UNIVERSITÀ DI PISA

Corso di Laurea Magistrale in Fisica

Anno Accademico 2013/2014

Tesi di Laurea Magistrale

Panchromatic Study of the Impulsive Phase of Solar Flares

Candidato

Antonio Alessandro Cilla

Relatore

Prof. Steven Neil Shore

Contents

Chapter 1

Introduction

The Sun would be an anonymous G-type main sequence star, if it wasn't at the center of the only planetary system we know capable of supporting intelligent life. This does nothing for the importance of the Sun for the rest of the Universe but it is the only star we can extensively study from such small distance. This means that we can resolve its surface, observe small spatial scale and short timescale processes: it is the only "laboratory" we can use to acquire informations about what happen in the atmosphere and on the surface of a star.

This thesis is in the spirit of the long standing research program "Living with a Star[1]" that links solar and heliospheric phenomena with the Earth and its immediate environment. From such a small distance (we are at about 300 solar radii - $R_\odot$) we have the opportunity of observe everything, from the surface to the lower atmosphere and the whole corona with instrumentation having a resolution of only a few hundred of kilometers. Nonetheless, when we use instruments that do not have such a spatial and\or temporal resolution we can see that other solar-like stars show similar phenomena to the large scale more stable structures.

The *Copernican hypothesis* asserts that nothing is particularly distinctive about the Sun or the solar system, so the presence of one scale will imply the other and we can use our Sun as a bridge between us and the rest of the population of stars in the Galaxy.

The purpose of this thesis is the study of magnetic structures and energetic solar phenomena, the flares, that must also occur on other stars. Using a limited but particularly energetic set of event coming from the same active sunspots group and that happened within few days, we will show that a series of similar characteristics emerge that point to generic behaviors of the phenomenon.

The study of sunspots began at the beginning of the 17th century and it's likely that sunspots were already been seen before the beginning of telescopic observations. The flare, instead, is a phenomenon that was more recently discovered. They were first observed by

---

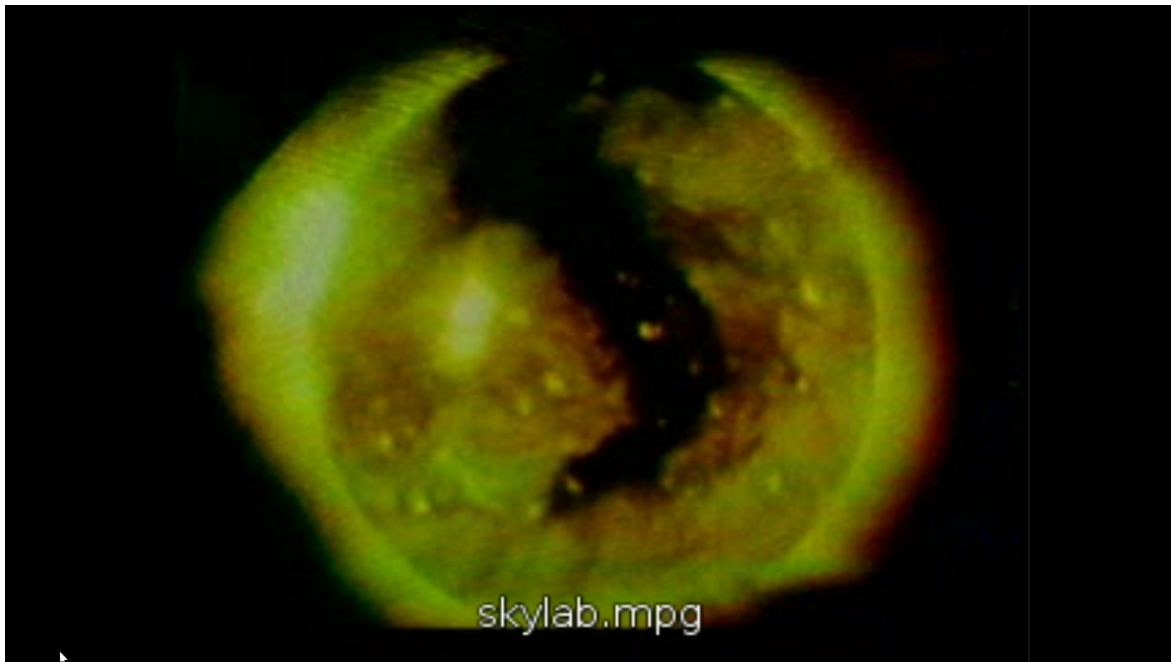[1]http://science.nasa.gov/about-us/smd-programs/living-with-a-star/

Figure 1.1: An image of the Sun in the X-ray in the 0.3 - 2 keV energy range, taken from the Skylab space station. One of the discovery images of a coronal hole.

Richard Carrington during 1859 as intense and short-lived optical brightenings in the vicinity of a sunspots group. He also guessed that they were associated with intense terrestrial magnetic activity (observed as magnetic storms) registered by ground based observatories all around the world. In a paper published in 1908 with the title *"On the Probable Existence of a Magnetic Field in Sun-Spots"*, George H. Hale the discovered of the presence of intense magnetic field in sunspots that followed the activity of the Sun along the so called "solar cycle". He measured the magnetic field along the line of sight using Zeeman splitting of metallic lines in the photospheric absorption spectrum, finding that the magnetic field was concentrated in the dark regions (the "darkness" was later explained as the local suppression of surface convection by these fields).

So it was not surprising that observations from rockets in the '60 and from the Skylab mission, a space station that orbited the Earth between 1973 and 1979, showed that the atmosphere of the Sun was bright in the X-ray (see Fig.1.1) and that the coronal structures were aligned with the active regions.

Decades of observation have shown the chaotic motion of the photospheric and envelope thermal convection (where the temperature is ~ 5800K) and its role in structuring the global magnetic field. The chromosphere, which is an emission line region higher in the atmosphere whose temperature is of the order of 10^4K showed the same structures which continue in the corona. The extremely high temperature of the corona ($\sim 10^6$K) and its striking inhomogeneity show further evidence of strong magnetic structuring and in situ energization.

What we now know about the solar atmosphere is that it adjust to the evolution of the large-scale and small-scale structure of the magnetic field which is created and modified by dynamic processes such as the differential rotation and the convective motion of the plasma . In general we can distinguish three main structures: *quiet corona*, *coronal holes* and *active regions*.

The *quiet corona* in the X-ray and EUV images show a quasi-homogeneous (sometimes amorphous) surface. Loops and arcades are present, but, in general, it doesn't show a well defined structure.

The *coronal holes* are zones where the X-ray emission is much lower. These regions are often called "open corona" because here the field lines are not closed on the surface but extend in the interplanetary medium, letting part of the plasma to escape. This is also explain their darkness: in an optically thin medium, the intensity of the emission is directly related to the density of the emitting material and its temperature, both of which are substantially reduced by the advective transport. Coronal holes are the originating site of the fast solar wind.

Active regions show much stronger emission much stronger than the other parts, and the emission spans the whole electromagnetic spectrum. They usually coincide with groups of sunspots, i.e. zones where there is a large concentration of magnetic flux created by sub-surface dynamical processes. These motions stress, twist, and concentrate the magnetic field lines in small structures, leading to the storage of magnetic energy. The signature of this concentration is the presence of very complex and braided loops that connect two spots within a bipolar magnetic region (BMR). Their length is of the order of 10^4 - 10^5 km and they are filled with hot emitting plasma having temperatures ranging from 10^6 to 10^7K. The energy stored in the stresses of the magnetic field during the solar cycle doesn't remain there for long: from time to time some processes find a way of relaxing the magnetic field lines. The most energetic and spectacular process is called a *Solar Flare*.

A *Solar Flare* is one of the most energetic phenomenon of the solar system, during which the magnetic energy stored in the stresses of the magnetic field is released and is converted in kinetic energy of particles and heat. They are classified according to NOAA GOES[2] scale (see Tab.1.1), which measures the X-ray flux in the wavelength range 1 - 8 Å that reaches the Earth.

Fig.1.3 shows a schematic of what occurs during the event. It starts with a couple of spots with opposite polarity, connected by field lines, around which charged particle are spiraling following the field lines. The buoyant emergence of flux from underneath the surface pushes the already emerged field lines higher in the atmosphere and an X-type neutral point is created, where two magnetic lines of opposite polarity meet. When this happens, a process called *Magnetic Reconnection* take place: the field lines disconnect from the actual, more energetic configuration and reconnect to a lower energetic configuration:

---

[2]http://www.swpc.noaa.gov/products/goes-x-ray-flux
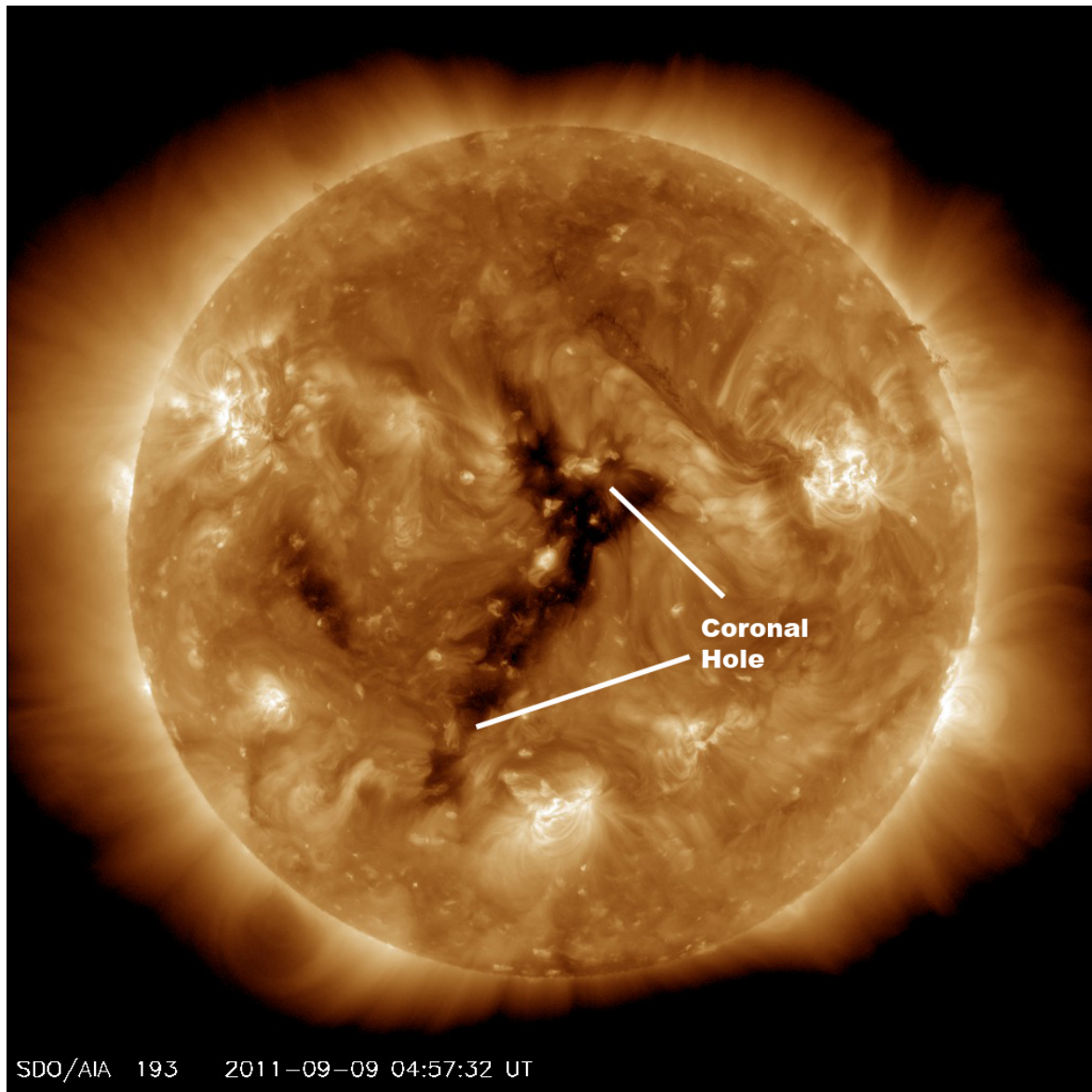
Figure 1.2: An image taken using the SDO satellite, showing the emitting corona and the presence of coronal holes. From http://sdo.gsfc.nasa.gov/

Class	Peak between 1 and 8 Å [W m^{-2}]
B	$I \leq 10^{-6}$
C	$10^{-6} \leq I < 10^{-5}$
M	$10^{-5} \leq I < 10^{-4}$
X	$I \geq 10^{-4}$

Table 1.1: Classification of a solar flare. The flux is measured by GOES satellites[2].

Figure 1.3: From http://www.astro.wisc.edu/ clinch/
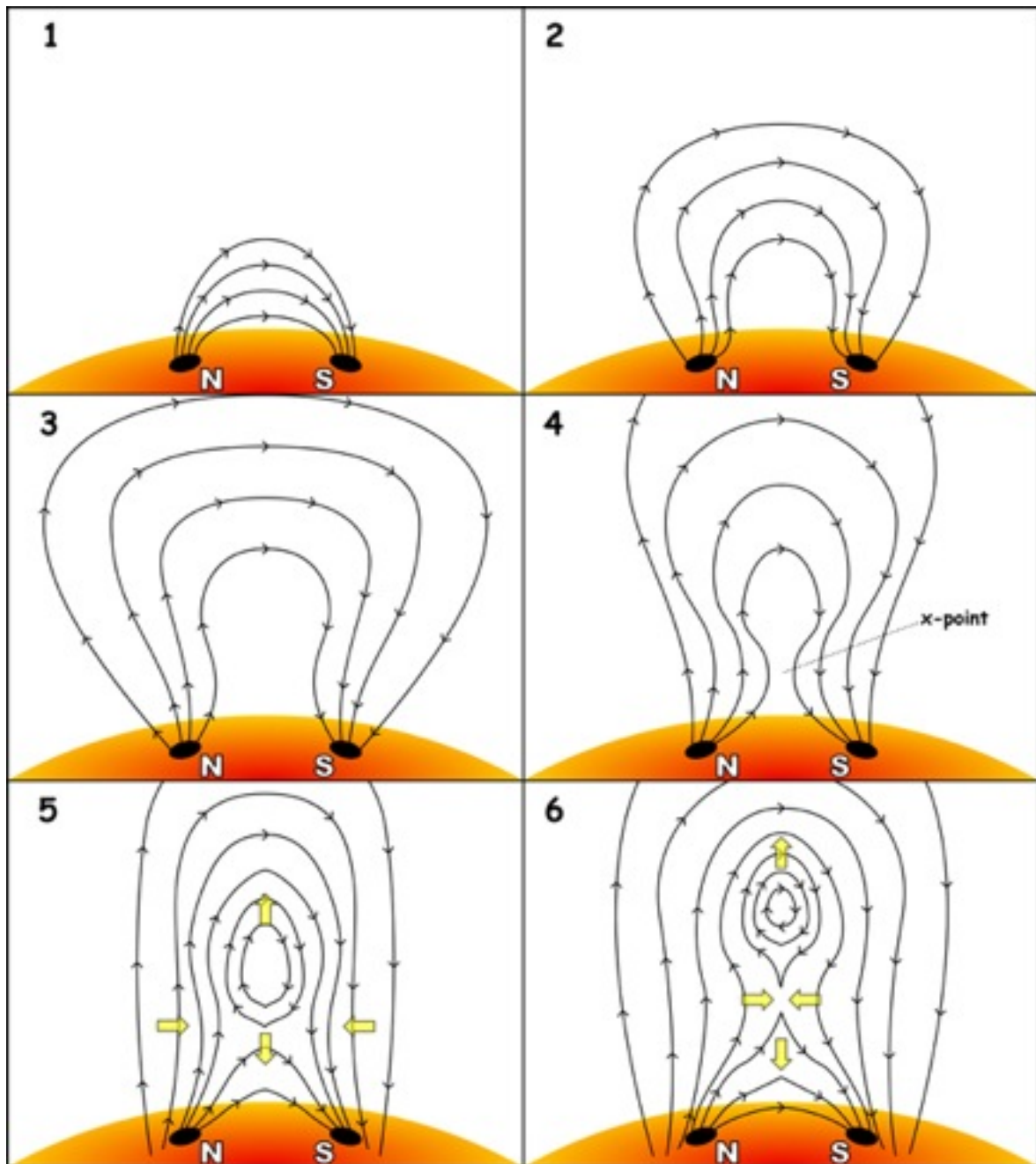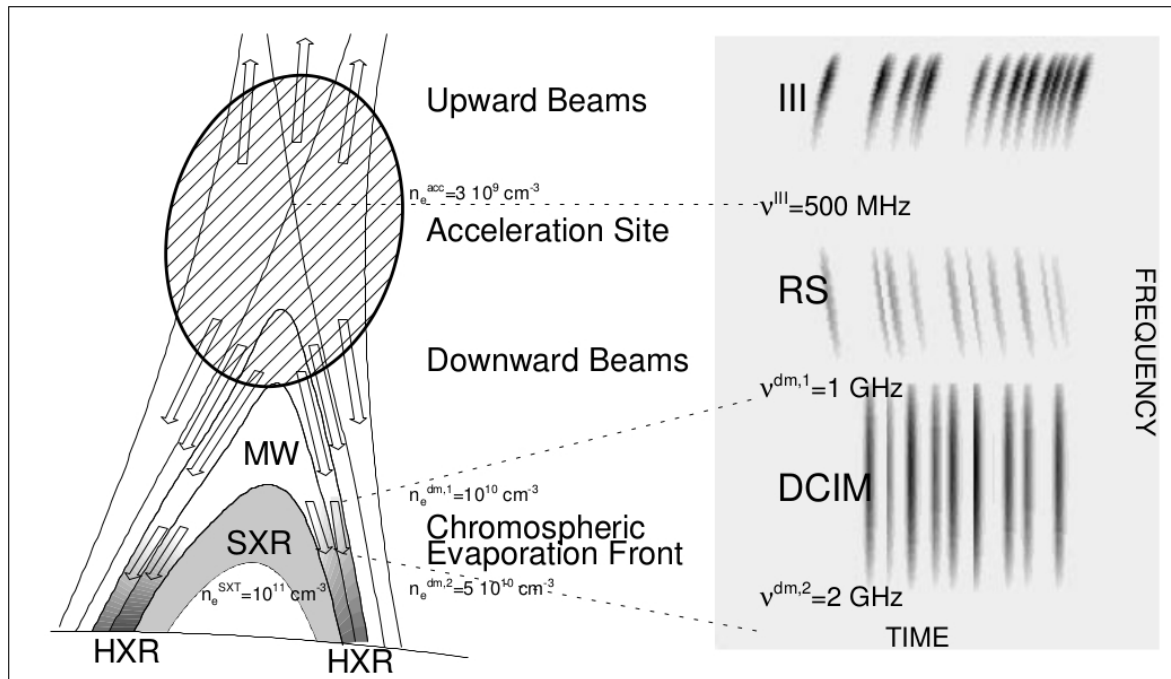
Figure 1.4: Schematic of what happen during a flare: the particles are accelerated and two streams depart from the acceleration region. The streaming particles will produce gyrosynchrotron emission because of the spiraling, and the interaction with the ambient plasma will produce thermal SXR and EUV radiation. The precipitating particles will hit the surface and produce HXR radiation due to bremsstrahlung. From Bastian et al. [1998]

the topology has changed and the particles can now flow from one field line to another. A considerable amount of energy is released, about 10^{32}erg which a significant fraction of the energy that the whole Sun emits every second ($4{\cdot}10^{33}$erg s^{-1}). As sketched in Fig.1.4 the released energy goes into heat and acceleration of particles, which stream along the field lines in opposite direction relative to the acceleration region and emit on the entire electromagnetic spectrum: radio waves from the gyrosynchrotron emission due to spiraling electrons; ultraviolet, extreme ultraviolet and soft X-ray (SXR) from the heated material; hard X-ray (HXR) and γ-ray from the bremsstrahlung process due to the electrons hitting the surface, depositing there all the kinetic energy gained during the reconnection process.

The details of the acceleration process are still hazy. The region within which the particles are accelerated has an estimated length scale of $\sim$10 km, but this is at least an order of magnitude smaller than the resolution capabilities of the modern instruments (for instance, the smallest resolved element for the *SDO* satellite (Fig.1.2) is $\sim$900 km).

It is still unknown how a large number of particles ($\sim$$10^{36}$ electrons) can be confined in such a small region and then so efficiently accelerated within *a fraction of a second*. Some models have been developed during the second half of the last century to explain the whole process, but many aspects of the flaring process have not yet been satisfactorily resolved. They are reviewed in the following sections.

1.1   Magnetic reconnection theory

The description of the magnetic reconnection theory in the MHD contest will follow Priest and Forbes [2000] and Retinò [2007]:

The equation used to describe the phenomenon of magnetic reconnection are:

$$\frac{\partial \rho}{\partial t} + \nabla \cdot (\rho \mathbf{u}) = 0 \qquad\qquad \text{conservation of mass} \qquad\qquad (1.1)$$

$$\frac{\partial \mathbf{u}}{\partial t} + (\mathbf{u} \cdot \nabla)\mathbf{u} = -\frac{\nabla p}{\rho} + \frac{\mathbf{J} \times \mathbf{B}}{\rho} \qquad \text{equation of motion} \qquad\qquad (1.2)$$

$$\frac{\partial \mathbf{B}}{\partial t} = \nabla \times (\mathbf{u} \times \mathbf{B}) + \frac{1}{\mu_0 \sigma}\nabla^2 \mathbf{B} \qquad \text{induction equation incl. resistivity} \qquad (1.3)$$

$$\mathbf{E} + \mathbf{u} \times \mathbf{B} = \frac{\nabla \times \mathbf{B}}{\mu_0 \sigma} = \frac{\mathbf{J}}{\sigma} \qquad\qquad \text{Ohm's law} \qquad\qquad (1.4)$$

where $\mathbf{E}$ is the electric field, $\mathbf{B}$ is the magnetic induction, ρ is the mass density of the plasma, $\mathbf{u}$ is the plasma velocity, σ the conductivity, $\mathbf{J}$ the electric current and p the thermal pressure.

If the timescale for the collisions is much more longer than the timescale for a fluid element to cross the system, we say that the conductivity σ is (more or less) infinite, then equations 1.4 and 1.3 become :

$$\mathbf{E} + \mathbf{u} \times \mathbf{B} = 0 \qquad\qquad\qquad (1.5)$$

$$\frac{\partial \mathbf{B}}{\partial t} = \nabla \times (\mathbf{u} \times \mathbf{B}) \qquad\qquad\qquad (1.6)$$

which express the approximation called "frozen in approximation" in an ideal plasma. Physically, this means that every particle inside a magnetic flux tube will remain within it unless the plasma is no longer ideal. Each motion of the plasma drags with it the embedded field lines, and each motion of the field lines drags with it the plasma.

If two field lines with opposite polarity are forced together in a space which is small compared to the overall length scale of the system, we have a sheared magnetic field so $\nabla \times \mathbf{B}$ is no longer negligible. It generates a current, the "frozen in approximation" no longer holds and the diffusion term in eq.1.3 now enters. The opposite directed field lines can now disconnect and reconnect in a new, lower energy configuration that leads to the expulsion of magnetized plasma towards the interplanetary medium and to the acceleration of particles towards the surface of the Sun.

Two broad scenarios have been developed to describe this process. Here I will briefly outline them to have a context for the analysis later in this thesis.

1.1.1 Sweet-Parker model

Fig.1.5 shows a schematic of the Sweet-Parker reconnection model (Sweet [1958]; Parker [1957]). The field lines lie in the XZ plane, the shaded region in the middle, called the *diffusion region*, having a length 2L along $\hat{z}$ and 2a along $\hat{x}$. At the center of the diffusion region the magnetic field is zero, which is the point where the magnetic field flips from positive to negative.

In the inflow region, which is outside the diffusion region, the current is zero and the electric field is given by:

$$E = u_0 B_0 \tag{1.7}$$

corresponding to the inflow of plasma from the sides of the current sheet with a velocity of u_0. The electric field at the center of the diffusion region (where the magnetic field vanishes) is:

$$E = \frac{J}{\sigma} \tag{1.8}$$

and the current is:

$$J = \frac{B_0}{\mu_0 a} \tag{1.9}$$

If we are in a steady-state, the electric field is constant and:

$$u_0 = \frac{1}{\mu_0 \sigma a} \tag{1.10}$$

The continuity equation 1.1 integrates as:

$$L u_0 = a u_e \tag{1.11}$$

with u_e being the outlow speed along the $\hat{z}$ direction. We can now eliminate the width a (eq.1.10 and eq.1.11) so:

$$u_0^2 = \frac{u_e}{\mu_0 \sigma L} \tag{1.12}$$

For any L, the eq.1.12 links u_e and u_0, and using eq.1.11 we find the width of the region to be

$$a = L\frac{u_0}{u_e} \tag{1.13}$$

From magnetic flux conservation, we can compute the outflow magnetic field strength:
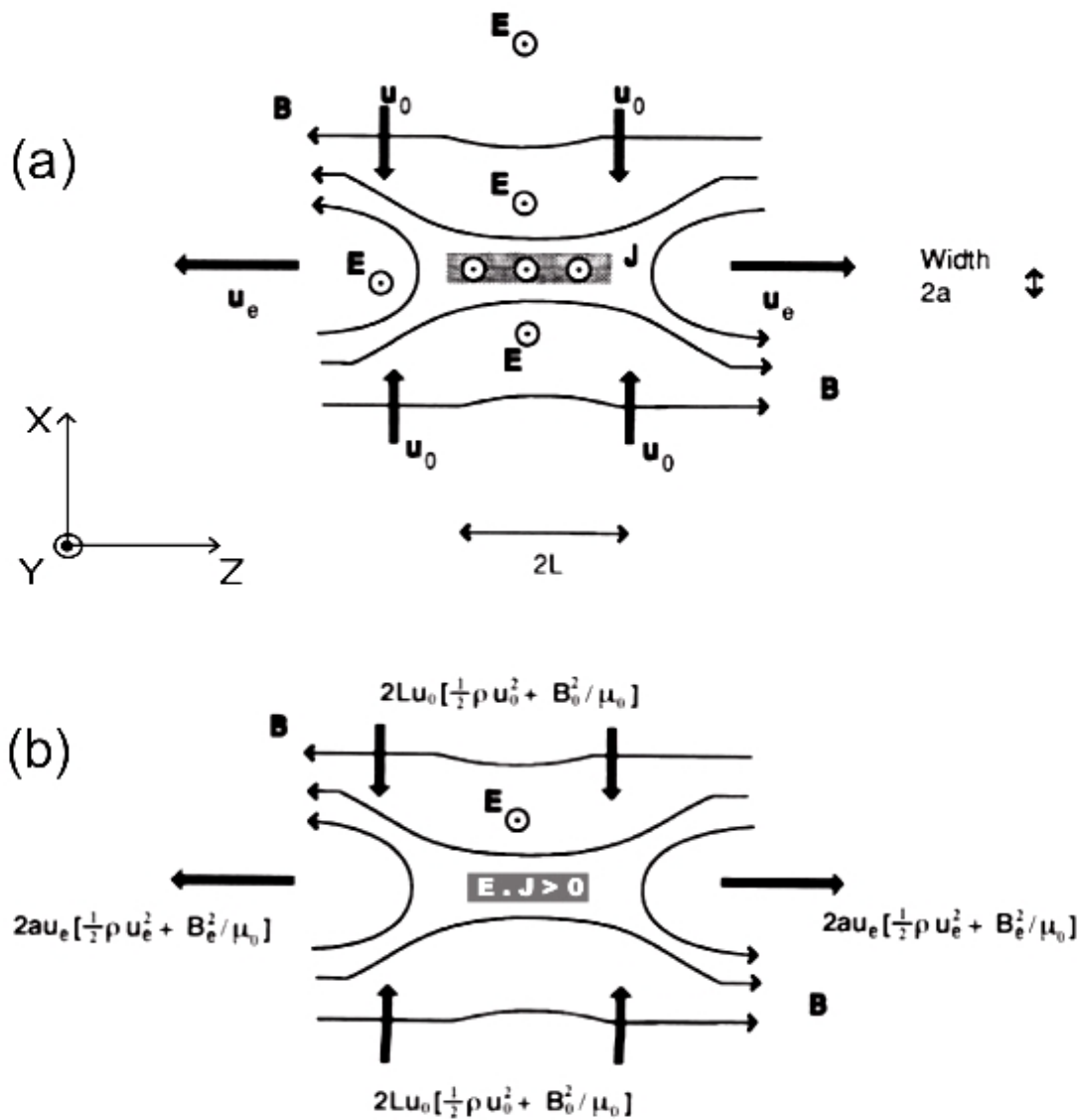
$$B_e = B_0 \frac{u_0}{u_e} \tag{1.14}$$

Figure 1.5: Schematic description of the Sweet-Parker model. Top panel: particle flux conservation. Bottom panel: energy flux conservation. From Retinò [2007]

We can compute the outflow speed using eq.1.2 neglecting the thermal pressure (because we assume an environment with a $\beta = \frac{p_{therm}}{p_{mag}} \ll 1$, where $p_{mag} = B^2/2\mu_0$) and imposing the steady-state. The Lorentz force accelerates the plasma from rest to u_e over the distance L and if we impose the balance between the Lorentz force and the inertial term we obtain:

$$\rho(\mathbf{u} \cdot \nabla)u_z \approx (\mathbf{J} \times \mathbf{B})_z \quad \longrightarrow \quad \rho\frac{u_e^2}{L} \approx \frac{B_0 B_e}{\mu_0 a} \tag{1.15}$$

Combining eq.1.15 with eq.1.11 and eq.1.14 we get:

$$u_e = \frac{B_0}{\sqrt{\mu_0\rho}} = u_{A0} \tag{1.16}$$

where u_{A0} is the *Alfvén speed*. We can also compute the value of u_0 from the formula:

$$u_0 = \frac{u_{A0}}{\sqrt{R_{m0}}} \tag{1.17}$$

where $R_{m0} = Lu_{A0}\sigma\mu_0$ is the magnetic Reynolds number. Since $R_{m0} \gg 1$, then u_0 is much smaller than u_a, $B_e \ll B_0$ and $a \ll L$. Thus, after the reconnection process, part of the magnetic energy is released and the system relaxes in a less energetic state.

The energetic balance of the region: the electromagnetic energy that enters the system can be described by the flux of the Poynting vector:

$$\Phi(\mathbf{S}) = \frac{EB_0}{\mu_0}L = \frac{B_0^2}{\mu_0}(u_0 L) \tag{1.18}$$

so the ratio of kinetic energy to electromagnetic energy entering the system is:

$$\frac{(1/2)\rho u_0^2}{B_0^2/\mu_0} = \frac{u_0^2}{2u_{A0}^2} \ll 1 \tag{1.19}$$

which means that most of the energy that enters the system is electromagnetic. Then since $a \ll L$ and $B_e \ll B_0$ the outflowing electromagnetic energy is $E\frac{B_e}{\mu_0}a$, which is much smaller than the inflow rate of electromagnetic energy. So, magnetic energy must be dissipated during the reconnection process. The ratio between the inflowing electromagnetic energy (EM_0) and the outflowing kinetic energy (K_e) is:

$$\frac{K_e}{EM_0} = \frac{(1/2)\rho u_e^2(u_e a)}{B_0^2/\mu_0(u_0 L)} = \frac{(1/2)u_e^2}{u_{A0}^2} = \frac{1}{2} \tag{1.20}$$

So half of the inflowing electromagnetic energy goes into kinetic energy of particles, and the other half heats the medium.

1.1.2 Petscheck model

In the Sweet-Parker model, the reconnection region is coincident with the diffusion region through which all of the plasma must pass to be accelerated. The reconnection rate is

Figure 1.6:

therefore quite slow and this does not succeed in explaining well the observations. Using eq.1.17 we can write:

$$M_0 = \frac{u_0}{u_{A0}} = \frac{1}{\sqrt{R_{m0}}} \tag{1.21}$$

where M_0 is called *inflow Alfvén Mach number* or *dimensionless reconnection rate* and since R_{m0} for the plasma is $R_{m0} \gg 10^6$, M_0 is very small.

Petscheck proposed a model (Petschek [1964]; see Fig.1.6) in which the Sweet-Parker diffusion region is replaced by a much smaller diffusion region with two standing shocks in the outflowing direction. In this configuration, the most part of the plasma *is not accelerated in the reconnection region*, but it is accelerated by the two slow shocks exiting from the diffusion region. This scenario yields an higher reconnection rate and is in much closer agreement with the observation than the Sweet-Parker model. The Petschek model predicts the scaling:

$$M_0 = \frac{\pi}{8 \ln R_m} \tag{1.22}$$

which yields a reconnection rate that is much larger than the Sweet-Parker rate, $M_0 \approx 10^{-1}$ to 10^{-2}.

However, these models seems to oversimplify the problem. For instance, the real event is not a 2D one and other mechanisms may play a substantial role in releasing the magnetic energy and in the acceleration of particles.

Figure 1.7: A schematic view of the possible mechanisms responsible for particle acceleration. From Birn and Priest [2007]

1.1.3   Acceleration of particles

As explained by Neukirch, Giuliani & Wood in Birn and Priest [2007], it is widely accepted that the the energy gained by the particles during the reconnection process comes from the energy stored in the magnetic field, which then relaxes and the energy is transferred to the particles and the surrounding medium. It is still however a matter of intense debate as to what happens on the small-scale, and more precisely, what is the process that produces so many and such energetic particles in so short a time.

Fig.1.7 shows a schematic review of the possible mechanisms that are thought to be responsible for the particle acceleration. In the following subsecton the main acceleration process will be outlined, following the explanation from Birn and Priest [2007] and Aschwanden [2002].

1.1.3.1   Electric fields acceleration

Reconnection is associated with the creation of strong electric fields which can easily accelerate particles. Orthogonal electric fields can form in a 2D model (along the X-line) or along separators in 3D reconnection model. In fact, in a 3D model, parallel electric fields

are needed to let the disconnection and the reconnection happen (*DC acceleration models*), as shown in Neukirch [1997].

The *DC acceleration models* can be divided in sub-Dreicer and super-Dreicer models, whether the accelerating field is weaker or stronger than the Dreicer field defined as:

$$E_D \approx 6 \cdot 10^{-3} \left[\frac{n}{10^{15} m^{-3}} \right] \left[\frac{T}{10^6 K} \right] V \, m^{-1}. \tag{1.23}$$

were n is the number density and T the temperature.

In **sub-Dreicer** model the particles are accelerated untill they reach an equilibrium between the acceleration due to the electric field and the deceleration due to coulomb collision. This kind of electric field is quite weak and it needs long distances to accelerate particles (namely $\sim 10^4$ km) and even though the length required is compatible with the usual length of a loop, it is not clear how such long scale electric fields can be generated.

In **super-Dreicer models** (see Aschwanden [2002]) the particles can be accelerated indefinitely. in the presence of typical value for the magnetic and electric field of $B_{||} = 100G$ and $E_{||} = 10^3 V \, m^{-1}$, the electron energy that can be reached is of the order of $W \approx 100 keV$. The estimated scale length over which the acceleration takes place is of the order of $l \approx 10 km$ (instead of $10^4 km$ as in sub-Dreicer models) which is a length scale compatible with the structure of the reconnection point of a single loop or a loop arcade, also if we hypothesize a scenario in which the acceleration region is fragmented. Moreover, observational and theoretical estimates of the strength of the field give us values of the order of 10^2-$10^3 V/m$ which are compatible with the super-Dreicer model.

1.1.3.2   Shock acceleration

Shock-Drift Acceleration: we know that in a shock the normal component of the magnetic field across the shock front remain constant, while the tangential component increases. This means that the magnitude of the total magnetic field increases across the shock front. Since the magnetic moment for the particle has to remain constant ($\mu = mv_{\perp}^2 / 2B$), then if the total magnetic field increases so does the perpendicular velocity of the particles, resulting in a net gain of energy for the particles.

However the energy gain is comparable with the ratio between the downstream magnetic field and that upstream, which is never greater than 4, and requires that the "frozen in" approximation holds.

First-order *Fermi* Acceleration at Fast Shock and Mirror Trapping: Tsuneta and Naito [1998] discussed the possibility that a fast shock should be coincident with the X-ray source near the looptop, formed because the accelerated particles move towards a region with higher density and lower Alfvén speed. If there is a point when the speed of the particle exceeds the magnetoacoustic wave velocity a fast shock appears ahead of the denser region.

Figure 1.8: A model for the mechanism that traps particles in the region between the acceleration region (outside the top of the figure) and the fast shock at the looptop .From Somov and Kosugi [1997]

In this case, some requirements have to be fulfilled in order to let the model be explicative of the observations:

- the time required for the acceleration has to be of the order of 1 sec;

- the number of excited electrons has to be of the order of 10^{34} - 10^{35};

- the acceleration rate has to be higher than the collisional loss rate:

$$\frac{dE}{dt} = \left(\frac{dE}{dt}\right)_{acc} - \left(\frac{dE}{dt}\right)_{coll} > 0; \qquad (1.24)$$

- the particles have to gain a sufficient amount of energy which is needed to explain the 50 keV X-ray emission found by Masuda et al. [1995], located near the looptop;

From eq.1.24, the energy of the electrons must be greater than 4 keV. Thus, a mechanism that accelerate particles from the thermal distribution to 4 keV is needed, and this role may be played by the slow shock, as explained by Tsuneta and Naito [1998].

In addition, Somov and Kosugi [1997] proposed a trapping mechanism in the region between the reconnection region and the fast shock, as shown in Fig.1.8. They propose that each field line reconnection that happen in the reconnection region is accompanied by the relaxation of the magnetic field into a lower energy state than the one we had

before the reconnection. The particles (that now are spiraling around the field lines that are relaxing) will mirror either near the footpoints, or near the intersection between the fast shock and the magnetic lines. This means that the magnetic trap collapses while the field line are relaxing and the particles gain energy through betatron effect and first-order *Fermi* acceleration.

So, to summarize what happen in this scenario, the particles gain energy through these effects:

- the magnetic moment of the particles (i.e. $\mu = mv_\perp^2/2B$) should remain constant, but the particles, after the reconnection process, are trapped in a lower part of the corona, where the magnetic field is stronger. So, if B grows, also $v_\perp^2$ has to grow in order to keep μ constant;

- the trapped particles move back and forth in the magnetic trap which is delimited by the fast-mode looptop-shock or by the footpoints. Since the trap is shrinking, it means that the distance between the two mirror point is reducing, increasing the parallel momentum (i.e. first-order *Fermi* acceleration) and eventually leading to the precipitation of the particles when the parallel momentum is high enough to let the particle enter the "loss-cone".

1.1.3.3 Stochastic acceleration and second-order *Fermi* acceleration

Another process that can accelerate particles is the so called Stochastic acceleration. It is a process during which, even though may gain and lose the same amount of energy in the short term, in the long term the net amount of energy received by the particle is positive. One of the most important accelerating agents are MHD waves, reviewed by Miller et al. [1997].

The wave-particle interaction through resonance is very important for the stochastic acceleration process. As Miller et al. [1997] explains, we have a resonant process when the following equation is satisfied:

$$x \equiv \omega - k_\parallel v_\parallel - l\Omega/\gamma = 0 \tag{1.25}$$

where x is the mismatch parameter, $v_\parallel$ is the parallel particle speed, γ the Lorentz factor and Ω is the cyclotron frequency of the particle.

If l is an integer greater than zero, the frequency of the electric field of the wave is a multiple of the gyration frequency of the particle in the guiding center frame (and the particle and the wave rotate in the same sense). In this scenario, the particle feels a static electric field for a certain interval of time, so it can be accelerated or decelerated and this depends on the relative phase between the gyration of the particle and the rotation of the wave. A special case arises when $l = 0$ when the resonance is between the particle speed and wave phase velocity (Landau resonance).
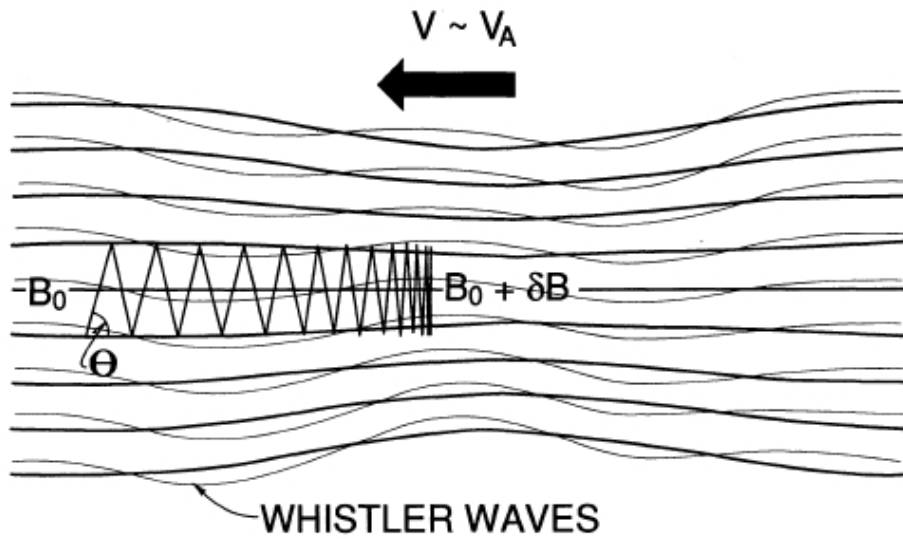
Figure 1.9: This image from Larosa et al. [1994] shows how a perturbation in the magnetic field can become a magnetic mirror.

In the presence of a single wave, the velocity of the resonating particle oscillates around the resonance velocity without any net gain in energy. The frequency of this oscillation is called bounce frequency, ω_b. This frequency is important because we can have a resonance when $|x| \leq 2\omega_b$ (the strict condition $x = 0$ is not needed).

But, if we have a broad spectrum of waves, the particle can first resonate, for example, with the one which has the lowest frequency. When the amplitude of oscillation around the resonance speed is high enough, the particle can gain a sufficient amount of speed that it start resonating with the wave having an higher phase speed: the particle has been accelerated. This process can continue till when the particle reaches the upper limit of the spectrum of waves after which it cannot be accelerated anymore.

Miller et al. [1997] explain that if the amplitude of the waves is sufficiently high the process that accelerates the particles is no longer resonant but the *Fermi* acceleration mechanism acts, during which the particles are scattered from the waves as they bounce on the magnetic field perturbations.

Larosa and Moore [1993] and Larosa et al. [1994] show that MHD turbulence can be created during the reconnection process. After the reconnection of loops a shear flow instability in the jets of particle escaping the reconnection region can create fast mode waves at scales of the order of $\approx 10^8$ cm. These waves turbulently cascade untill they reach a length scale capable of either resonating with electrons (small amplitude) or scattering particles when they "bounce" on the turbulent magnetic field perturbations (large amplitude) and the particles are accelerated through second-order *Fermi* acceleration. An example of the latter mechanism is shown in Fig.1.9. They showed that a number of loops of the order of 10^2 may reconnect, which is compatible with a "bumpy" structure of the lightcurve, and that this mechanism can accelerate electrons from the thermal distribution up to energies

of the order of 25 keV.

Chapter 2

Flares analysis

Three X-class events were chosen for the analysis in this thesis. These occurred during three different days, from May 13th to May 15th 2013. The active region responsible of the events was "rising" from the western limb the first day, so the May 13 flare is on the limb, similarly to the well-known "Masuda flare", described in Masuda et al. [1995].

The instruments used for the analysis are the Nobeyama Radio Polarimeter (*NoRP*) for the radio emission, the Atmospheric Imaging Assembly (*AIA*) on board of the Solar Dynamics Observatory (*SDO*) for the Ultraviolet (UV) and the extreme ultraviolet (EUV), the Gamma-ray Burst Monitor (*GBM*) on board of the *Fermi* satellite and the *RHESSI* satellite for X-ray emission. A review of the instruments used is in Chapter 4.

In contrast to an experiment performed on Earth, the observation of astronomical events is a little more problematic. That's because we can just observe what's going on, we cannot switch on and off the object of interest, as you could do, for instance, with the LHC. Worse still, when observatories in low Earth orbit are used, it may happen that the satellite is in a position that makes the observation of the Sun impossible, because the Earth is occulting the solar disk. Every low Earth orbit has a period of ∼90 minutes and the Sun is hidden for 1/3 of each orbit. This is not a problem for *SDO* because it is in a geosynchronous orbit, but it is a problem both for *Fermi* and RHESSI. That's why two X-ray observatories have been used for this study.

The following analysis deals with the temporal behavior (or lightcurves) of the emitting regions in different portions of the electromagnetic spectrum, using also lightcurves in UV and EUV computed integrating the spatial resolved observation of *SDO* at different times. When possible, single structures[1] have been analyzed with the aim of checking whether the structures could be produced by the same population of particles emitting in different

---

[1]I say there is a structure if there is a finite interval (in the range between 2 sec and 100 sec) over which the minimum of the emission inside the interval is above the maximum of the emission computed over an interval which precedes the structure having a duration similar to the duration of the structure. Following this definition, the everage of the emission during the structure is usually three σ higher than the average emission before the structure.

ways at different wavelengths.

For the flare of 15/05, where it is possible to analyze the surface, a procedure has been developed to decompose the lightcurve of the whole region in eight different lightcurves computed integrating over a small portion of the surface, usually in coincidence with the regions were the loops "entered" the surface. The aim of this kind of analysis was to check whether different structures were produced by different population of particles in different part of the emitting region.

2.1 Flare 15/05/2013 Analysis

The detailed temporal development of the flare was divided into three principal intervals, shown in Fig.2.1 using the 2 GHz *NoRP* channel as the reference: the first peak, corresponding to the antecedent peak (mainly visible at low frequency), the middle part that covers the first stage of the main emission peak, and the main interval, where the bulk of the emission occurs. While these may appear arbitrary distinctions, as will be shown in this chapter there are specific behaviors associated with each sub-interval that render these choices natural. Almost every feature is present in each part of the spectrum that has been analyzed, which is an indication that they may be produced by the same ensemble of particles at each energy.
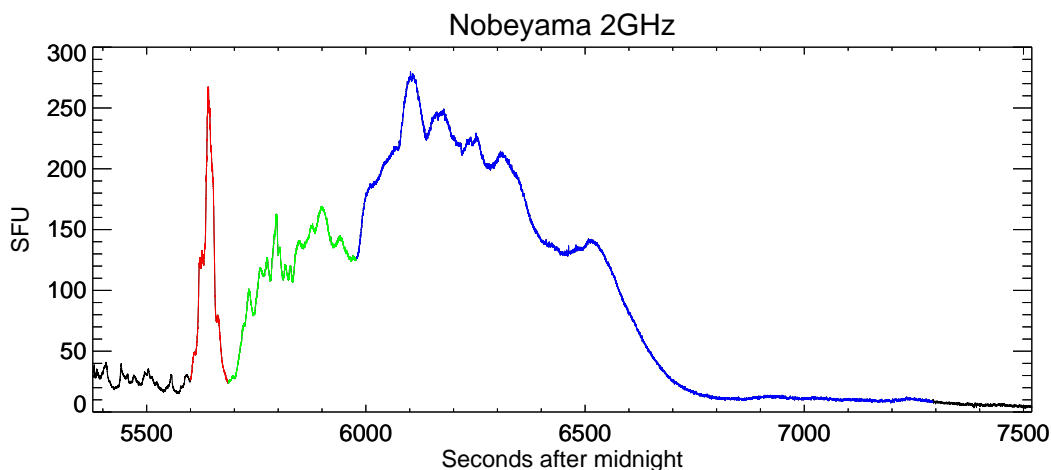
Figure 2.1: Energy flux at 2 GHz taken from Nobeyama Radio Polarimeter. The first peak is in red, in green there's the middle part and in red there's the bulk of the emission. Some sub-peaks are clearly seen. The Solar Flux Unit (SFU) is defined as $10^{-22} \cdot W \cdot m^{-2} \cdot Hz^{-1}$ or, equivalently, 10^4Jy.

The middle and the main part show a series of sub-peaks to be analyzed, with the limitation that they are not present in every energy channel. For increasing energy, the signal to noise ratio decreases so we will have some problems in detecting the peaks at high energy. As an example, the last three bands of the *GBM* are almost completely dominated by noise.

2.1.1 *NoRP* **Data**

Fig. 2.1 shows the 2 GHz channel, where the three parts are highlighted with colors: the
first peak is marked in red, the middle part in green and the main part in blue. In Fig. 2.3
all the frequency bands available in Nobeyama data are presented in solar flux units (SFU).
The maximum flux occurs in the 9.4 GHz band. Strong emission is present at the beginning
of the observation at 1 GHz but this feature was not included in the analysis because it had
very weak correlation with the other Nobeyama channels and X-ray emission and may
have been caused by interference. The signal to noise ratio (SNR) is highest at low energy
and minimum at high energy thus, most of the substructures in the 35 GHz and 80 GHz
channels, if present, may be hidden by the noise and these channels were also excluded in
the morphological analysis. They were used only in the main peak timing analysis.

Figure 2.4 displays a zoom of the first part of the emission. The first peak of the
emission is relatively strong at 1 GHz and 2 GHz, weak but present at 3.75 GHz and 9.4
GHz, and undetectable at 17 GHz. The maximum of the emission is almost coincident for
every channel at 5641.6 sec ±0.5 except for the 2 GHz where the peak is 1 sec earlier. Note
the two small peaks in the rising part of the signal in both 1 GHz and 2 GHz: they are
separated by 5.7 sec and the same feature has a delay of 7.1 sec at 2 GHz (same delay for
both peaks), so they may be causally related. A series of peaks with a $\sim$10 sec delay is
present in the 1 GHz channel.

Figure 2.5 shows the middle part of the emission. The first half, marked with the letter
E, is characterized by small peaks having a timescale (rise time plus decay time) of about
20 sec, comparable to the mean time elapsed between a peak and the previous one. These
peaks are present in every band except 17 GHz, but at this frequency they may be hidden
in the noise.

The second half, marked with the letter **F** (and by the sudden jump in 17 and 9.4 GHz
that is a real feature since it is present also in X-ray lightcurves and it is likely a single
acceleration event), shows a different behavior: the peaks are broader, having a time scale
ranging from 26 to 41 sec. The shortest timescale in this interval is due to the peak at 5876.7
sec, which is present only in the 2 GHz channel, while the 1 GHz channel shows just the
peak at $\sim$5900 sec.

The last two peaks are present in every band, so we can check whether there is an
energy dependent delay (see Fig.2.6). In Table2.1 there is the peak time for the last two
peaks at each frequency and is evident that there is an energy dependent delay. With the
exception of the 1 GHz band (in which the first peak seems to be a sum of small peaks and
the second peak is barely distinguishable), *the peak at 17 GHz leads those at lower energies and
each frequency leads the previuous one*.

Figure 2.7 shows the main part, where most of the total energy derived by the cooling
of the electrons is released. The letters mark different parts of the emission: the first peak
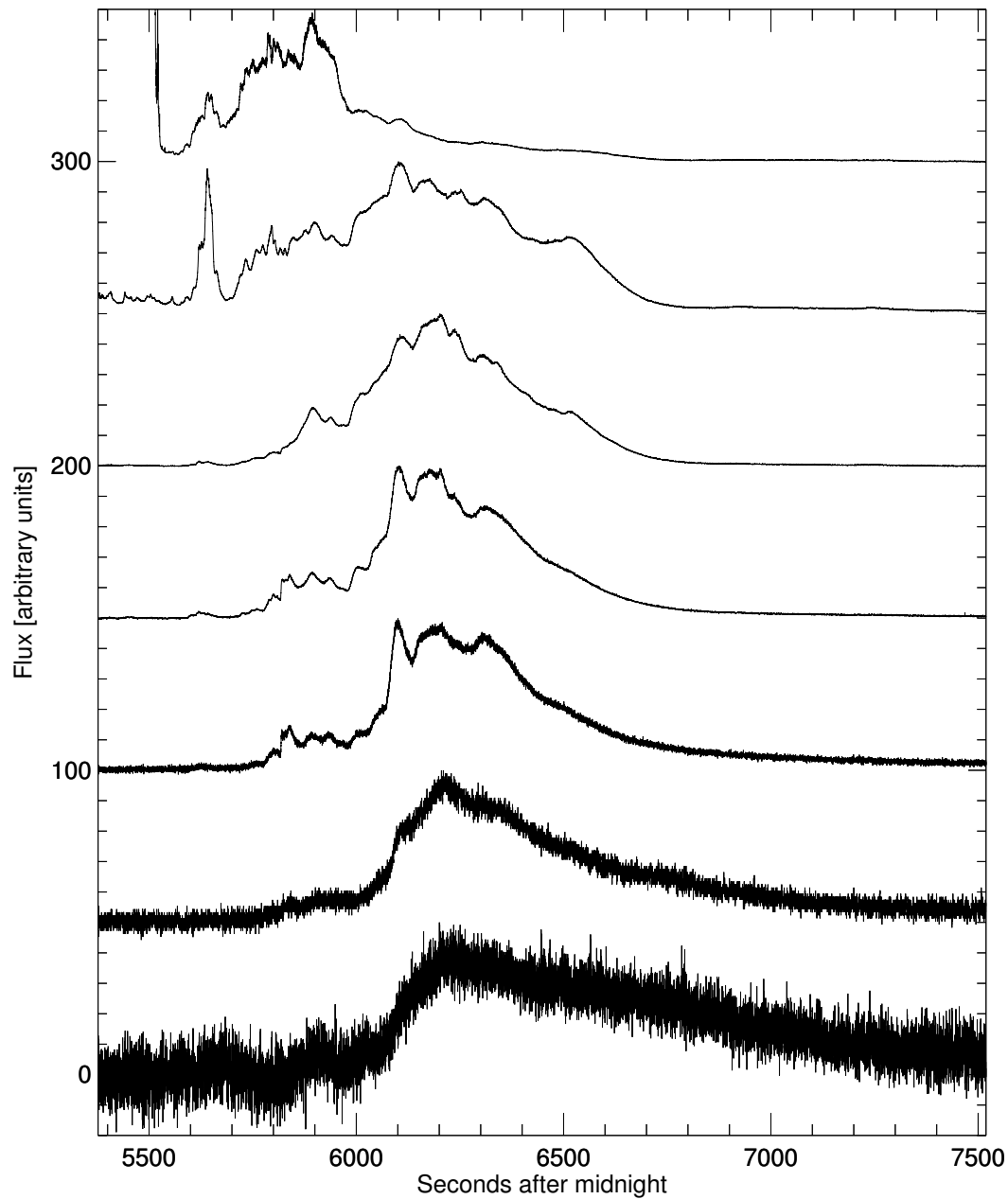
Figure 2.2: The whole dataset for the *NoRP* observation. Each lightcurve represent the emission at a different frequency. From top to bottom the frequencies are: 1 GHz, 2 GHz, 3.75 GHz, 9.4 GHz, 17 GHz, 35 GHz, 80 GHz.
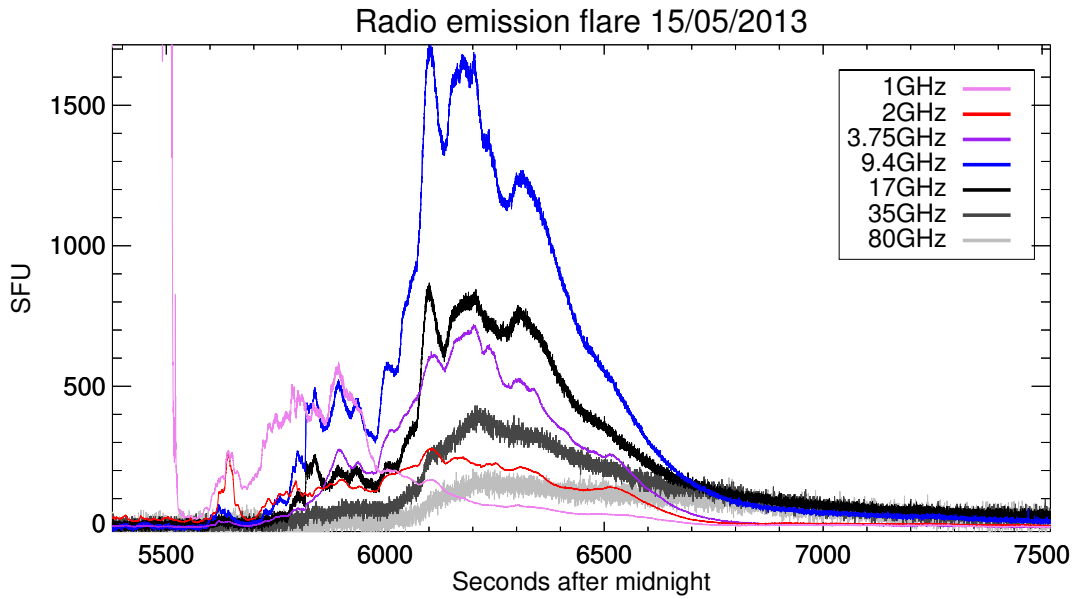
Figure 2.3: Flux in SFU for all the Nobeyama frequencies. The SFU (Solad Flux Unit) is defined as $10^{-22} \cdot W \cdot m^{-2} \cdot Hz^{-1}$ or, equivalently, 10^4Jy.
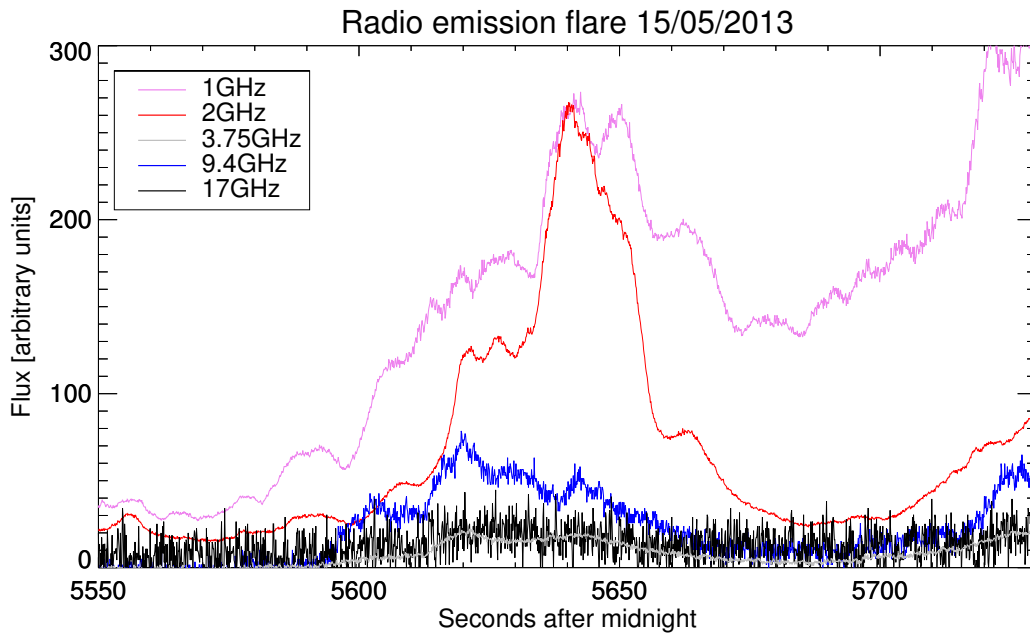
Figure 2.4: Comparison between the first five frequencies of Nobeyama, showing the emission in the time window of the first peak.

Freq (GHz)	1.0	2.0	3.75	9.4	17
Peak time 1 (s)	5893.1 $\pm$0.5	5895.6	5894.6	5893.0	5892.6
Peak time 2 (s)	-	5941.2	5937.2	5935.5	5934.3

Table 2.1: Energy dependent peak time of the last two peaks in Fig.2.5
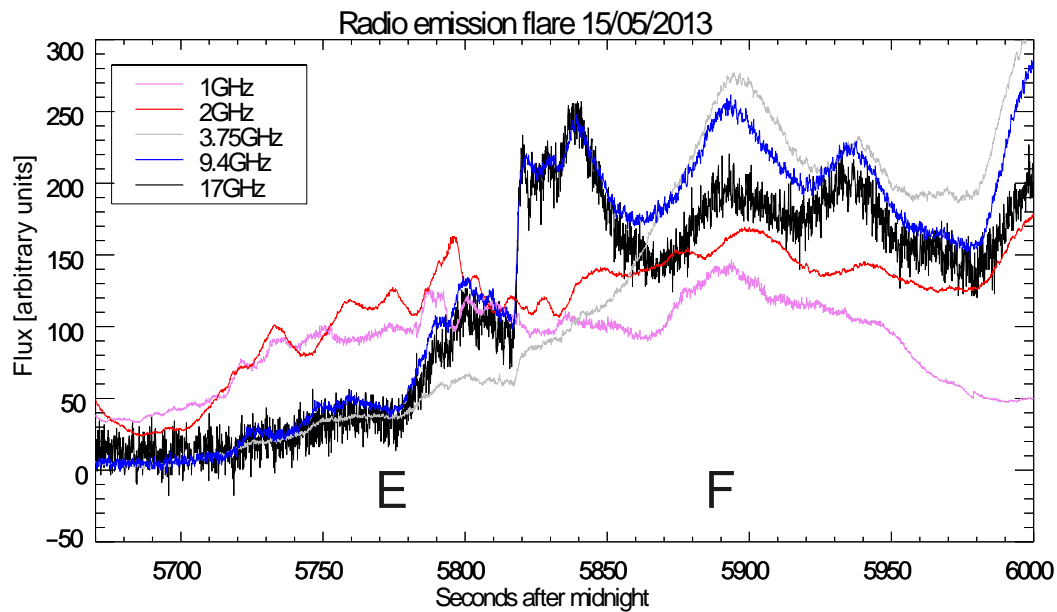
Figure 2.5: Comparison between the first five frequencies of Nobeyama, showing the emission during the pre-flare stage. The letters **E** and **F** mark the first half and the second half of this time window, where the emission shows different behavior (see the text for the description).
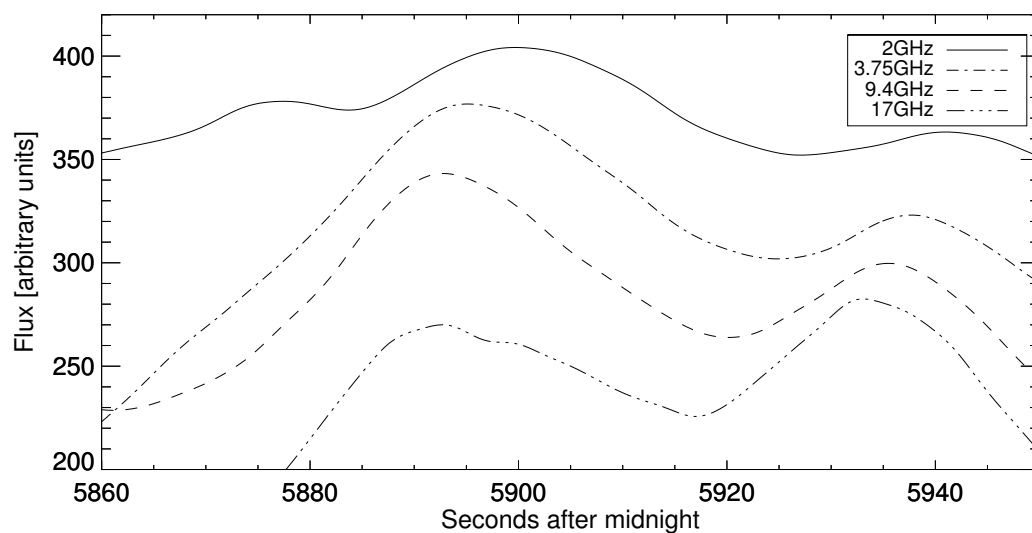
Figure 2.6: A zoom on the last two peaks of the middle part of the emission. The curves have been smoothed with a N(0,20) gaussian (i.e. the $\pm\sigma$ interval covers four seconds) to show the trend of the emission.
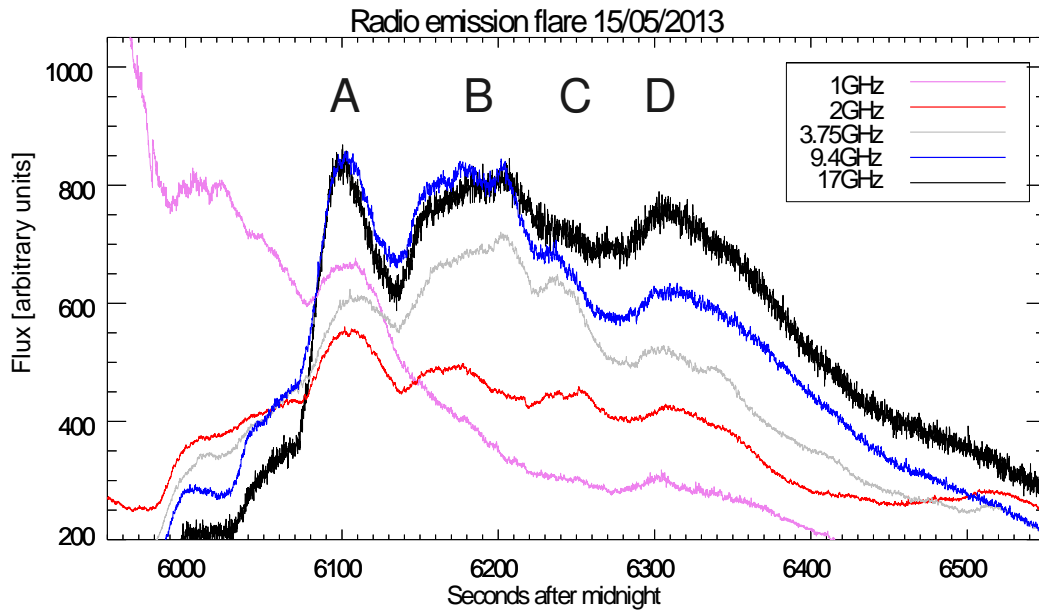
Figure 2.7: Comparison between the first five frequencies of Nobeyama in the main part, where there is the bulk of the emission is. The letters **A**, **B**, **C** and **D** mark four different parts of the emission. (see the text for the description)
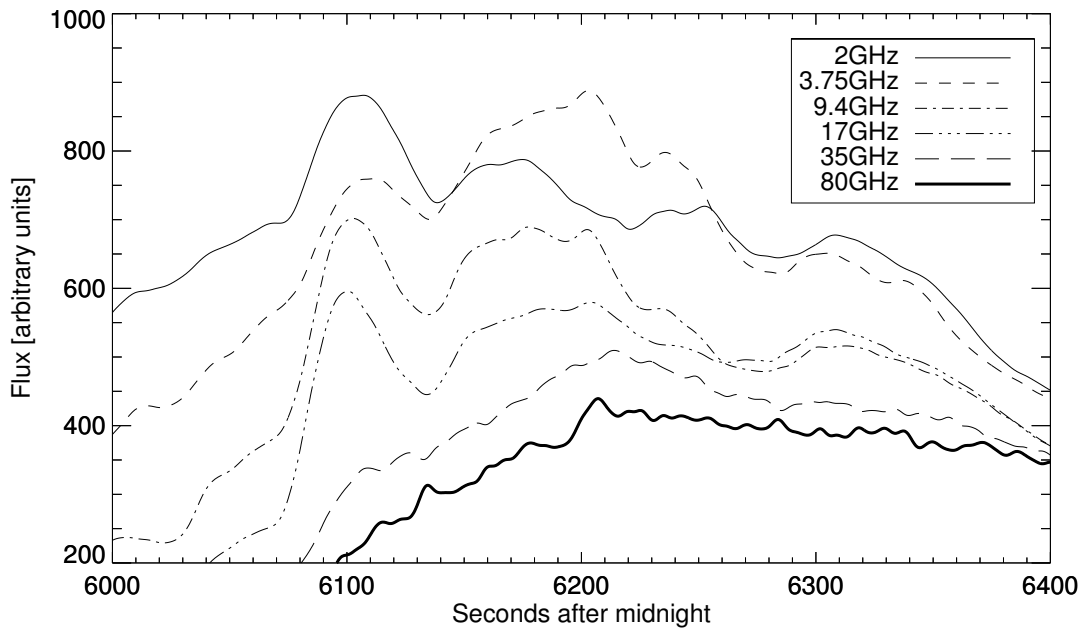
Figure 2.8: A zoom on the main part of the emission. The curves have been smoothed with a N(0,30) gaussian (i.e. the $\pm\sigma$ interval covers six seconds) to show the trend of the emission.

Peak	Freq (GHz)	σ=10pts	σ=20pts	σ=30pts
A	2.0	6107.5 ± 0.2	6107.5 ± 0.5	6106 ± 1
	3.75	6105.4	6112.4	6110
	9.4	6102.6	6102.6	6102
	17.0	6101.7	6100.8	6100
B	2.0	-	-	-
	3.75	6202.8	6203.1	6203
	9.4	6202.7	6202.5	6202
	17.0	6205.7	6204.5	6204
D	2.0	6307.4	6307.8	6308
	3.75	6305.4	6305.0	6304
	9.4	6314.3	6313.2	6312
	17	6308.8	6308.6	6308

Table 2.2: Energy dependent peak time of the three main peaks in Fig.2.7.

(part **A**) is the maximum of the emission. At a first glance, three or four main peaks seem to be present, but if we look at the detail of the emission we can clearly see that each peak is composed of different subpeaks. Moreover there is a peak in the last part of **B** that is absent at 1 GHz nor at 2 GHz. In Fig. 2.8 all the frequencies are shown. The lightcurves have been smoothed over a time window of 6 sec. It is still it is possible to see that substructures are present in every frequency, even though, at high energy (35 GHz and 80 GHz), they may just be an artifact due to the smoothed noise.

Three main substructures are present during this part of the event at $\sim$6100 sec, $\sim$6200 sec and $\sim$6300 sec. To compute their timing the lightcurve at each frequency has been smoothed first with a gaussian having σ=10pts, then with a gaussian having σ=20pts and lastly with a gaussian σ=30pts. The results are shown in Tab.2.2.

The timing of the peak was computed three times, each time with a different level of smoothing. As shown in Tab.2.2, three gaussians with three different standard deviations have been used in order to test the reliability of the computed value. The data provided in the table show that during this phase of the emission the time of the peak is almost uncorrelated with the frequency of observation. All times are almost independent of the smoothing except the 3.75 GHz channel at 6100 sec, where the peaktime shows a jump of 7 sec from σ=10 to σ=20 due to the weak substructure of the peak. These may arise from the spatial complexity of the emission processes involved in the emission. The Nobeyama Radio Polarimeter is a full-disk instrument so the integrated curve cannot distinguish contributions from the local effects except by timing.

Channel	2 (26-50 keV)	3 (50-100 keV)	4 (100-300 keV)
Peak time 1 (s)	5886 ± 2	5889 ± 3	5893 ± 5
Peak time 2 (s)	5933 ± 2	5936 ± 3	5938 ± 5

Table 2.3: Energy dependent peak time of the two peaks in Fig.2.13

2.1.2   *Fermi*/*GBM* Data

The first five channels of *GBM* instrument are shown in Fig.2.10 and Fig.2.11. In both, the signal from the highest channel (i.e. channel 2 and channel 4) have been multiplied by 3 in order to make them visible. The data have been processed through OSPEX to remove the background emission of the Sun.

The NaI scintillators composing the *GBM* instrument have a dead time of $2.6\mu s$ so, if there is an high flux coming from the source, the instrument suffers energetic pile-up as in channel 0 (i.e. if two photons with an energy of 10 keV ,which should be counted in the 4-11 keV channel, arrive with a difference in time lower than 2.6μ, they will be interpreted as a single photon having an energy of ~ 20 keV, so they are counted in the 11-25 keV channel). In fact we can see that there is a local minimum of the emission where there should be a maximum, and if we compare the shape of the emission of channel 0 with that of channel 2, we see that channel 0 shows a sort of mirrored shape of channel 2.

The sudden decrease in flux at about 6850 sec is due to the satellite entering Earth occultation. Channels 0 and 1 are the most affected because the emission at these energies is mostly due to thermal emission from heated material in the corona, and last longer than the emission from the higher energy channels, which trace bremsstrahlung emission from electrons hitting the chromosphere and photosphere. In fact, channels 2, 3, and 4 reach almost the background emission before the satellite enters night-time.

The SNR increases as the square root of the counts, as it should for a poissonian process. So the first five channels have a good SNR, while channels 5, 6, and 7 (which are not shown) have a SNR which is almost equal to 1 and for this reason they are not used in this analysis.

The first four channels are shown in Fig.2.12. The dashed line at 5614 sec represent the instant when the *GBM* instrument triggers, so we know that at least two detectors have seen a signal which is 4.5σ above the background, in the energy range between 50 and 300 keV during the previous 1.024 sec of observation (standard configuration of the trigger).

Channel 0 shows a wide bump coincident with the trigger time, with no visible substructures. Channel 1 and channel 2 show three small bumps having a repetition timescale of about 10 sec, and substructures are visible, with periodicity of about 5 sec. Although channel 3 is dominated by the background in this time interval, very weak signals are visible that correspond to the signals in the other channels.
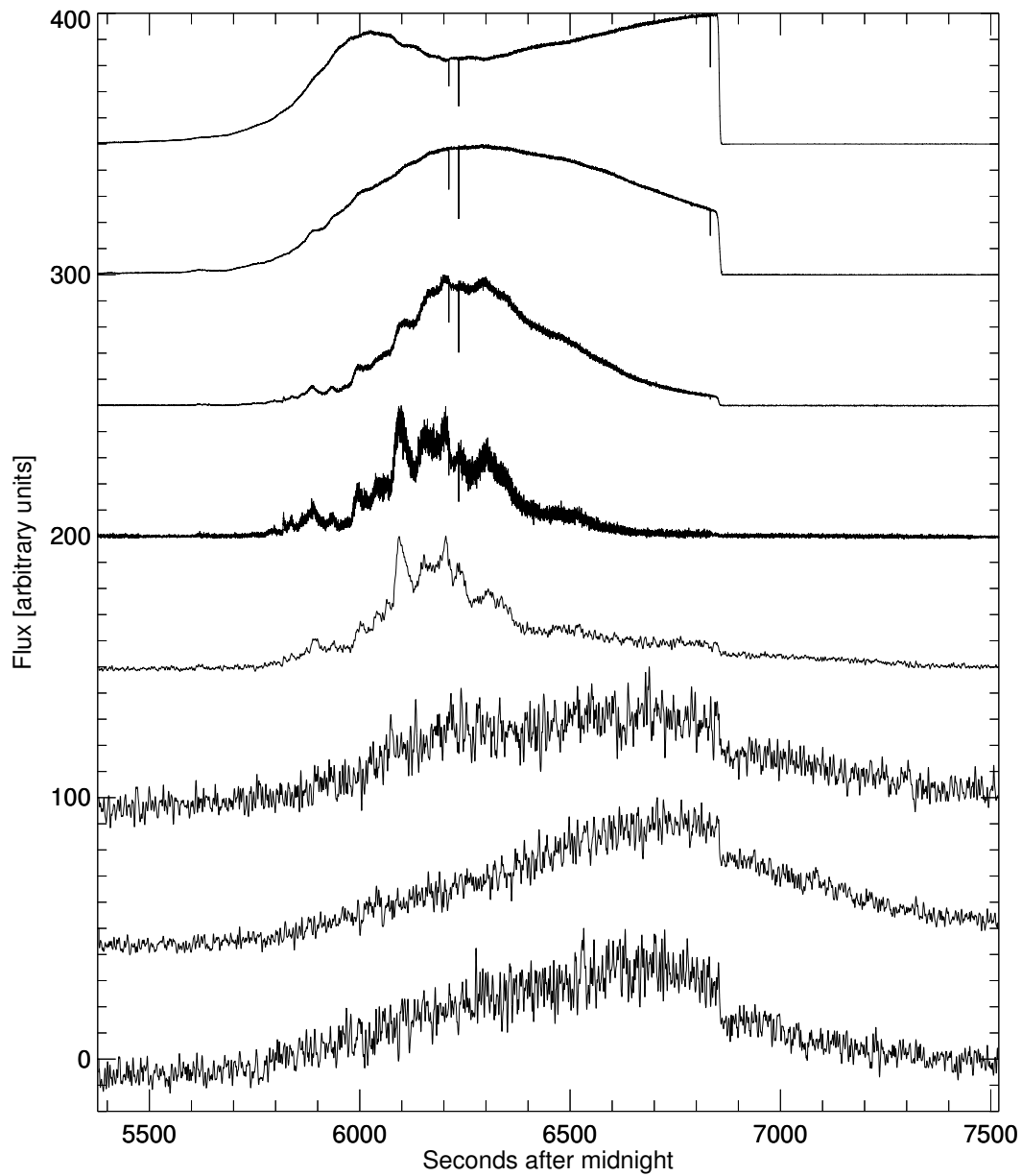
Figure 2.9: The whole dataset from *Fermi/GBM*. The energy channels from top to bottom are: 4-11 keV, 11-25 keV, 25-50 keV, 50-100 keV, 100-300 keV, 300-540kev, 540keV-1 Mev, 1-2 MeV. The last four channel have been smoothed with a σ=10pts gaussian.
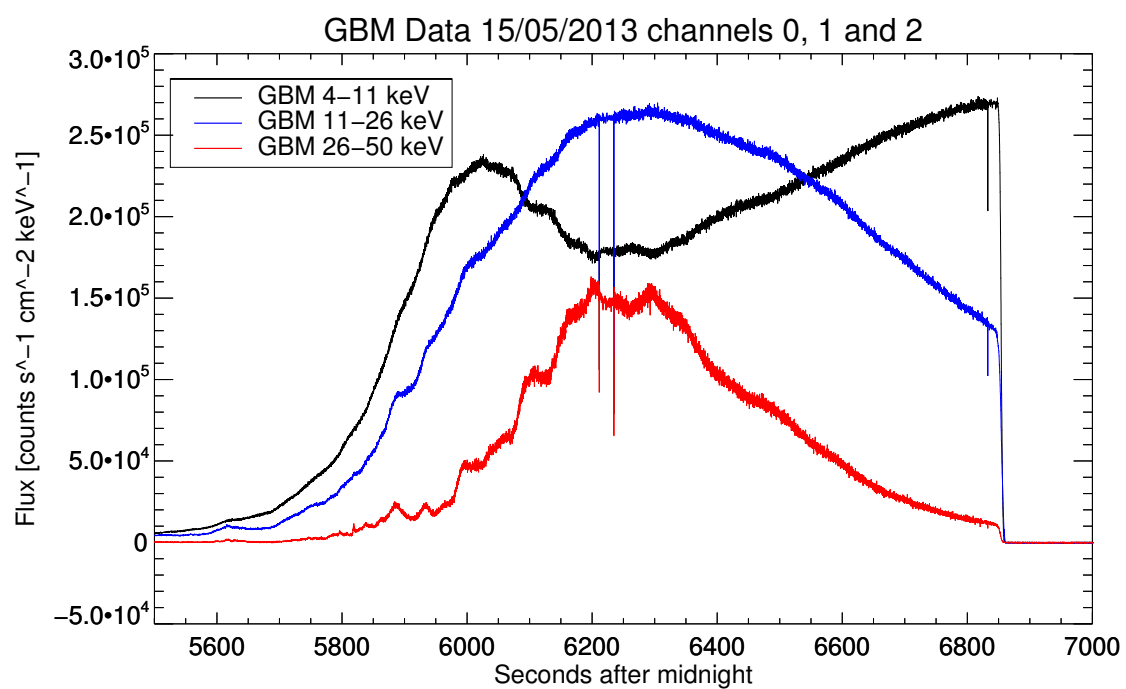
Figure 2.10: Data from the first three energy channel of the *GBM* instrument. Channel 2 has been multiplied by 3 in order to appreciate the substructures. Looking at the timerange between 5600 sec and 6000 sec, channel 0 is the one that has the higher flux, channel 1 is the middle one and channel 2 is the lowest.
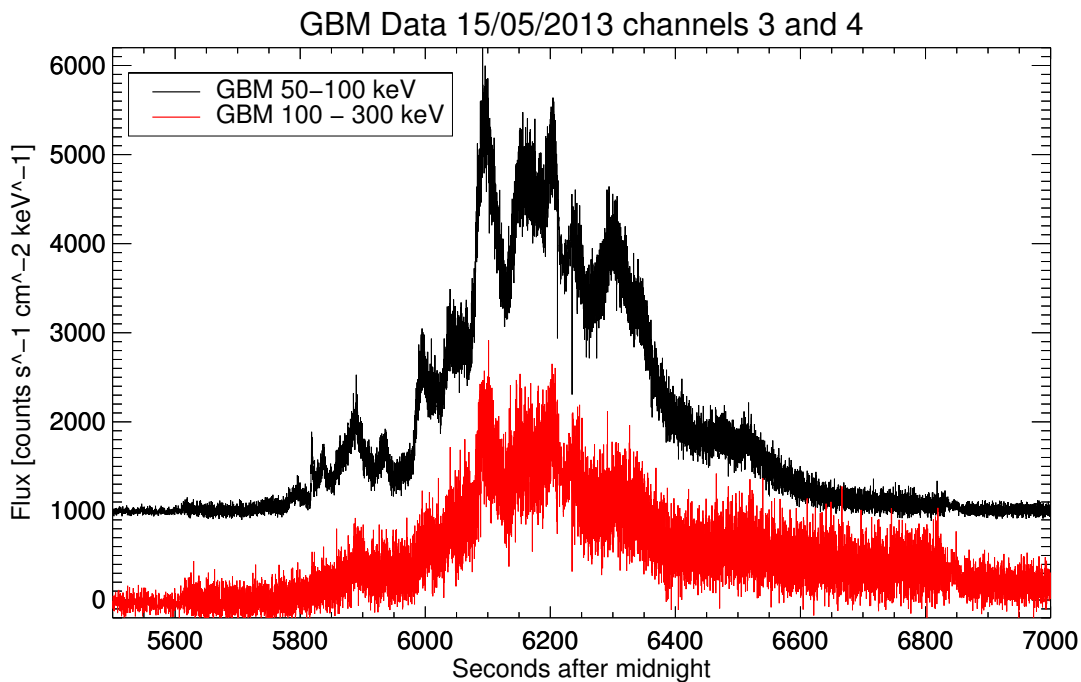
Figure 2.11: Data from the channel 3 and 4 of the *GBM* instrument. Channel 4 has been multiplied by 3 in order to appreciate the substructures. Channel 3 (the higher one) has been shifted 1000 points up to make both channels visible.

Fig.2.13 shows a close-up view of the two peaks already analyzed in radio bands (see Fig.2.6). The graph shows channel 2, 3 and 4 from the *GBM* instrument. The solid line overplotted on the first two channels is the smoothed data. The smoothing was performed by convolving a gaussian with $\sigma = 10$pts, so the 2σ interval covers a time interval of 2 sec since the data have been interpolated on a time-vector having a constant cadence of 0.1 sec.

We see that the peak occurs at later times for higher energies. Tab.2.3 gives the peak-time. Since it is impossible to calculate the peak-time by fitting a function on the data (in fact, we don't know which function is the best to be used for fitting the data, so, whathever function we use, a bias would be introduced), the peak-time and the error interval have been measured by eye. Some substructures are present, but it is difficult to discern which are caused by noise and which are real. However, the interval between the small subpeaks in channel 2 goes from 6 sec to 12 sec. Some of them have possible counterparts also in channels 3 and 4.

Fig.2.14 shows the emission from 25 to 300 keV during the main phase of the flare. Many substructures are visible with durations varying from a few seconds to a hundred of seconds almost uniformly (see also Mészárosová et al. [2011]).

There are three main peaks at 6100 sec, 6200 sec, and 6300 sec, the analysis of which has been done as follow. Since the higher energy lightcurves show more noise than the lower energy one, I've calculated each time of the peaks for three times, the first one after a
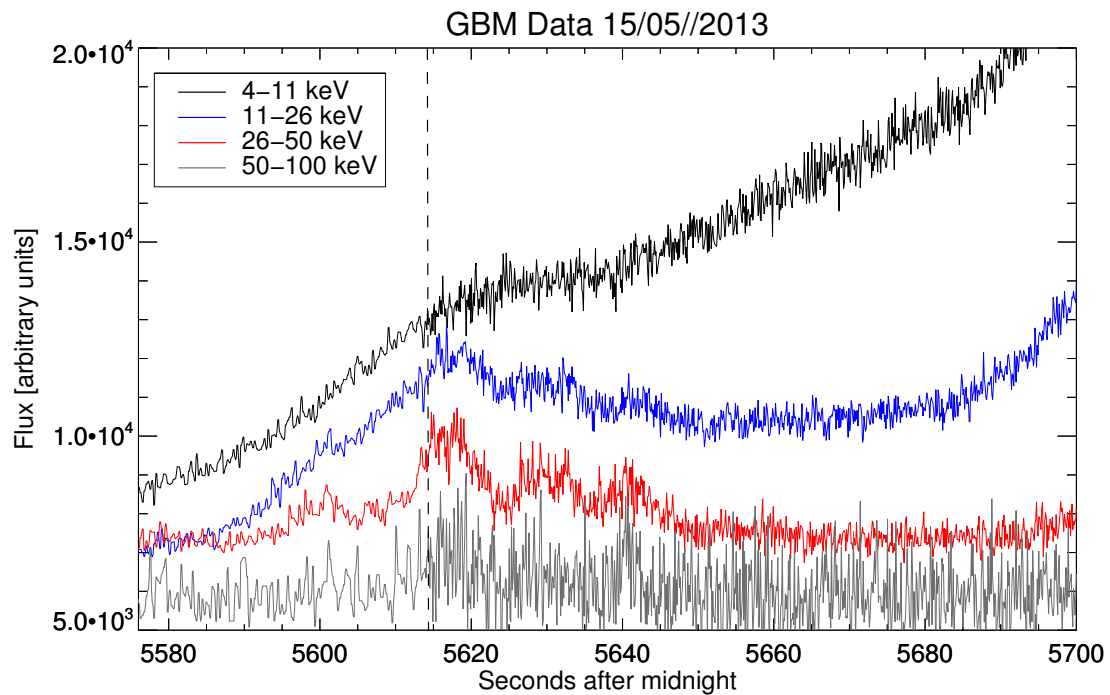
Figure 2.12: Data from the first four channels of *GBM* instrument in the time range between 5580 sec and 5700 sec. A signal is seen in first three channels while channel 3 is dominated by the background (and so it is the channel 4, not shown here) and it is not possible to detect a signal. The vertical dashed line represent the time when the *GBM* triggers the observation. The integration time before the line is 0.256 sec and it is 0.064 sec after the line. In fact is possible to see that the SNR is lower when the integration time is lower. Note that similar features are present in the Nobeyama dataset at the same time, see Fig.2.4
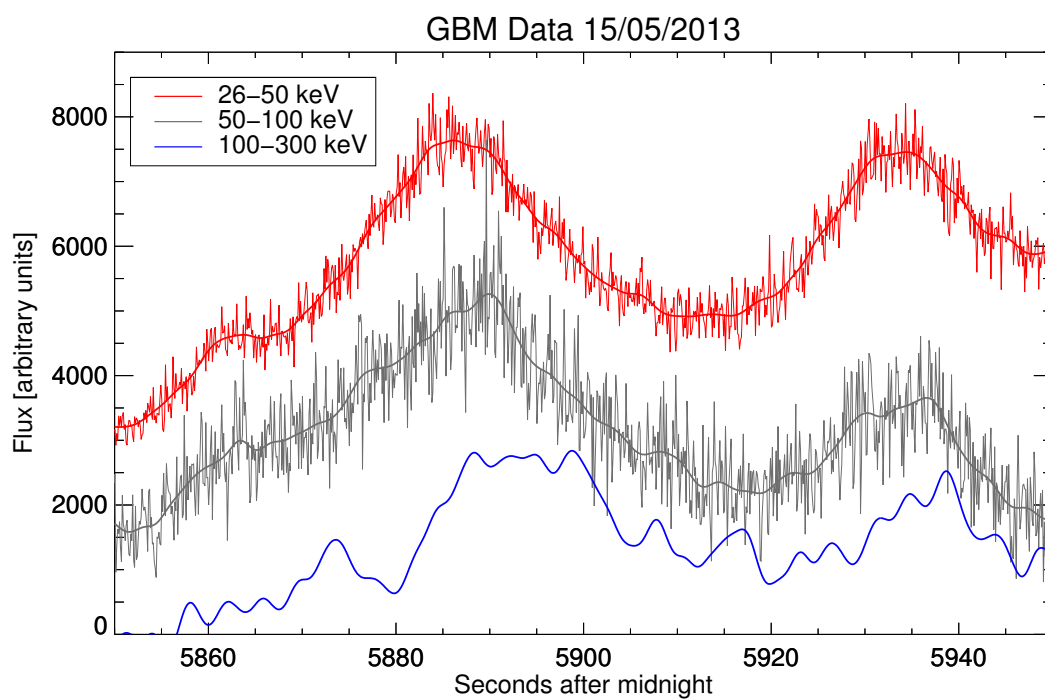
Figure 2.13: Data from channel 2 (original and smoothed), channel 3 (original and smoothed) and channel 4 (just smoothed). The smoothing has been done using the convolution with a gaussian having σ=10. Since the resolution of the data equal to 0.1 sec, the 2σ interval covers a time interval of 2 sec. We can see that, as the energy goes up, the peak shifts forward in time, see Tab.2.3.
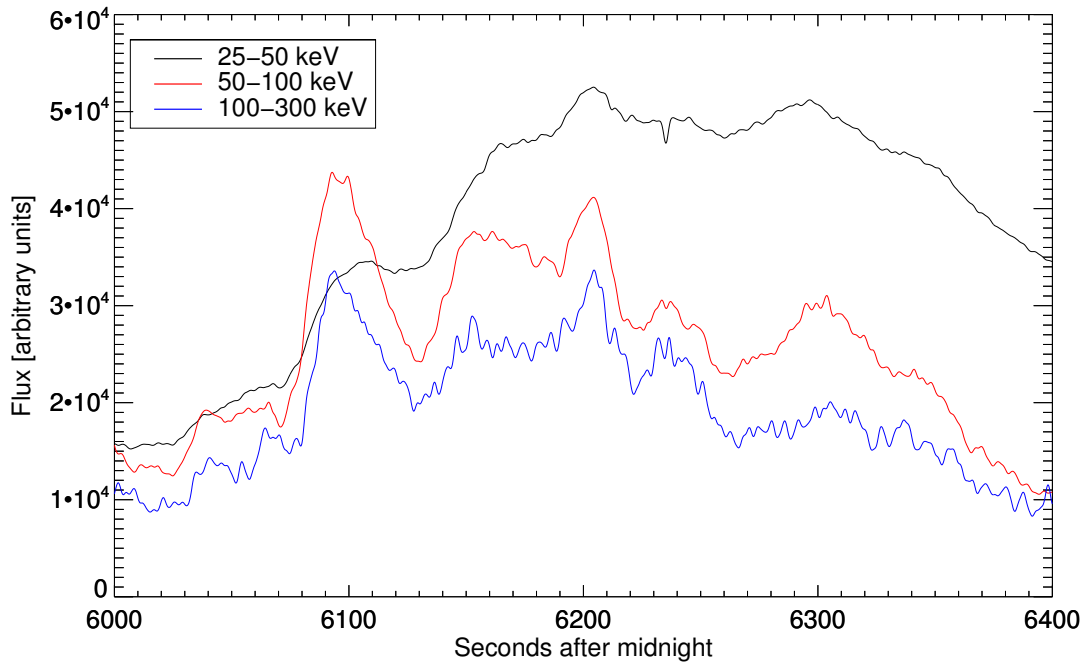
Figure 2.14: Data from channel 2, 3 and 4 from *Fermi/GBM* , smoothed with a gaussian having σ=10pts.

gauss-smoothing with a gaussian having σ=10pts, the second one with a gaussian having σ=20pts and the third with a gaussian having σ=30pts. The results are:

- the peak at 6100 sec shows different behavior in the three channels. Channel 2 shows a slower rise and the peaktime is delayed (the same delay is present during the rise between 6130 sec and 6180 sec), channel 3 presents two small subpeaks at 6092.8 sec and 6099.3 sec and the decay phase is irregular. Channel 4 presents a subpeak at 6093.8 sec and a bump on the decay at 6100.1 sec which may be the counterpart of the peak at 6099.3 in channel 3 (i.e. channel 4 have a delay of about 1 sec). All three channels display subpeaks in the range 6110 sec - 6130 sec and the FWHM calculated for channel 3 and 4 is ∼20 sec. It is worth noting that, since the peak is composite, the measured peaktime is strongly dependent on the degree of smoothing. In fact, for light smoothing, the two subpeaks appear distinct and the peaktime is taken measuring the first subpeak of the two (which is the stronger one). As the smoothing gaussian became larger (increasing σ) the two subpeaks disappear, leaving a single smoothed peak having the peaktime almost equal to the mean of the two;

- the peak at 6200 sec is almost coincident in all three channels, with the peaktime being at 6204.3 sec;

- the peak at 6300 sec is broader and the amplitude is lower. Here, the higher channels

are delayed with respect the lower one. In fact the peak time after a 10pts smoothing
was 6296.7 sec for channel 2, 6303.8 sec for channel 3 and 6305.3 sec for channel 4.
The smoothing with a wider gaussian has only the effect of systematically shifting
the peak earlier, consistent with the fact that this peak marks the beginning of the
decay phase (i.e. what is before the peak, being higher in flux, weights more than
what is after it).

The last phase is the cooling phase. Each energy channel has a characteristic cooling
timescale, and as the energy goes up, the cooling time reduces: for channel 2 the timescale
is ∼265 sec, for channel 3 is ∼82 sec and for channel 4 is ∼64 sec. The lower channels
have still a high emission rate when the satellite enters its night-time so it is impossible to
calculate the timescale.

2.1.3 *SDO/AIA* Data

The *SDO* data show a very complex and braided region. Loops are visible in every band
with the exception of 1600 Å band, because the loops have a very low emission at this
wavelength (see Tab.4.2 for relations between bands, temperature and observed part of the
solar atmosphere). To compare lightcurves in radio, x-ray and the lightcurves in UV\EUV,
a spatial integration was been performed over a box defined by the low-left vertex at [-
912,157] arcseconds and the up-right vertex at [-816,247] arcseconds (which is roughly a
square with a side of 70Mm), in heliocentric coordinates. The area qas chosen to contain
the visible surface and the loops related to the flaring region.

The dataset covers the time interval between 00:30:00 UTC and 03:00:00 UTC, the ca-
dence is variable from 12 sec to 24 sec.

The first frame (see Fig.2.15) shows the complexity of the region in the pre-flare phase.
The upper photosphere (panel *a*) shows that the region is quite active: the average emis-
sion is higher in the active region than in the other parts of the surface. There is some
mechanism that is heating the photosperic plasma and we are seeing the cooling. The
other bands show many emitting loops which that are filled by gas at the temperature to
which each filter is sensitive, traced mainly by Fe ions (see Tab.4.2 for the correspondence
between wavelength, temperature and degree of ionization of Fe ions and Sec.4.2.1 for an
explanation of the process involved).

The frames shown in figure Fig.2.16 illustrate that the photosphere emits the bulk of the
energy, deposited there through thick-target bremsstrahlung by the particles accelerated in
the reconnection process, from small regions coincident with the point where the loops
enter the photosphere (i.e. the *footpoints* of the loops, see also Fig.2.19). There are small
bright points coincident with the intersection between the visible surface and the loops, the
integraton over which gives us the lightcurve in band 1600 Å described later.

This is expected since the electrons (which have been energized by the reconnection
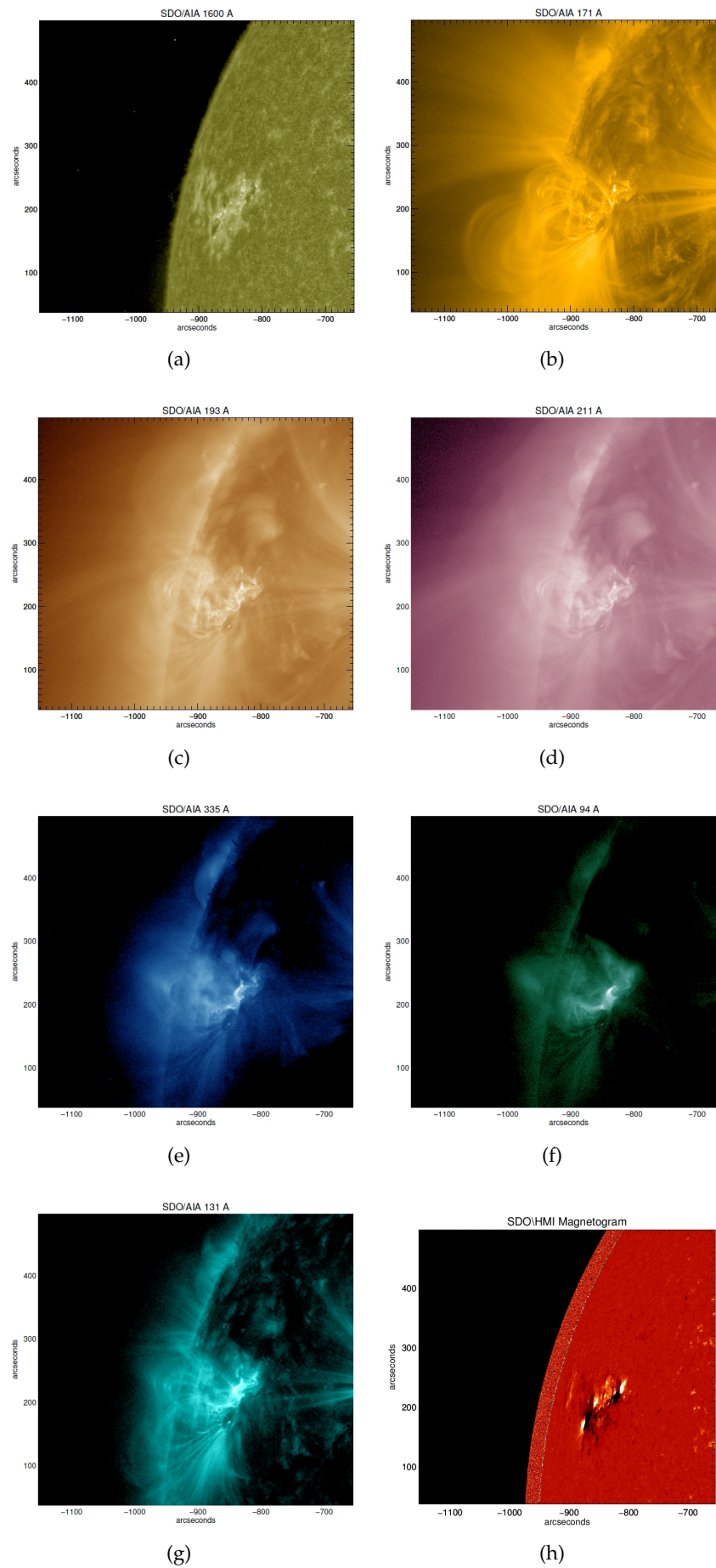
Figure 2.15: *SDO/AIA* data in different bands. The first frame in each band is shown. The time of the observation is 00:30:00 UTC
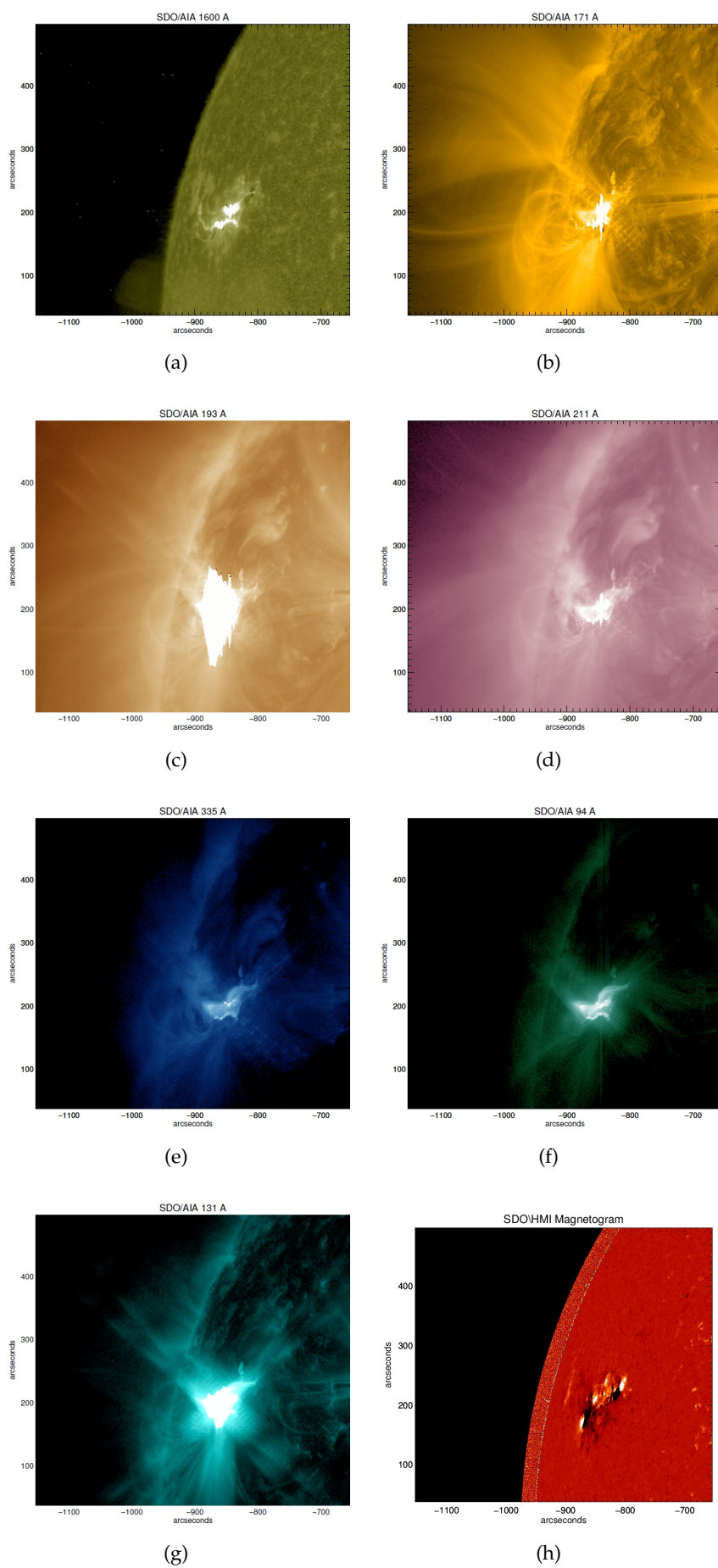
Figure 2.16: *SDO/AIA* data in different bands. The frame shown here correspond to the frame taken during the impulsive phase of the flare. The time of the observation is 01:41:50 UTC
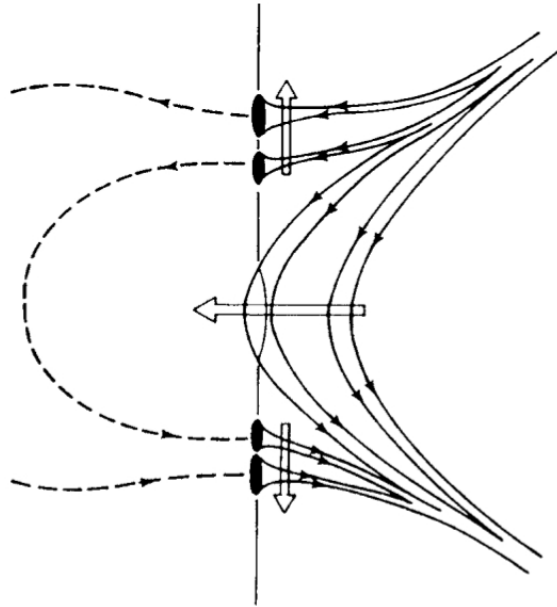
Figure 2.17: A schematic view of the emergence of flux. The large arrows indicate the motion of the loops. From Zwaan, C. 1992. In *Sunspots: Theory and Observations,* , ed. J.H. Thomas and N. O. Weiss, p.75

process) flow along the loop arms and deposit all their energy in the photosphere and lower chromosphere. The loops are visible in the EUV data, (from panel *b* to panel *g*), while the footpoints are, in general, always visible.

Unfortunately, the AIA instrument is so sensitive that during the impulsive phase of M-class and X-class flares most of the bands saturate. In fact, the only not-saturated bands are 335 Å (panel *e*) and 94 Å (panel *f*).

During the impulsive phase we also see that the group of loops having their looptop around [-950,230] seem to be expelled, creating what is called a Coronal Mass Ejection (CME), which has been observed by SOHO [2].

Panel *h* shows the data from HMI (the scale ranges from black (negative flux) to white (positive flux), passing through red which is the zero). The footpoints where the magnetic

---

[2]See http://cdaw.gsfc.nasa.gov/movie/make_javamovie.php?date=20130515&img1=lasc2aia193

flux is positive is situated at a higher latitude with respect to the flaring region, while the negative one is at lower latitude (this is consistent with the polarity of the solar cycle 24[3]). Using the model shown in Fig.2.17, these loops may be related to the same underlying structure which is buoyantly emerging from the photosphere.

Fig.2.18 the last frame of the observation is shown. We see that a whole arcade lights up, the two lines of footpoints at the base of the arcade move apart indicating that the arcade expands in the corona. The first two looptops (from left to right) continue to emit very strongly during the cooling phase (i.e. the phase that comes after the impulsive heating phase which is defined by the X-ray emission), while the rest of the loops show faint emission along the whole loop.

The comparison between lightcurves in EUV and UV is shown in Fig.2.20 and Fig.2.21. The emission from the lower coronal transition region (band 1600 Å) is very different from the others since it shows only what happen on the visible surface of the Sun (in this band) and also because, as said earlier, the loops do not emit at the wavelength of this filter. If we compare this lightcurve with that from the footpoint X-ray emission, we notice that every feature that has a timescale equal or longer than the temporal resolution of the instrument (i.e. 24 sec at this wavelength) is present (see also Section 2.2 and Fig.2.27).

What can be seen in these plots is that the footpoints are visible in most band with the exception of 193 Å , 131 Å and 94 Å because in 193 Å and 131 Å the saturation hides the emission from the footpoints and in 94 Å they are very faint. Band 193 Å is the most affected by the saturation, in fact during the flaring time, almost every pixel in the box is affected by saturation so the curve has a plateau from 6000 sec to 6500 sec. Band 171 Å and 211 Å are the most interesting, showing a feature that seems to be present in flares ending with an arcade: the peak of the emission has a modulation that mimics the footpoint emission modulation, but delayed by 758 sec (taking as reference the impulsive emission). Similar structures may be the one delayed by 769 sec from the previous one and the one at 926 sec.

Fig.2.22 shows the mean magnetic flux compared with the lightcurve from the lower coronal transition region. The mean magnetic flux per pixel changes during the time of the observation: it shows a slow decreasing of the modulus of the flux from the beginning of the observation to ∼5800 sec, when the reconnection occurs and there is a sudden increase of the flux, probably related to the relaxation of the magnetic field and emergence of flux (see sec.3.6). The slow rise in flux at the beginning may be due in part to the changing in orientation of the surface of the Sun (since the observation measures the field along the line of sight).

The *SDO* data are also very useful to add the spatial information to the time-resolved information from *GBM* and *NoRP* since we can take the lightcurve of every single resolved element on the surface (i.e. a square at least 2x2) to check whether any of the features seen

---

[3]see http://solarscience.msfc.nasa.gov/SunspotCycle.shtml
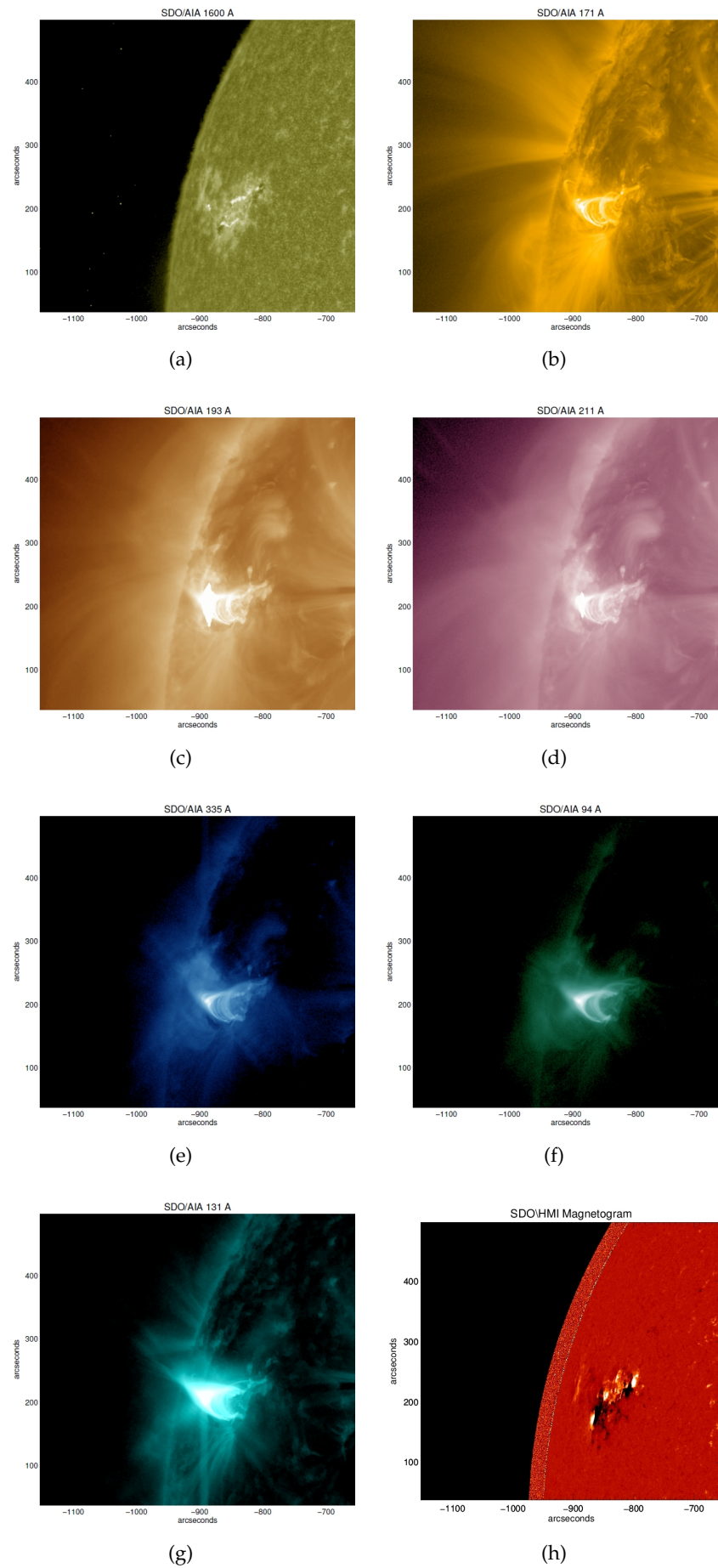
Figure 2.18: *SDO/AIA* data in different bands. The frame shown here correspond to the last frame of the observation. The time of the observation is 03:00:00 UTC
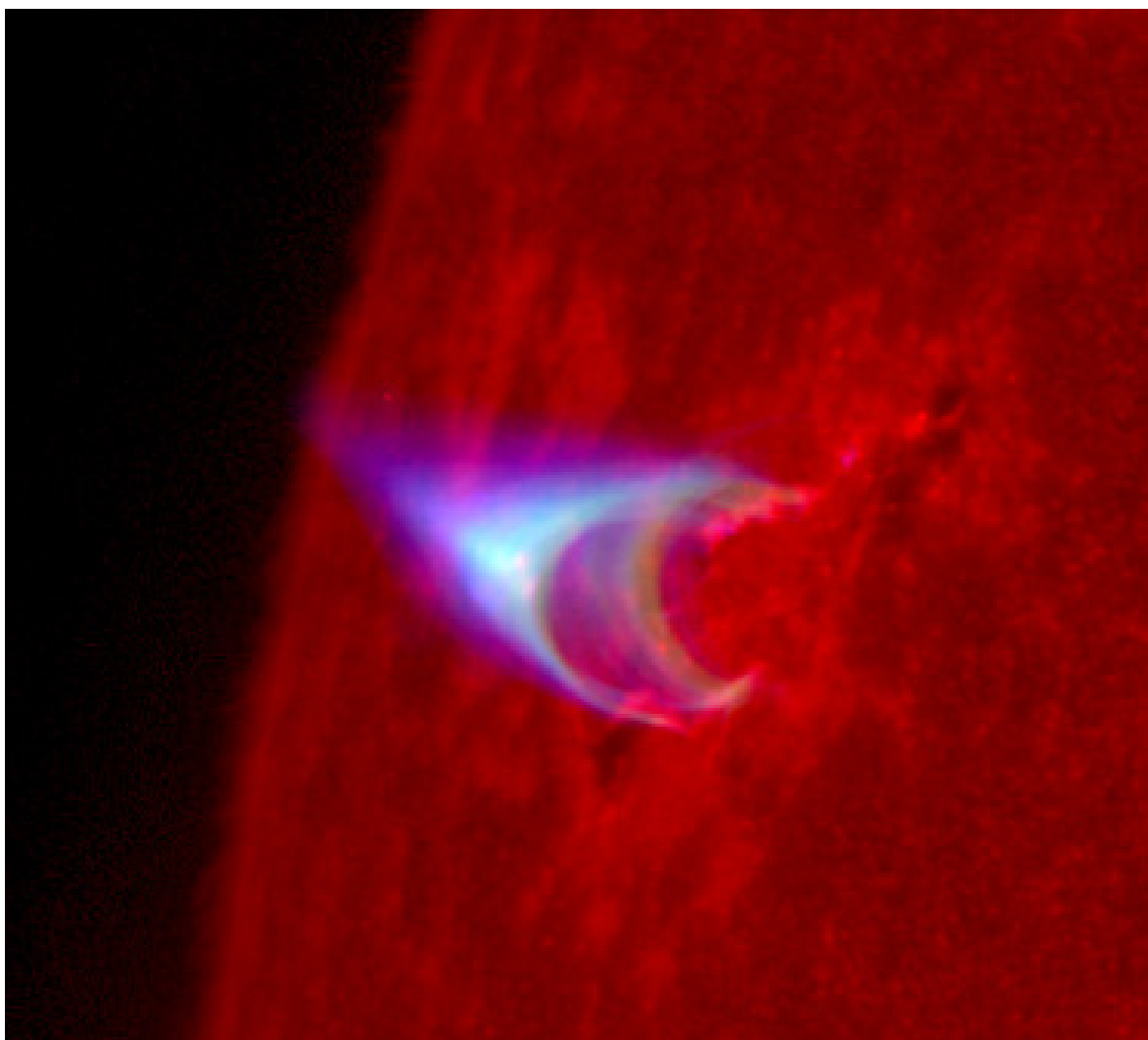
Figure 2.19: Composite image where band 1600 Å represent the red layer, band 94 Å the green one and band 131 Å the blue one. It has been created using the last frame of observation for each band, when the arcade is already developed and the footpoints are still emitting. The distance from the lower right pixel and the limb is 302pix which is equivalent to 181.2 arcseconds.
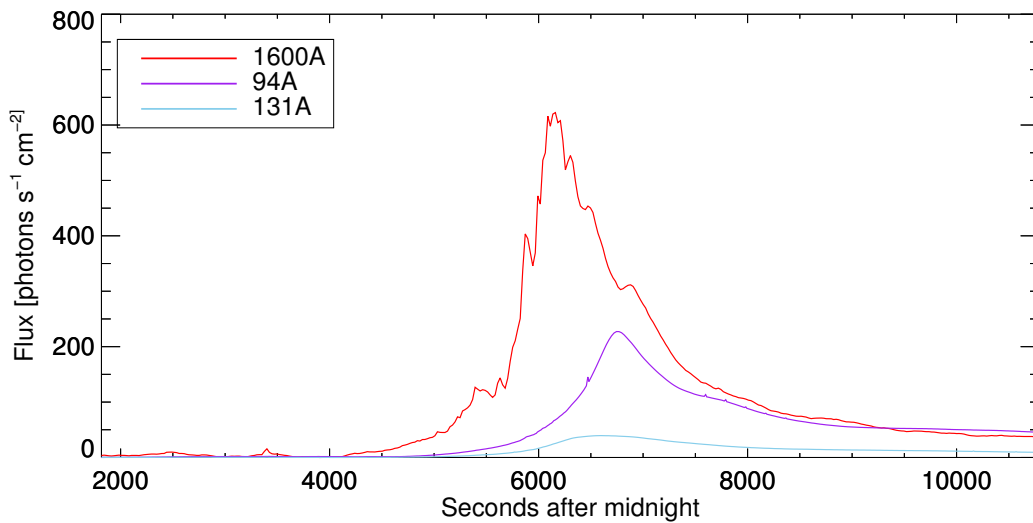
Figure 2.20: Data from *SDO/AIA* instrument. The lightcurves have been taken by integrating on the whole active region, keeping the loops related to the flare in the box of integration. The box is defined by the low-left and up-right vertices which are [-912,157] and [-816,247] arcseconds, in heliocentric coordinates.
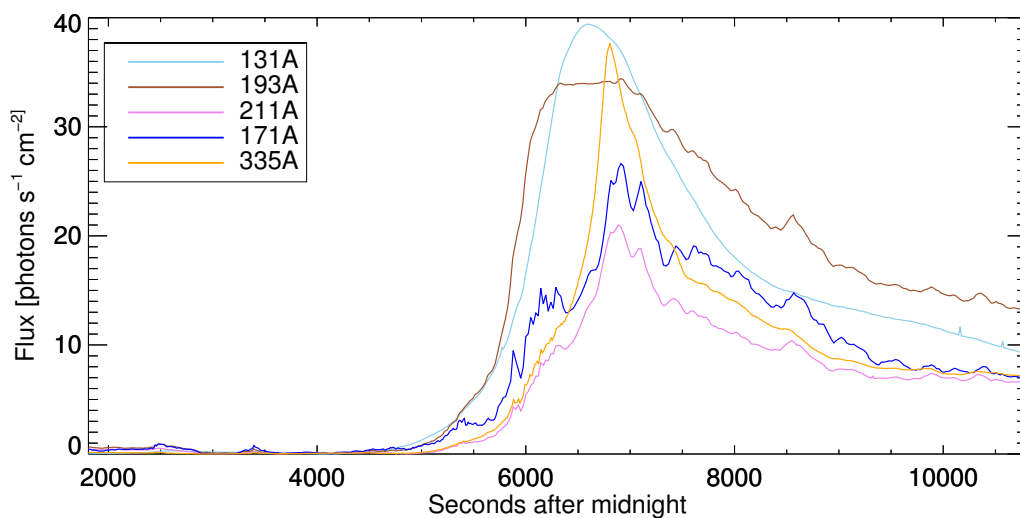
Figure 2.21: Data from *SDO/AIA* instrument. See caption of Fig.2.20 for the explanation about the integration. The bands plotted here show the emission from both footpoints (in the rising part of the emission,from 5500 sec to 6500 sec) and loops. The lightcurve of the band 131 Å has been also plotted here in order to be able to make a comparison between the two figures.
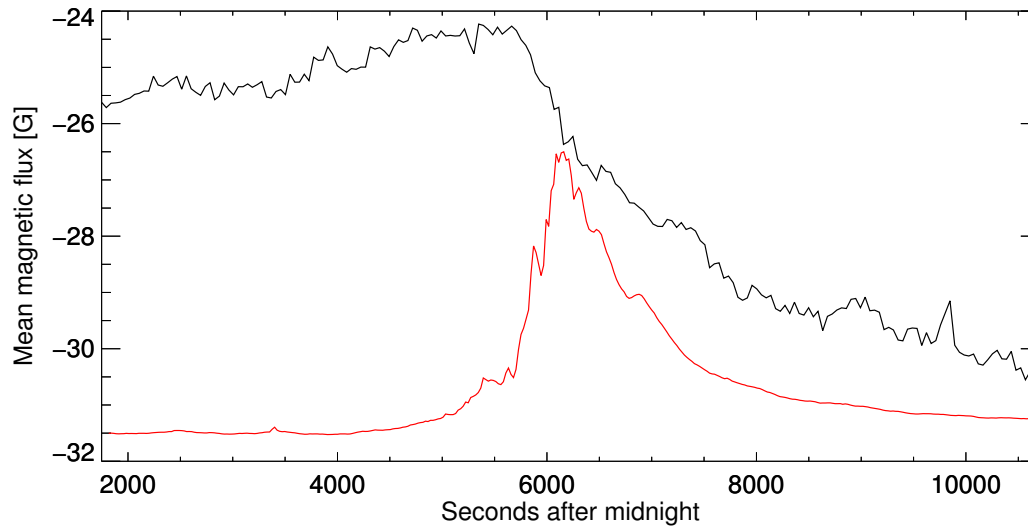
Figure 2.22: Data from SDO\HMI instrument. The black line represent the mean magnetic flux from each pixel, weighted over the whole area of integration, which goes from [-912.6,157.5]arcsec to [-792,247.5]arcsec. There is a slow drift upward from 2000 sec to 5500 sec when the reorganization take place, marked by the sudden drop in magnetic flux, coincident with the emission coming from the footpoints, indicating that the reconnection event has happened

in the *GBM* and *NoRP* lightcurves are coming from a single region. In order to do that, I have used the procedure *aac_sdolightcurve.pro* (see sec.A.1) for the 1600 Å data. I selected an 8x8 matrix of points covering the part of the flaring region corresponding to the upper footpoints of the arcade, as shown in Fig.2.23. Then every vertical line of boxes have been summed, obtaining eight lightcurves, one for each vertical line.

The procedure tracks the motion of the solar rotation (eastward) so the coordinates of the projected points vary during the whole observation. The reason why a matrix of points has been taken (instead a single line along the footpoints line) is because a problem arises in doing this kind of integration: the point responsible for the emission may also move in the upward direction due to emergence of an arcade or because the structure of the arcade is similar to what Magara and Longcope have simulated (see sec.3.6): the hypothesis is that the footpoints of the purple loop light up first, and, after that, so do the footpoints of the yellow loops. Then the heated material evaporates and fills the whole arcade, producing the emission seen in EUV (lightcurves in Fig.2.21).

The procedure *aac_sdolightcurve.pro* can perform a gauss-smoothing of the image before calculating the lightcurve. This is done because the Sun rotates continuously, whereas the procedure follows the points in a discrete way and smoothing is needed to avoid artifacts due to the jump from one pixel to the adjacent one. The gauss-smoothing performed here has a σ=1pix and, since the procedure removes from the gaussian kernel any contribution less than 10^{-4}, the kernel matrix has a dimension of 7x7 pixels, centered on the selected

(a)   (b)

(c)
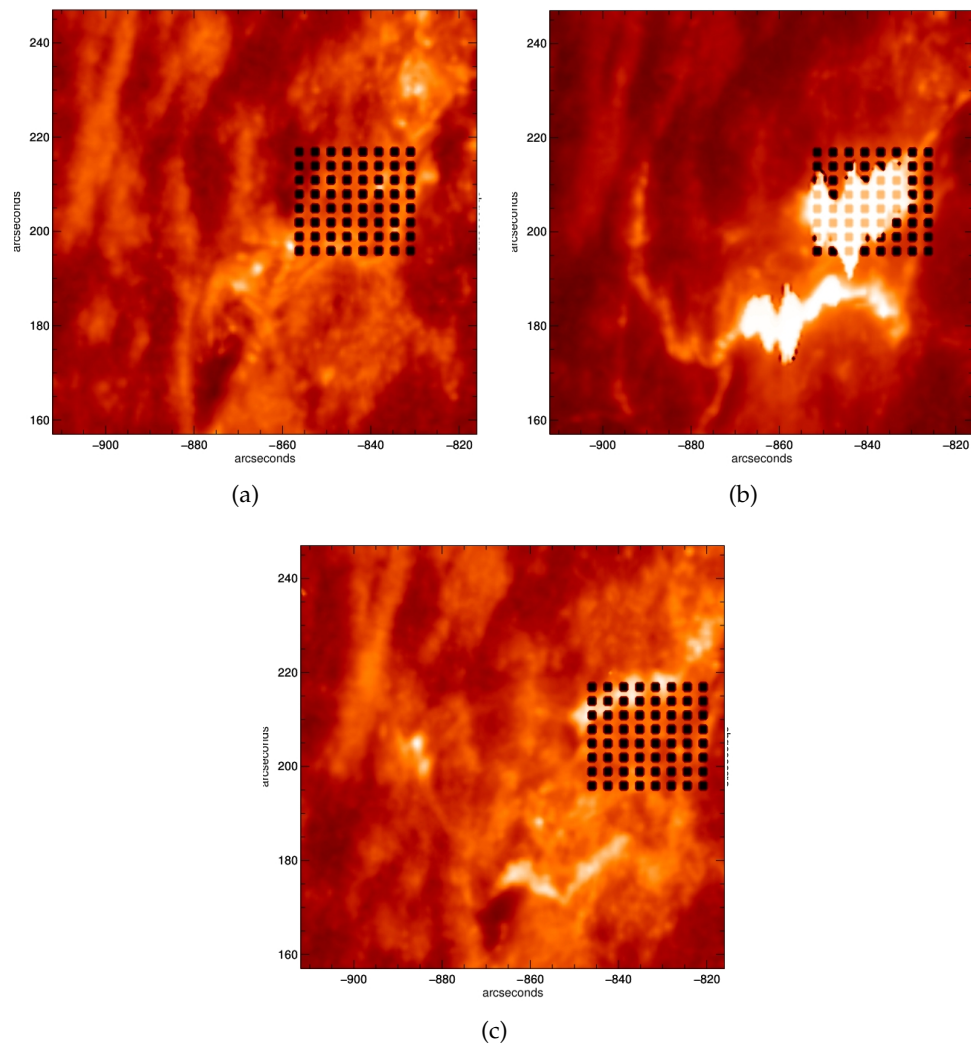
Figure 2.23: The three panels show a cut over the active region in band 1600 Å at three different instants: a) beginning of the observation; b) flaring time; c) last frame of the observation. The black squares encircle seven 3x3 boxes, and for each one of them the lightcurve has been taken. Then every vertical line of boxes have been summed not to loose any feature of the emission due to de shifting upward of the emission point. The results are shown in Fig.2.24. I'll refer to each inntegrated vertical line, from left to right, with letters from A to H.
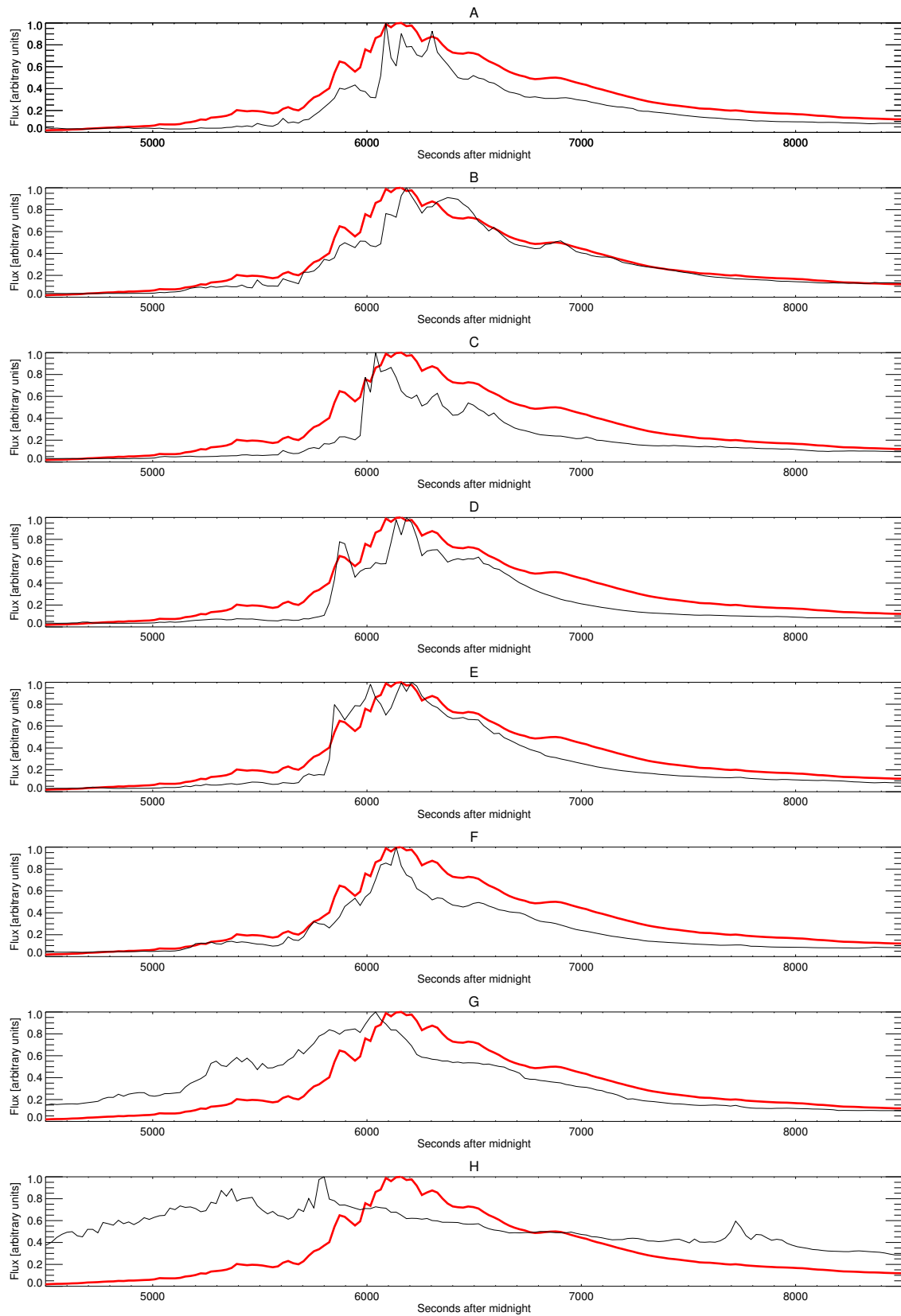
Figure 2.24: Red line represent the lightcurve taken from the band 1600 Å images. Each black line represent the lightcurve of each vertical set of points of the mask shown in Fig.2.23. The lightcurve of each point has been calculated using the procedure *aac_sdolightcurve.pro* integrating on a 3x3 box, after the smoothig with a gaussian having σ=1pix.

point of integration. Thus, only the last line of pixel of the kernel overlaps with the kernel of the adjacent point of integration, so, each single lightcurve is almost independent from all the others.

The result of this integration is shown in Fig.2.24. Each plot from the A to H corresponds to a integrated North-South (NS) line of points, from left to right. The first result we have from this series of plots is that the footpoints line lights up in a sort of sequence going from right to left and there are structures that appear in some lightcurves and are not present in others.

The overall behavior is:

- the feature at ∼5900 sec is strong in E and D. F shows a gradual rise till ∼6150 sec, while G, even though has a strong presence of noise (because it is at the left end of the footpoints region), shows stronger emission in the first half of the lightcurve (till ∼6050 sec)

- then, at ∼6000 and ∼6050 sec, there are two features in the rising part of the main emission which are very strong in C, and there is weaker (but not absent) emission in E, F and G;

- at ∼6100 sec the only strong part of the footpoint region is A, so this peak is very localized;

- from ∼6150 sec on, the emission is dominated by the regions A, B, D, and E in a sequence that seems to be: D+F (∼6150 sec), then A+B+E (∼6200 sec), then A+B again (∼6300 sec).

Finally, the hypothesis that the particle are accelerated in a single region at the looptop and then stream along the two arms of the loop before depositing their energy at the footpoints can be tested by the computation of two lightcurves each of them containing one of the two line of footpoints.

The results of the computation are shown in Fig.2.25. The three lightcurves are highly correlated. In fact, taking every combination of two curves out of the three, we obtain a correlation coefficient equal to 0.99. Thus **the two region must be causally connected**, i.e. each pair of footpoints have a unique acceleration point, which is likely to be situated at the looptop. Then, the accelerated electrons stream along the arms of the loop, reaching the denser photosphere and loose all their energy by collisions. Then the two lightcurves are simultaneous, within the 24 sec cadence of the instrument.

2.1.4 RHESSI Data

The *RHESSI* satellite provides spatial information about the X-Ray emission in different energy range, with the advantage that most of them overlap with the bands at which *Fermi/GBM* observes.
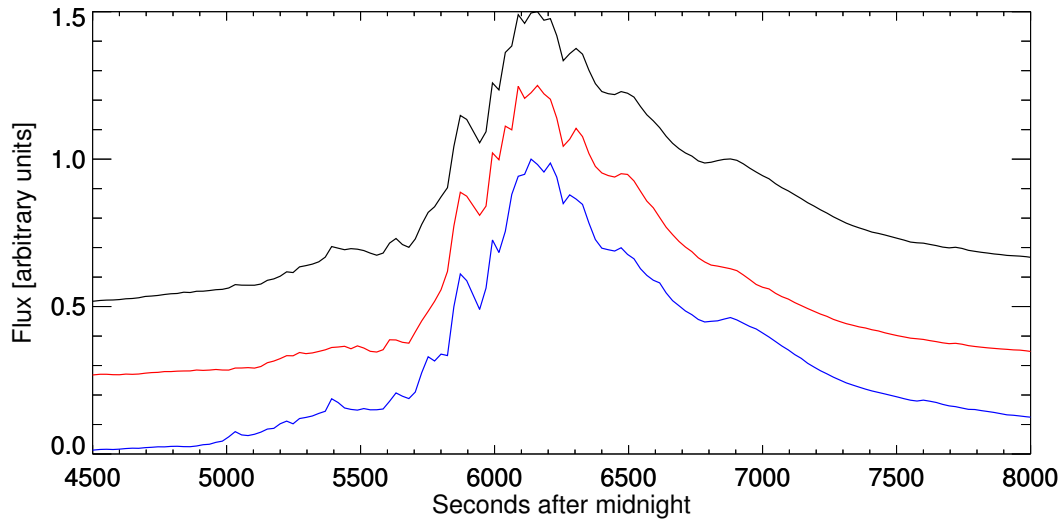
Figure 2.25: Comparison between the lightcurve from the whole region (black line with 0.5 vertical offset), the lightcurve from the upper footpoints (red line with 0.25 vertical offset) and the lightcurve from th lower footpoints (blue line starting from 0). The three lightcurves are highly correlated: the correlation coefficient of each pair of the three is 0.99, so we can say that the events are happening simultaneously. The lightcurve from the upper footpoints has been taken integrating over the box [(-880.8,191.7),(-847.8,217.5)] arcseconds and for the lower footpoints the box of integration is [(-901.2,169.5),(-870.0,190.5)] arcseconds.

We see in Fig.2.26 that the spatial behavior of the emission is consistent with the model shown in Fig.1.4.

The emission is quite asymmetric and the reason for this has been studied by Yang et al. [2012] who explain it by differences in the magnetic configuration at each side of the loop creating an asymmetric magnetic bottle. If the trap is asymmetric, one of the mirror points is lower in the atmosphere, where the the density is higher causing the loss of orthogonal momentum and then precipitation. They say, however, that they cannot rule out other processes such as transport effect and coronal acceleration processes.

2.2   Comparison between datasets

Our central problem is to understand if the particles that cause the radio emission are, for instance, the same responsible for the X-ray and UV emission or there are other mechanisms (or particles) that cause the observed emission. This can only be addressed by inter-comparing multiwavelength data with different physical sensitivities. First, in Fig.2.27, we see a direct comparison between radio, UV and X-ray emission.

First thing that we see is that almost every feature is present in the three lightcurves, with the restriction that the 1600 Å lightcurve has a cadence of 24 sec, so it is impossible to resolve structure having a timescale lower than 48 sec.

(a)

(b)

(c)
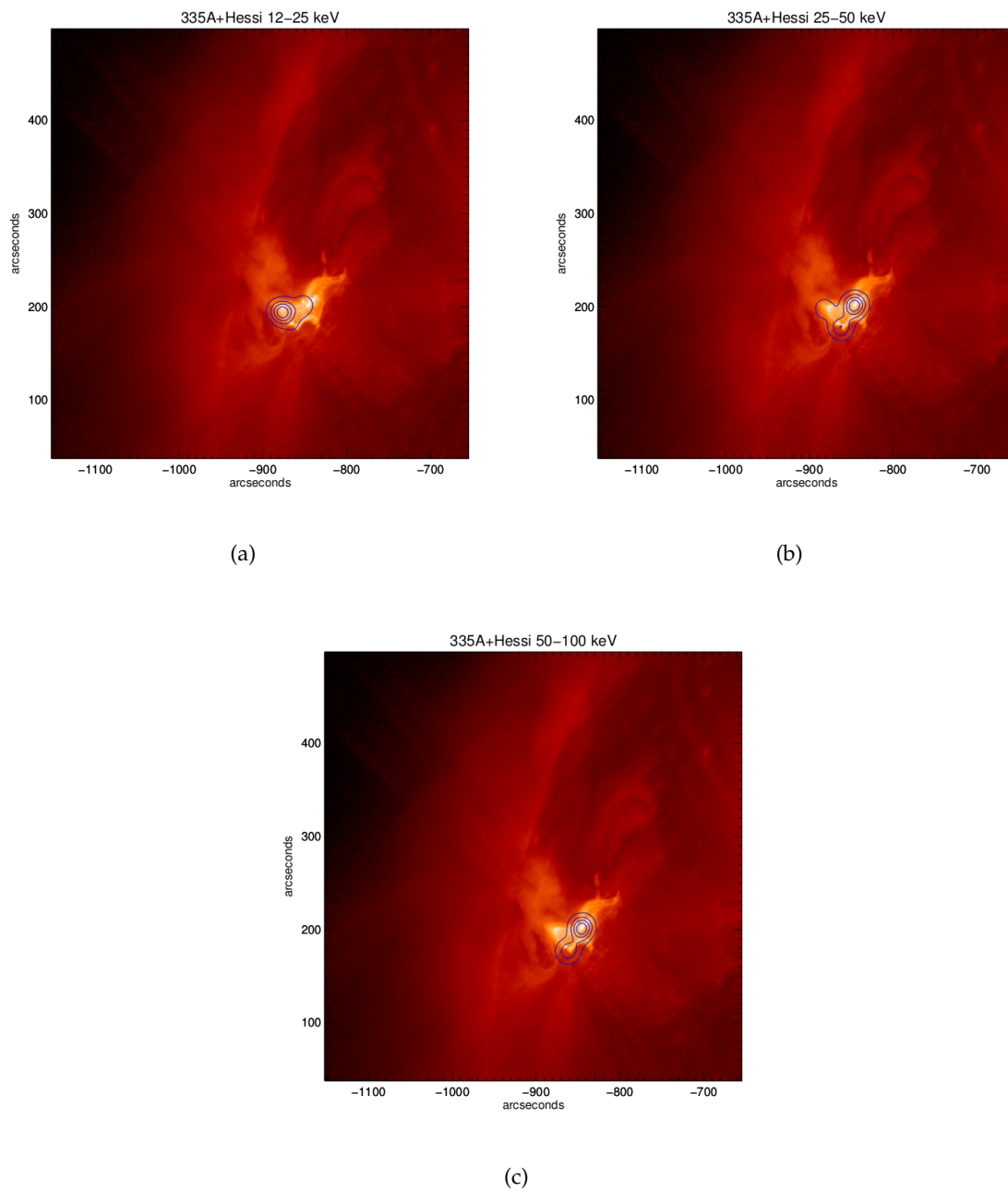
Figure 2.26: Comparison between data from AIA and *RHESSI* (blue contour plot). The AIA data are in band 335 Å for all the three panels. The energy bands of *RHESSI* data are: a) 12-25 keV; b) 25-50 keV; c) 50-100 keV. We can see that soft X-ray emission comes mainly from the looptop, while hard X-ray emission comes from the footpoints of the loops. Contour levels at 20%,40%,60%,80%
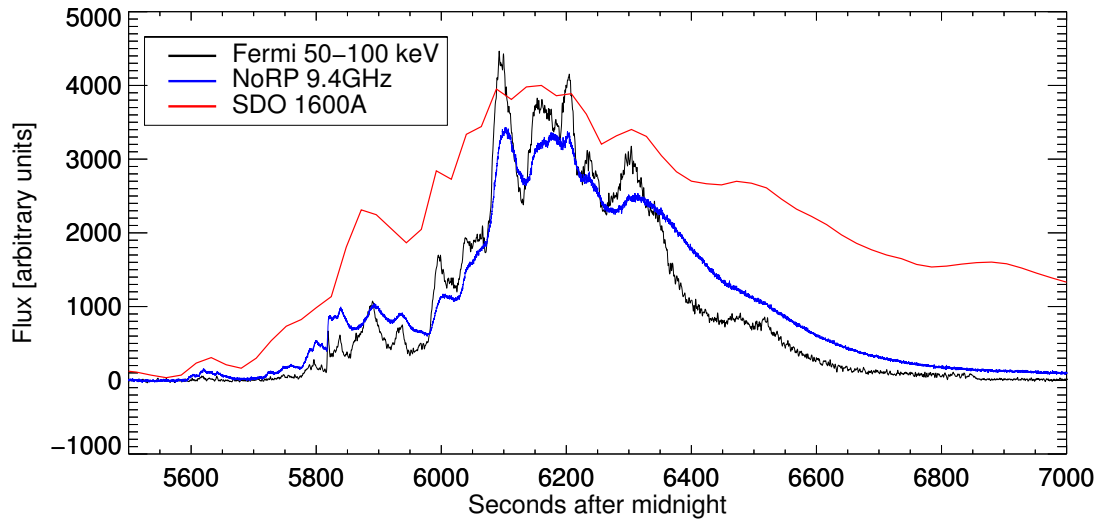
Figure 2.27:   Comparison between the data in radio (blue line), X-ray (black line, 5pts gauss-smoothed) and the integration over the whole flaring region in UV using *SDO* (red thick line).

The feature at ∼5600 sec corresponds to the *GBM* trigger. At 1600 Å it lasts for ≈120 sec (i.e. 5 frames of observation) and resembles a small single peak. At both radio and X-ray energies the emission is composed of four small peaks. The separation in time between the peaks is, respectively, 18 sec-10 sec-12 sec in **both** lightcurves which is very similar to the delays we find in the small structures at ∼5800 sec. Moreover, the radio peaks have a constant delay of about 1 sec with respect to the X-rays.

The observation at 1600 Å also shows the ensemble of structures between 5800 sec and 6000 sec (but here is a single structure), the peaks at 6000 sec, 6050 sec, 6100 sec, 6150 sec, 6200 sec and 6300 sec. The last broad peak (in 1600 Å) at 6900 sec corresponds to the evaporation flow. The agreement between 1600 Å emission and those in radio and X-rays points to the footpoints having an important role in the X-ray and radio emission. The *RHESSI* images show that **the X-rays emission in the range 3-25 keV comes mainly from the top of the loops and the emission from 25 keV on is coming from the footpoints**.

The loops are optically thin in most of the EUV bands, so almost every lightcurve in EUV contains a contribution from the underlying footpoints. This is important because the EUV bands have a cadence of 12 sec (while 1600 Å has a candence of 24 sec) and it is possible to distinguish structures with a resolution of 24 sec that still are coincident with the same structures in radio and X-ray.

No evidence is present for enhanced radio emission from the looptop, comparable with the one beginning at 7000 sec on in *SDO* (see Fig.2.21). No data are available from *GBM* after 6850 sec because the satellite enters its night-time, while the lightcurves from *RHESSI* do not show any substantial emission during the EUV loop emission. Thus the impulsive acceleration of particles had ended and the loop emission must be due to evaporative flow

that fills the loops.

2.2.1   Comparison between X-ray and Radio

Beside the correspondence between *SDO* and other wavelengths, theres a striking corre-
spondence between short timescale structures in X-ray and radio. Fig.2.6 and Fig.2.13
show the first two peaks, which were analyzed in detail in both X-ray and radio and the
time analysis is reported in Tab.2.1 and 2.3. Both peaks show 9 sec of delay between the
earliest peaktime (which for both peaks is at channel 2 from GBM) and the last one (which
is in radio, at 2 GHz) but, even though there is such a difference in time, is evident that the
structure is caused by the same population of electrons interacting with both the magnetic
field and the surrounding plasma.

It was not possible to analyze the relative shifting in time of each peak with cross
correlations because the only way of doing that required cutting out each peak from the
lightcurve and computing the cross correlation; this process created some biases due to the
fact that the cut produced a jump at both the beginning and end of the peak, that affected
the correlation coefficient.

The best possible measurement was to cross correlate the entire vector to check whether
the emission bands had a systematic relative shift. For the X-ray emission, the lightcurve
between 50 and 100 keV was taken as the referent because it showed the emission nearest
to the footpoints with an acceptable level of noise that let us distinguish all the features.
For the radio emission, the lightcurve of reference was the 9.4 GHz because that was the
spectral peak.

To improve the sensitivity of the cross correlation algorithm, I followed the technique
used in Cornell et al. [1984b] and de-trended the lightcurve using an high pass filter. My de-
trending method consisted in smoothing the lightcurve with a Gaussian having σ=500pts,
enclosing an interval of 1000pts (i.e. 100 sec, because 1pt is equivalent to 0.1 sec) in one
$\pm\sigma$ range. The heavily smoothed lightcurve was subtracted from the original that had al-
ready been smoothed with a gaussian having a σ=3pts (shown in Fig.2.28). The result
is in line with what we have found for the peaks around $\sim$5800 sec: **the radio is consis-
tently delayed with respect to the x-ray, with low frequency having the maximum delay
and high frequency the minimum; low frequency radio emission is delayed with respect
high energy emission**.

I also used two different standard deviations for the gaussian kernel to check whether
the results were affected by a change in the kernel. As listed in the table, the change in
the kernel does affect the computed delay. This is mainly due to the fact that a narrower
gaussian kernel filters out a lot more low frequency features, and leaves us with those at the
high frequency (some of which are artifacts). As seen in Fig.2.30, the detrended lightcurve
with σ=100pts (lower panel) is more affected by noise and lacks of the broad peak at 6300
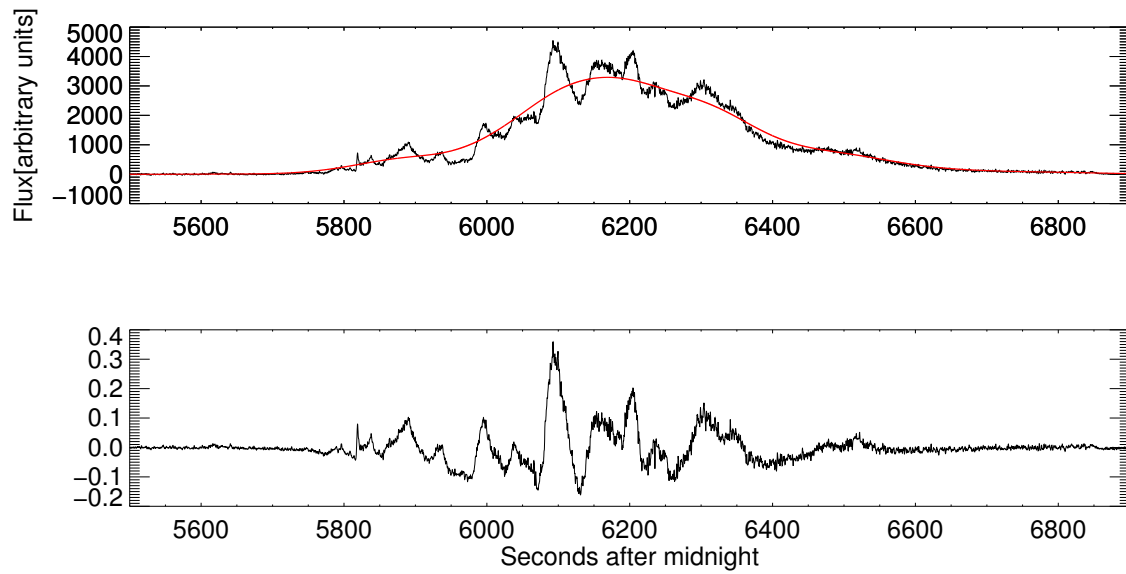
Figure 2.28:   Upper panel: original lightcurve from channel 3 of *GBM* (black ine) and the same lightcurve smoothed by mean of a gaussian having σ=500pts (red thick line). Lower panel: result of the subtraction of the smoothed lightcurve from the original one.
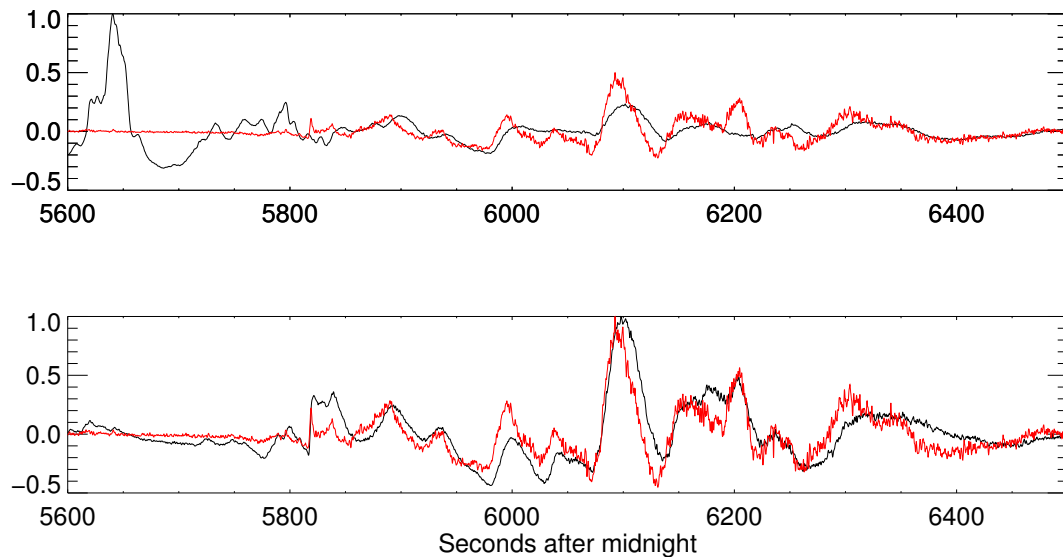
Figure 2.29: The upper panel represent the two detrended lightcurve for Nobeyama 2.0 GHz (black line) and *GBM* 50-100 keV (red line). The lower panel concerns the Nobeyama 9.4 GHz and *GBM* 50-100 keV.
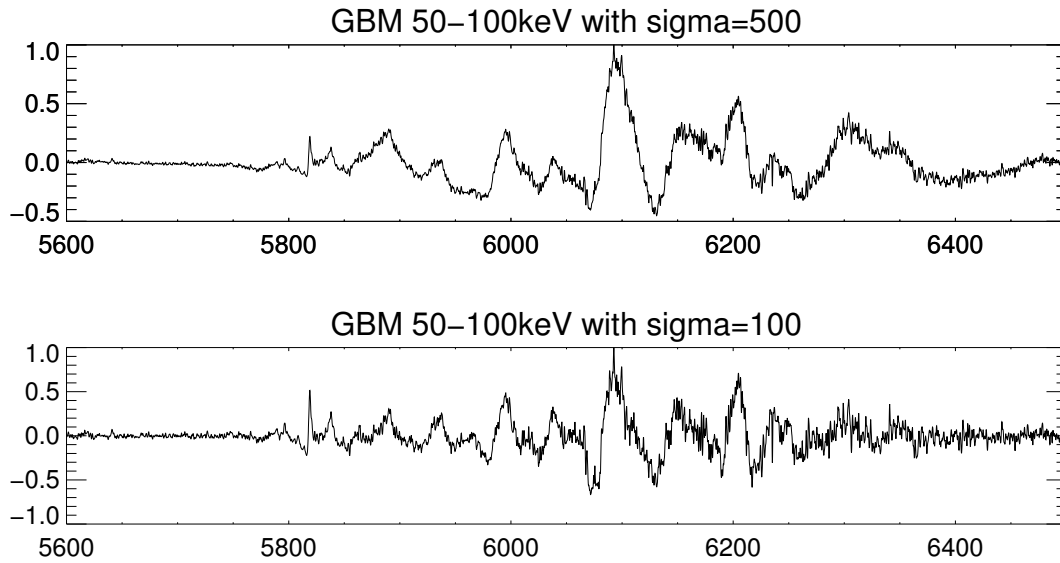
Figure 2.30: Upper panel: detrended 50-100 keV lightcurve, using a gaussian kernel having σ=500. Lower panel: detrended 50-100 keV lightcurve, using a gaussian kernel having σ=100.

sec that is present in the lightcurve, detrended with a σ=500pts (upper panel).

2.2.2   Comparison between X-ray and EUV

As discussed in sec.2.1.3, the peak of EUV emission from loops at 211 Å and 171 Å shows an emission pattern very similar to the emission pattern seen in the lightcurve of band 1600 Å and X-rays (both coming from the footpoints), but delayed. After the same delay ($\pm$10%) it shows a modulation in the lightcurve which presents a series of substructures similar to the first occurrence of the repeated pattern, suggesting that there could be a periodic process as the cause of the repetition. To test the hypothesis that the repeated pattern is causally related to the footpoint emission I computed the cross correlation between the 171 Å lightcurve and the *GBM* lightcurve in the 50-100 keV range, both of which have been properly binned on a common timescale of 24 sec.

Fig.2.31 shows the result of the cross-correlation and a detrended version of the same vector to improve the visibility of the peaks. The lower panel shows that there is a peak at 0 sec, as expected because in 171 Å we still see the impulsive emission from the footpoints, and there is a peak at 744 sec corresponding to the maximum of the emission at 171 Å , where there is the first appearance of a signal having a modulation that resembles that from the footpoints. The third peak, at 1536 sec, also behave similarly to the footpoints and the last peak, at 2471 sec is the last appearance of that quasi-periodic signal. The measuremets done by eye returned the values 758 sec, 1527 sec and 2453 sec which are compatible with the values found from the cross-correlation because the lightcurve used for the cross-correlation have been interpolated on a 24 sec timescale (instead of the 12 sec

Lightcurve 1	Lightcurve 2	σ (pts)	Delay (s)	Max coeff.	σ (pts)	Delay (s)	Max coeff.
50-100 keV	2.0 GHz	500	7.3	0.3	100	6.6	0.2
	3.75		6.0	0.75		4.4	0.6
	9.4		3.8	0.8		2.3	0.45
	17.0		2.8	0.8		2.0	0.65
9.4 GHz	2.0		2.8	0.3		3.8	0.25
	3.75		1.6	0.75		0.7	0.75
	17.0		-0.6	0.95		-0.6	0.9
50-100 keV	25-50 keV		0.2	0.75		0.0	0.7
	100-300		2.5	0.7		2.5	0.45

Table 2.4: Results of the cross-correlation between lightcurves from which the trend has been subtracted. The σ value represent the standard deviation of the gaussian kernel used to smooth the lightcurve; the smoothed lightcurve has then been subtracted to remove the trend of the emission. The Max coeff. column represent the maximum value of the correlation coefficient. The cross-correlation computed for the 2.0 GHz lightcurve has the smallest coefficient because, as shown in Fig.2.29, it has a strong emission around 5600 sec, where all the other lightcurves do not.
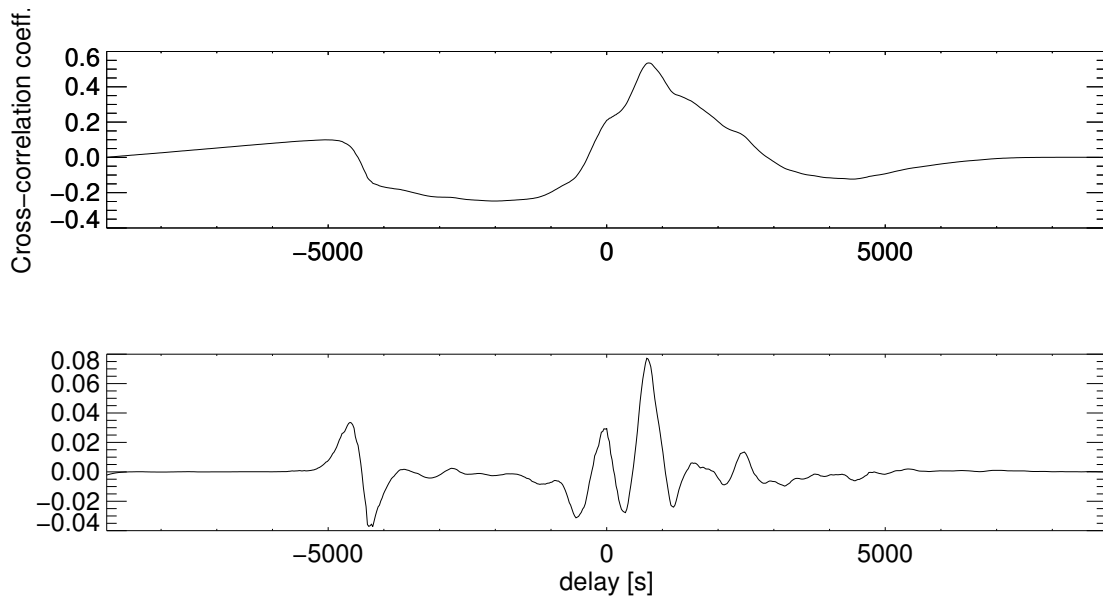
Figure 2.31: Upper panel: cross-correlation function for the lightcurves in X (50-100 keV) and 171 Å . Lower panel: Detrended cross-correlation function. The peaks correspond to the periodicities found in 2.1.3
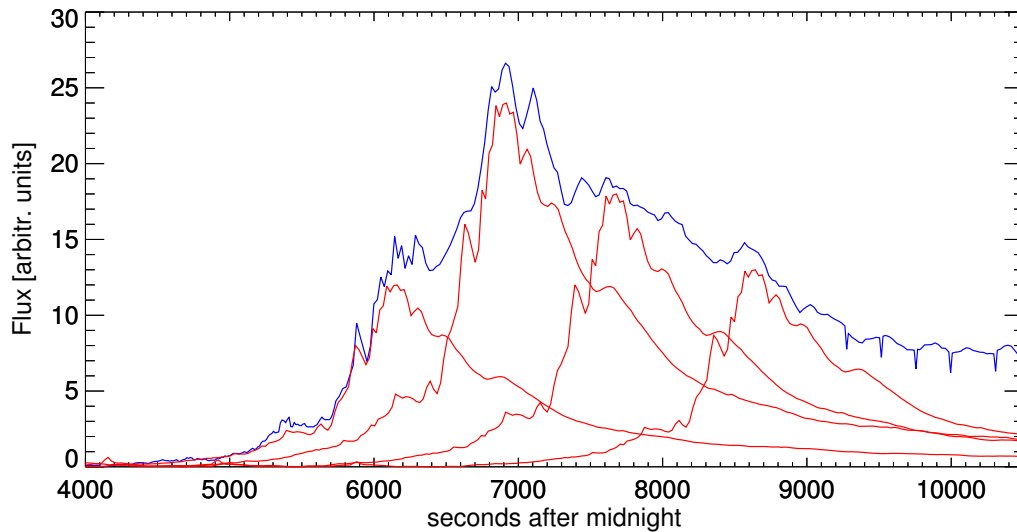
Figure 2.32: This image shows the lightcurve in band 171 Å (blue line) and the scaled lightcurve in band 1600 Å first without delay, then with a delay of 758 sec (first repetition), then 1527 sec (second repetition), and 2453 sec (fourth repetition). Each time the curve has been scaled to match the amplitude of the 171 Å lightcurve. It shows also that the substructures of the emission seem to be reproduced also in the repetition of the pattern of emission.

timescale of the original lightcurves), and the timing uncertainty is about the bin duration.

This behavior make a question arise: why the looptops emits this way? What causes this quasi-periodicity? Is this quasi-periodicity present also in flares? In the following sections we will outline a scenario based on these observations.

2.3 Flare 14/05/2013 analisys

2.3.1 *NoRP* Data

The *NoRP* data for this event are shown in Fig.2.34 and Fig.2.33. The latter figure shows all the channels together without scaling in order to highlight the differences in amplitude between the channels. A series of letters mark the peaks that have been analyzed, which are the peaks having a recognizable structure in almost all the frequencies. Some features, however, are strong at some frequencies but absent in others so it is difficult to analyze their behavior.

As we have seen for the May 15 flare the periodicity of the peaks range from few seconds to few hundred seconds. The radio lightcurve divides into four intervals:

- the main part where we find the peaks marked with A, B, C, and D[4] (Fig.2.36);

---

[4]I have not analyzed the intermediate peak between C ad D because it was not clearly visible in all the lightcurves.
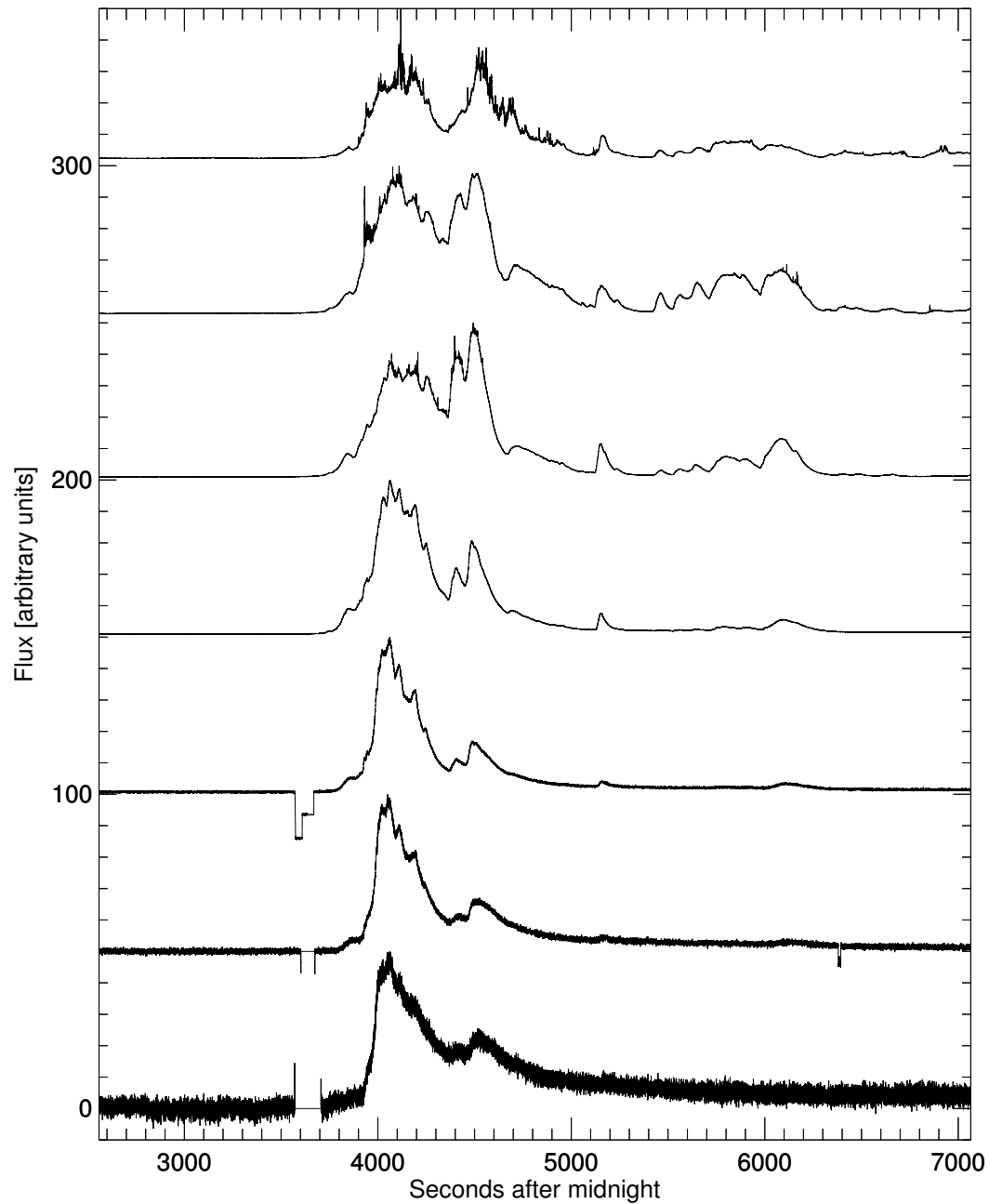
Figure 2.33: The whole dataset from Nobeyama Radio Polarimeter. The frequency of each channel is (from top to bottom, in GHz): 1, 2, 3.75, 9.4, 17, 35, 80. From this image we can appreciate how each feature evolves at different energy. The gap around 3700 sec at 17 GHz is due to the calibration of the receiver gain . In 35 and 80 GHz the calibration steps have been cut away.
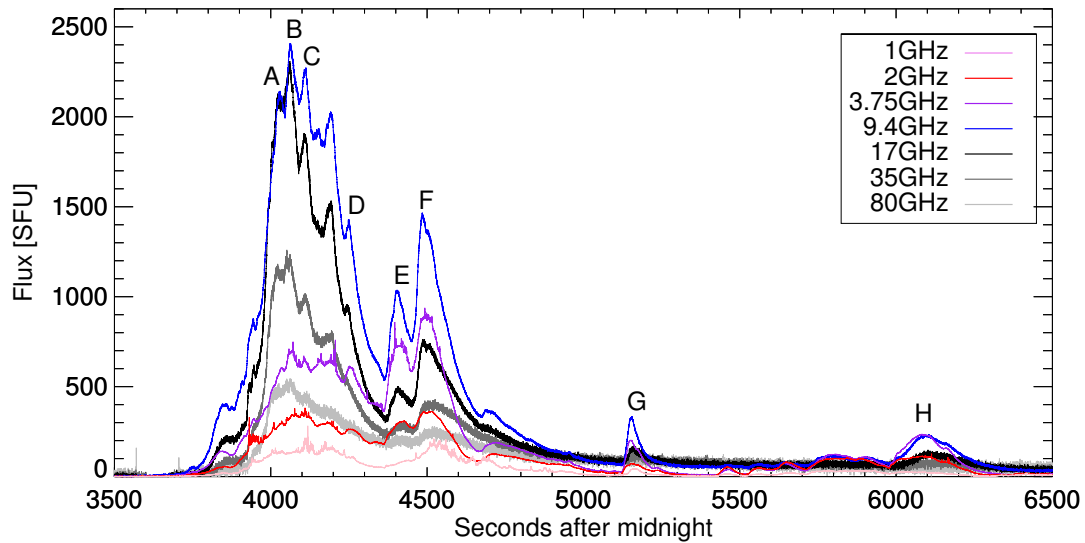
Figure 2.34: Same lightcurves as Fig.2.33, but not scaled, in order to appreciate the relative amplitude between channels.

- two features marked with E and F (Fig.2.37);

- a weak but well defined peak marked with G (Fig.2.38);

- the last, broad peak marked with H (Fig.2.39).

The pre-flare stage is comparatively quiet, with no sign of activity. The "step-like" feature around 3600 sec at 17 GHz is due to the calibration of the instrument (see Sec.4.1). There is a small "bump" at the beginning, around 3900 sec (see Fig.2.35), and it is worth noting that although the peak is not well defined (so, has not been analyzed), the whole feature seems to be more delayed as the energy goes up.

Fig.2.36 displays the main part of the emission in all frequencies except 1 GHz. The low energy lightcurves are more "spiky" and irregular with respect to those at high energy. The peaks shown are A ($\sim$4030 sec), B ($\sim$4060 sec), C ($\sim$4110 sec), and D ($\sim$4250 sec). The timing analysis is in Tab.2.5, which shows that each peak has very similar behavior to the May 15 flare: in general, low energy emission lags that at high energy with some exception. Specifically:

- peak A: the emission at 35 GHz leads the emission at other frequencies;

- peak B: is like peak A, but now 17 GHz peak first, while 35 GHz and 80 GHz are both delayed;

- peak C does not show a regular behavior;

- peak D does not show a "turn off" frequency and the highest frequency peak first (note that this peak is not recognizable at 80 GHz).
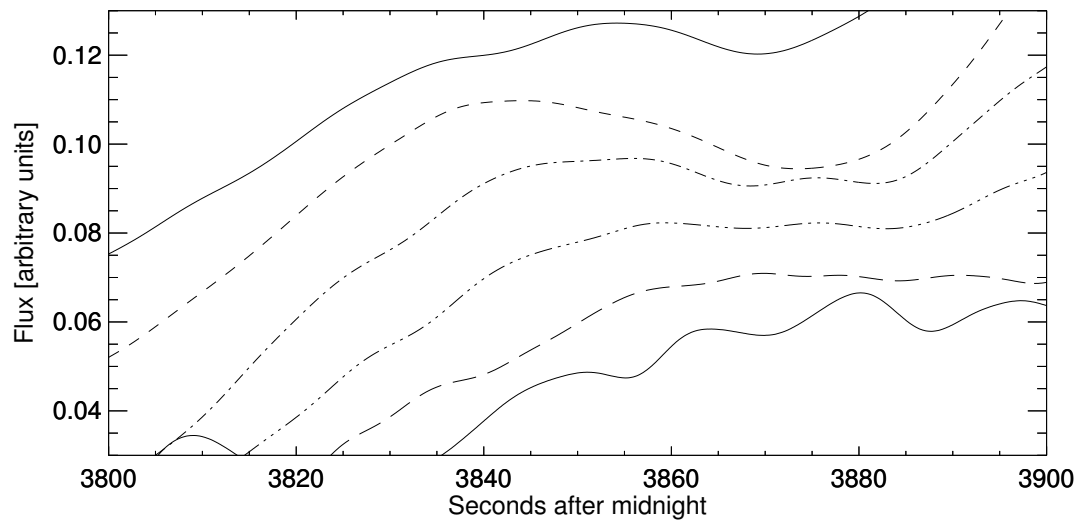
Figure 2.35: Behavior at different energies of the bump around 3850 sec. From top to bottom, the frequencies are: 2, 3.75, 9.4, 17, 35, 80 GHz. The overall behavior seems to be the opposite of what we usually find: instead of negative delay as the frequency goes up, in this case we see there is a positive delay.
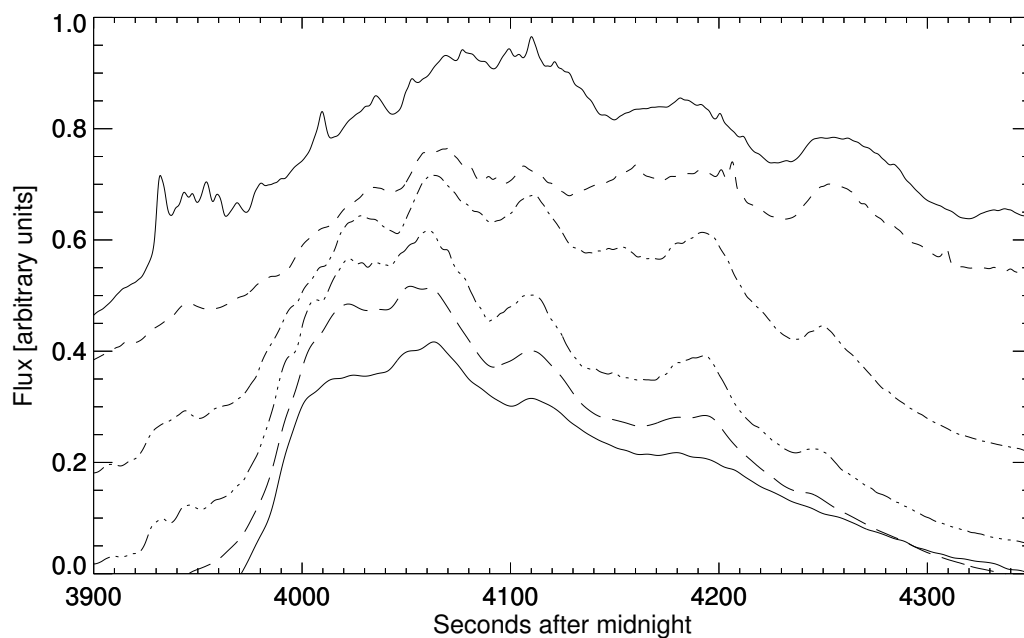
Figure 2.36: Radio emission of the main part of the flare. The frequencies are, from top to bottom: 2, 3.75, 9.4, 17, 35, 80 GHz. All the lightcurve are smoothed with a gaussian having σ=10pts with the exception of 35 and 80 GHz which are smoothed with a gaussian having σ=30pts. The plotted interval covers a time window where the peaks from A to D are.
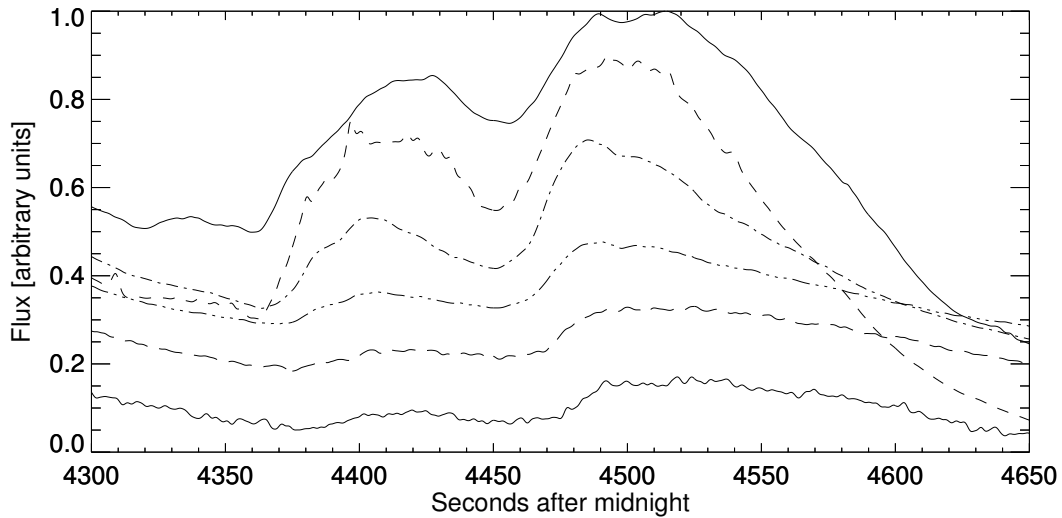
Figure 2.37: Radio emission from the two peaks marked with E and F. The frequencies are, from top to bottom: 2, 3.75, 9.4, 17, 35, 80 GHz. All the lightcurve are smoothed with a gaussian having σ=10pts with the exception of 35 and 80 GHz which are smoothed with a gaussian having σ=30pts.

Fig.2.37, 2.38 and 2.39 show peaks E ($\sim$4400 sec), F ($\sim$4500 sec), G ($\sim$5150 sec) and H ($\sim$6100 sec). The timing analysis shows that:

- peak E: the first frequency to peak is 9.4 GHz. For 3.75 GHz, there is a significant difference between the delay calculated with a 10pts smoothing and that with 30pts smooting due to the presence of substructures which are removed with the wider gaussian;

- peak F: as for peak E, 9.4 GHz peaks first. The difference in timing at 80 GHz is probably due to the noise;

- peak G: 3.75 peaks first and higher frequencies are delayed;

- peak H: 2 GHz leads, and all the others frequencies are delayed.

Each peak has a different leading frequency (see Tab.2.5) which we will denote as ν_{fp}. Moreover bands that are both higher and lower than ν_{fp} are increasingly delayed. The leading frequency is not always the same: for peak A, it is 35 GHz and it decreases to 2 GHz at peak H.
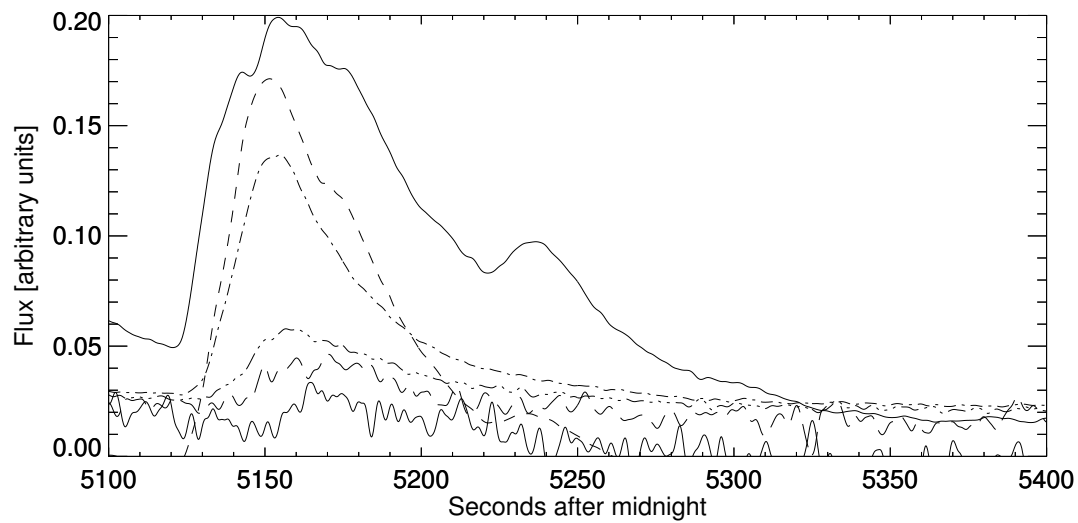
Figure 2.38: Radio emission from the peak marked with G. The frequencies are, from top to bottom: 2, 3.75, 9.4, 17, 35, 80 GHz. All the lightcurve are smoothed with a gaussian having σ=10pts with the exception of 35 and 80 GHz which are smoothed with a gaussian having σ=30pts.
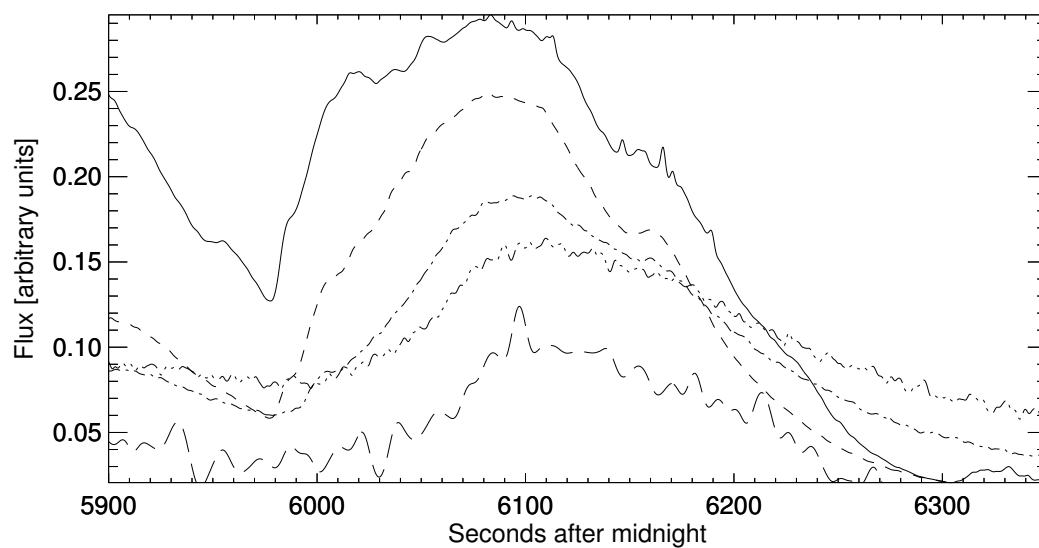
Figure 2.39: Radio emission from the peak marked with H. The frequencies are, from top to bottom: 2, 3.75, 9.4, 17, 35 GHz. All the lightcurve are smoothed with a gaussian having σ=10pts with the exception of 35 GHz which is smoothed with a gaussian having σ=30pts.

| Peak	Freq (GHz)	σ=10pts	σ=30pts	Peak	Freq (GHz)	σ=10pts	σ=30pts
A	2.0	-	-	**E**	2.0	4427	4426
	3.75	4034	4035		3.75	4397	4410
	9.4	4029	4029		9.4	4404	4404
	17.0	4022	4023		17.0	4406	4406
	35.0	4022	4022		35.0	4419	4417
	80.0	4023	4025		80.0	4423	4422
B	2.0	4078	4078	**F**	2.0	4514	4513
	3.75	4068	4068		3.75	4493	4493
	9.4	4063	4063		9.4	4485	4485
	17.0	4060	4060		17.0	4490	4489
	35.0	4061	4061		35.0	4512	4512
	80.0	4063	4063		80.0	4528	4522
C	2.0	4110	4110	**G**	2.0	5154	5155
	3.75	4106	4107		3.75	5151	5151
	9.4	4111	4110		9.4	5154	5153
	17.0	4110	4109		17.0	5158	5158
	35.0	4112	4110		35.0	5170	5171
	80.0	4111	4109		80.0	5164	5166
D	2.0	4254	4253	**H**	2.0	6083	6081
	3.75	4252	4253		3.75	6082	6082
	9.4	4249	4249		9.4	6101	6101
	17.0	4245	4245		17.0	6110	6110
	35.0	4243	4242		35.0	6121	6121
	80.0	-	-		80.0	-	-

Table 2.5: Energy dependent peak time (sec) of the peaks in Fig.2.34. The plot of these data is in Fig.2.40. For frequencies between 2.0 GHz and 35 GHz is $\pm$1 sec, while for 80 GHz is $\pm$3 sec.
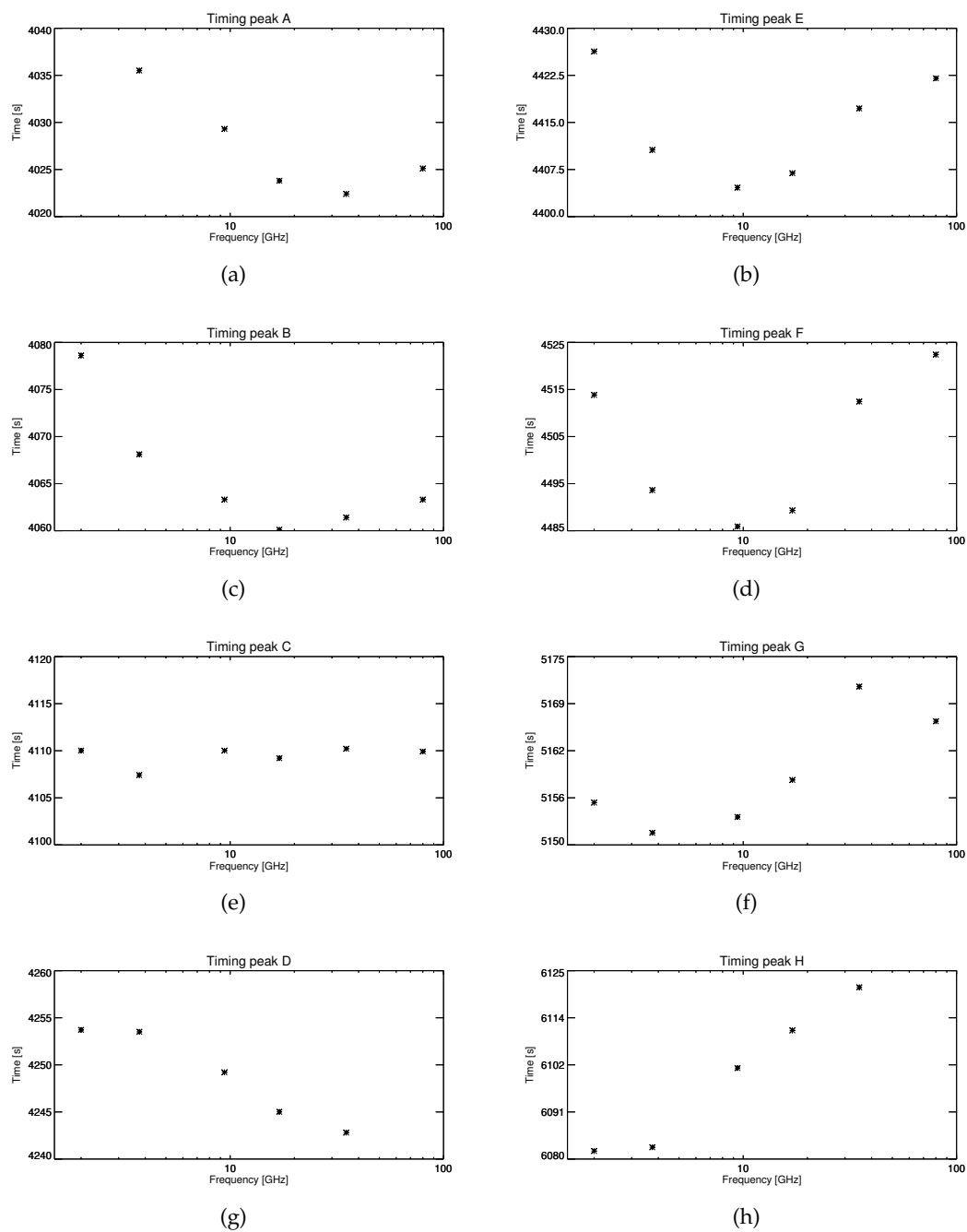
Figure 2.40: Plot of the computed peaktime for each peak. The computed peaktime is shown in Tab.2.5

Peak	Channel	σ=10pts	σ=30pts	Peak	Channel	σ=10pts	σ=30pts
A	3	4017 $\pm$ 1	4018.0 $\pm$ 1	**E**	3	-	-
	4	4017	4018		4	4396	4398
B	3	4061	-	**F**	3	4472	4472
	4	4060	4062		4	4479	4479
C	3	-	-	**G**	3	5151	5151
	4	-	-		4	5152	5152
D	3	4242	4241	**H**	3	6048	6050
	4	4244	4244		4	6072	6073

Table 2.6: Energy dependent peak time of the peaks in Fig.2.41. The effects of saturation, thermal emission from looptop and shot noise at high energies reduce the possibility of peaks detection. Channel 6 and 7 are not taken into account for the time analysis but it has to be mentioned that channel 6 shows a strange behavior (compared to the other lightcurves), in fact it has a peak at 4105.9 sec and one at 4397.8 sec.

2.3.2 *Fermi/GBM* Data

Fig.2.41 shows the dataset from *Fermi/GBM* . The effect of saturation is present from 4 keV to 50 keV, while the effect of thermal emission of the looptop seems still to be present in channel 4 (100 keV - 300 keV). Unfortunately, no *RHESSI* data are available for this event, so we cannot identify with certainty the source region of emission. The first channel that seems to show pure footpoint emission is channel 5 (from 300 keV to 540 keV). Noise is important here because the SNR is low for channels from 5 to 7 and it is very difficult to distinguish any feature other than the two main peaks. For these reasons the analysis cannot be as complete as for the radio.

In Tab.2.6 there is the timing analysis for the peaks in the x-ray lightcurves. As found in the May 15 flare, all structures present in radio are also present in the X-ray lightcurve, so the same population of particles are likely responsible for both radio and X-ray emission. In general, high energy emission come later than low energy ones.
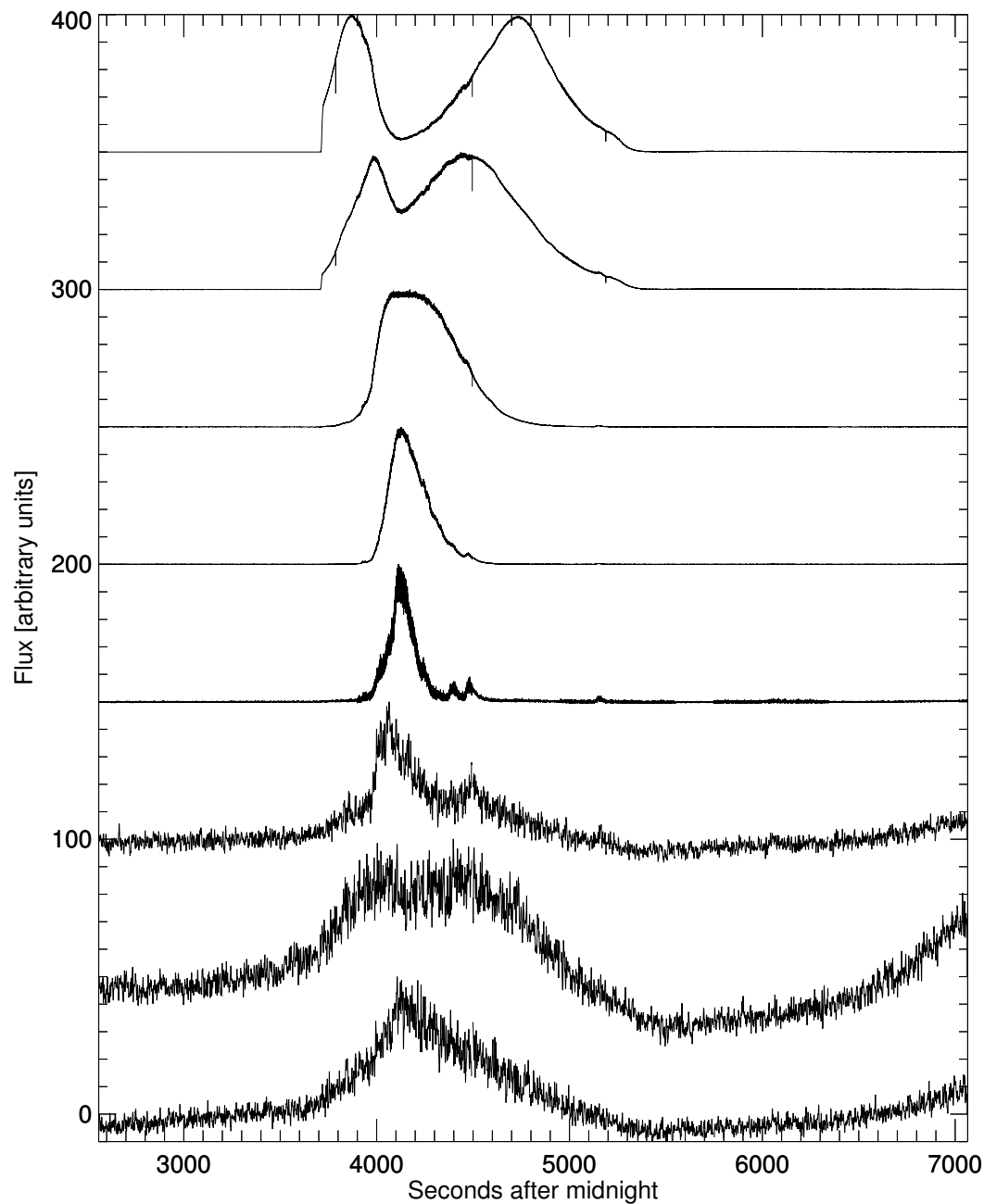
Figure 2.41: The whole dataset from *Fermi/GBM* . From top to bottom, the energy goes from a minimum of 4 keV to a maximum of 2MeV. There is saturation effect till 50 keV (third lightcurve from top) and there is thermal emission from the looptop till 100 keV (fifth lightcurve). Pure footpoint emission is present from 100 keV on. Channel 5, 6, and 7 show also the effect of the modulation due to the orbit which seems to be stronger in channel 6. This effect is due to the fact that the counts are so low that the background emission from Earth is the dominant signal observed, and it changes with respect to the position of the satellite and its orientation.
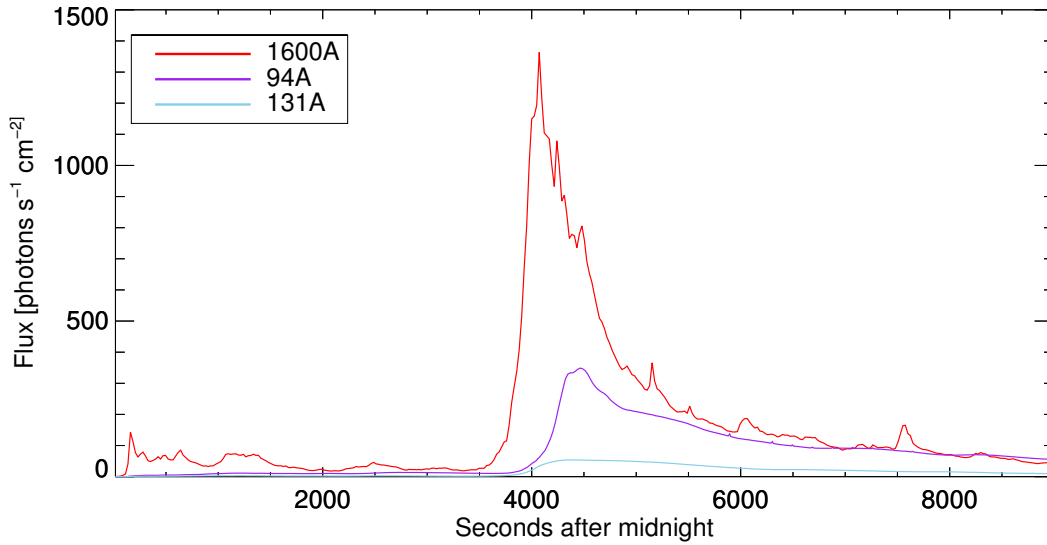
Figure 2.42: Data from *SDO/AIA* instrument. The lightcurves have been taken by integrating on the whole active region, keeping the loops related to the flare in the box of integration. The box is defined by the lower left and upper right vertices which are [-948,152] and [-879,249] arcseconds, in heliocentric coordinates.

2.3.3   SDO */AIA* Data

Fig.2.42 and 2.43 show the lightcurves from the active region in all EUV bands, taken integrating a box defined by the lower left corner at [-948,152] arcseconds and the upper right corner at [-879,249] arcseconds. The overall behavior is pretty much like the previous flare. The most of the emission coming from the footpoints (band 1600 Å), and the looptops showing the same repetition pattern. Every band shows the effect of the saturation, but it does not prevent identifying temporal structures, with the exception of band 193 Å that is heavily by saturated[5].

The loops of the arcade seem to have different lengths: the shortest has a length of ∼38000 km and the longest ∼46000 km and the measurement has been done using the model of circular loop used in literature.

We find a timescale for the slow magnetoacoustic oscillation of $\tau_{slow} = 420 sec$ with an uncertainty of 10% using the formula 3.1 and the computed length of the loops. This is quite compatible with the timescale of the observed repetition pattern. The computed timescale are ∼480 sec for band 171 Å and 211 Å and ∼422 sec for band 335 Å.

---

[5]Nonetheless the images in band 193 Å , being so sensitive, are very useful to understand the location of the beginning of the heating process, before the saturation covers the entire region
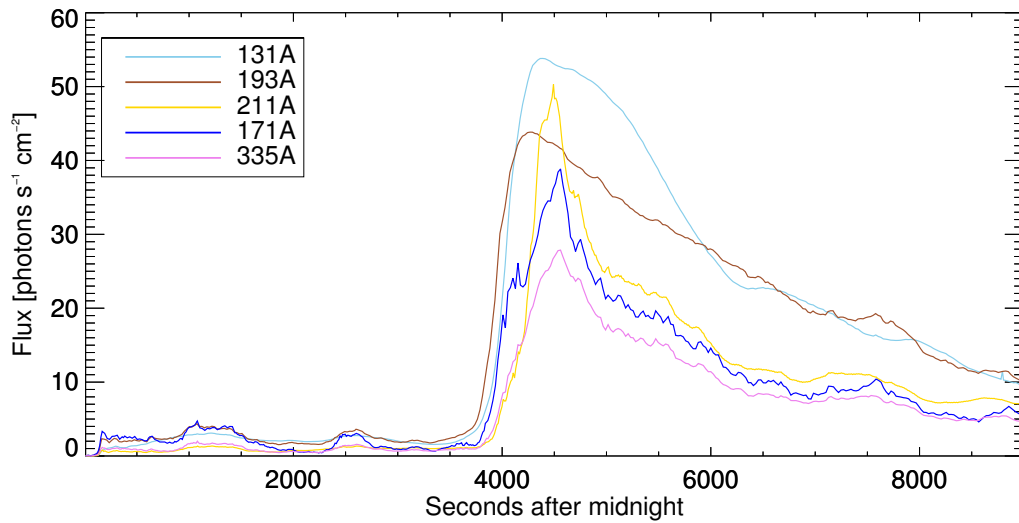
Figure 2.43: Data from *SDO/AIA* instrument. See caption of Fig.2.20 for the explanation about the integration. The bands plotted here show the emission from both footpoints (in the rising part of the emission,from 3900 sec to 4500 sec) and loops. The lightcurve of the band 131 Å has been also plotted here for ease of comparison between the two figures.

2.3.4   Loop motion

This flare shows an interesting feature: the active region in which this flare occurred was very complex, many loops are braided, and there are loops connecting this region to other distant regions on the surface (see Fig.2.44, panel A). Here we see the image in band 171 Å at the peak time. We see hot loops and emission coming from their footpoints. In order to visualize the motion of the loops I cut a line of pixel from each frame, as shown in the figure, putting this line in a (m, n) matrix, where m is the number of frames of the observation and n is the length in pixel of the line cut to create the time-space image shown in panel (c) of Fig.2.44. This means that if a loop changes its position along the cut line, we will see a motion in the direction of the ordinate. What we see in panel (c) is that there is a group of loops that starts at an ordinate of about 220pix and starts to slowly move away from the surface. Then, at around 3900 sec, the impulsive phase of the flare take place and the loops start to strongly oscillate. The oscillation begins to damp untill (light green arrow) the loops loose support and start to implode (i.e. move toward the surface). Then, 185 sec later, the two footpoints light up **at the same time** (panel *b* which is a frame of the observation in band 1600 Å and the two footpoints are indicated by the two light green arrows). This is also seen in panel *c* in the blue lightcurve from the box containing the active region in band 1600 Å : the peak marked by the dark green arrow indicates the time at which the frame in panel *b* wast taken.

We expect that the coronal gas is supported by magnetic tension (β should be extremely small) and also that, in general, the magnetic field is frozen in the plasma, so motion of

(a)

(b)

(c)
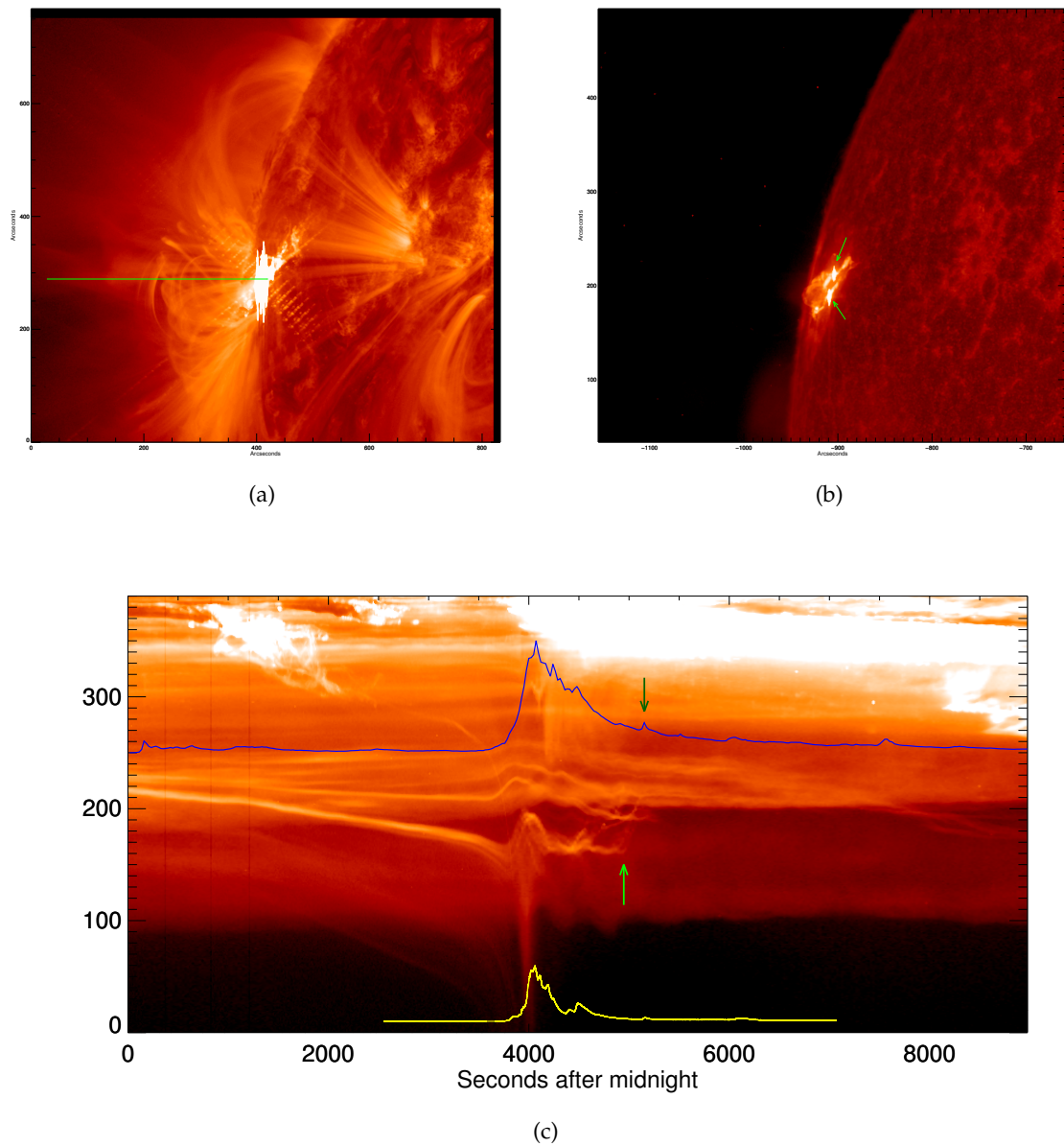
Figure 2.44: This image shows the motion of the loops during the whole event. Panel A shows the 171 Å frame at peak time. Panel B shows the 1600 Å frame at ∼5500 sec, when the falling material turns on two footpoints of a loop. Panel C shows a time-space plot, produced by cutting a line of pixel at each frame of the 171 Å observation (as shown by the green line in panel A) to follow the motion of the loops; the blue line represent the lightcurve in band 1600 Å integrated over the whole active region; the yellow line represent the emission in radio at 17 GHz. As we can see in panel C, there is a group of loops (starting from an ordinate of about 220) which rises (in this image they seems to go down but the surface is in the upper part of the plot) till the time when the impulsive part of the flare take place. Then, an oscillation is triggered and after few oscillations the group implodes (the start of the implosion is indicated by the green line). After about 200 sec there is a small peak in the 1600 Å lightcurve which corresponds to the image shown in panel B, where the arrows point to the two footpoints of a loop which is not visible.

the magnetic field and plasma are strongly coupled. We see two footpoints lightning up at the same time so it appears that the loops in the higher corona have lost support and then started moving towards the surface, where the plasma links to a loop, before hitting the surface and causing the simultaneous brightening of its two footpoints.

I can also estimate the Alfvén speed. The estimate is done knowing that the time of flight of the material, which is 185 sec, and the distance traveled, whose projection is 210pix. We also know the angle that the line normal to the active region makes with the line of sight which is of the order of 14deg: the deprojected distance is 216pix. So the average velocity is 1.14pix/s and since each pixel equal to ∼450 km, we computer an Alfven speed of 510±50 Km/s. This estimate is useful also because we can rule out the "Alfvenic" origin of the pattern repetition seen in 2.3.3. Since the longest loop is 46000 km, a magnetic perturbation should have a periodicity of about 90 sec. Instead, we see a repetition with a timescale five times longer, which is compatible with the acoustic travel time. The magnetoacoustic origin appears more probable.

2.4 Comparison between datasets

Fig.2.45 shows the comparison between radio, EUV and hard X-ray emission. Channel 5 from *GBM* is the lowest channel shows only footpoint emission; the lower energy channels still show the effect of the thermal emission from the looptop. Since the emission in the energy range coveredby channel 5 is so low, the SNR is also low. The lightcurve shown in the figure (black line) has been smoothed with a gaussian having σ=20pts.

The lightcurves show that almost every feature has its correspondent in every lightcurve and this is evidence that the same population of particles is responsible for the emission in each band. Peaks E and H are not visible in hard X-ray emission but the fact that they are present in *SDO* lightcurve suggests that these peaks may be just too faint to be visible, given the SNR. The single event shown in 2.3.4 (i.e. peak G, around 5250 sec) is also present in all the three spectral ranges.

The comparison between the timing analysis of each peak (Tab.2.5 and Tab.2.6) yelds:

- hard X-ray emission arrives always first, except for peaks B and C, and shows that low energy comes first;

- Radio emission shows the effect explained in Sec.2.3.1: the peaktime for each structure at each frequency is not constant. In general, one frequency leads the others and the other frequencies follow a sort of delay curve. Additionally, the leading frequency is not always the same but shifts from high frequencies at the beginning of the flare emission to low frequencies at the end of the flare event;

- UV emission from the footpoints is highly correlated both with hard X-ray and radio emission.
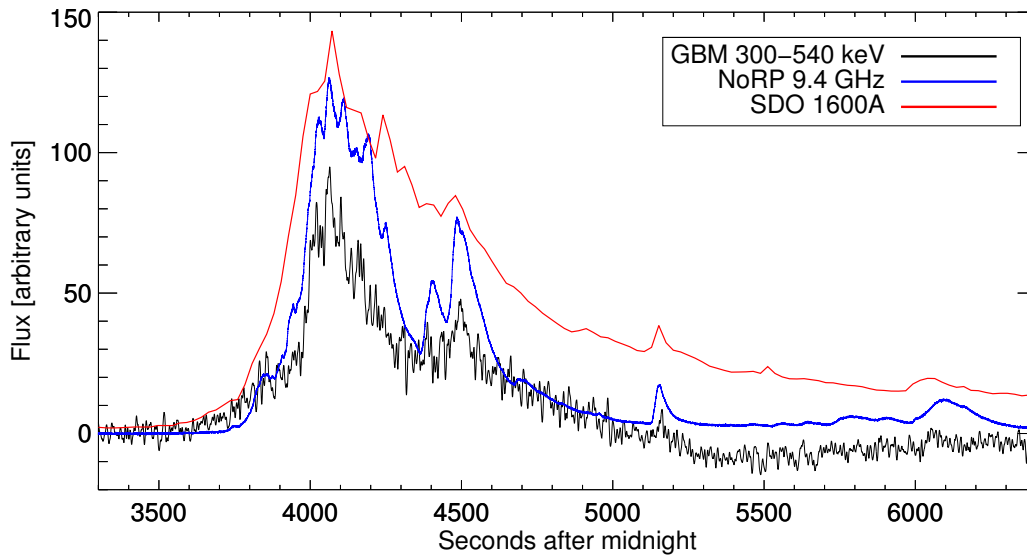
Figure 2.45: Comparison between lightcurves. Top (red) the 1600 Å lightcurve, middle (blue) the NoRP 9.4 GHz lightcurve, and bottom (black) the *GBM* 300 - 540 keV. Note that even though the *GBM* lightcurve was smoothed at σ=30 pts, it is still very noisy hence is not possible to rely on the peak time computation.

2.5 Flare 13/05/2013 analisys

2.5.1 *NoRP* Data

The full dataset from *NoRP* is shown in Fig.2.47 and 2.48.

The data show some preflare activity, followed by the main emission event which seems to be subdivided in two (maybe three) subevents. Also here, the periodicities found on the lightcurve have a wide range of timescales so it is not possible to say whether one dominantes. As previously noted, the SNR is lower at high frequencies where the majority of the peaks are not visible.

Even at low frequencies it is difficult to identify any well defined structure. For this reason, has not been possible to perform the same analysis as for the May 14 flare. In particular we cannot check whether the "single peak delay curve" is also displayed by this flare.

The only way we can check whether there is a delay is cross-correlation of the lightcurves at all frequencies with that from X-rays (shown in Fig.2.49). The result of this analysis is shown in Fig.2.46 and Tab.2.7.

As we can see, we still observe a minimum delay at 17 GHz, and the others are delayed with respect to it.

It is worth noting that the x-ray lightcurve has been smoothed with a gaussian with σ=30, while the radio lighturves have been smoothed first with a gaussian with $\sigma = 0$ (i.e.

Hessi ch.	*NoRP* ch.	$\sigma : 30, 30$ [s]	$\sigma : 30, 10$ [s]	$\sigma : 30, 0$ [s]	Avg del. [s]
4	0	18.9	18.9	18.9	18.9±0.1
	1	15.5	15.4	15.3	15.4±0.1
	2	19.2	19.2	19.0	19.1±0.1
	3	15.9	15.9	16.0	15.9±0.1
	4	12.0	11.8	11.8	11.9±0.1
	5	29.9	29.4	29.3	29.5±0.3
	6	49.2	49.0	49.3	49.2±0.3
5	0	-	-	-	-
	1	8.9	8.7	8.8	8.8±0.1
	2	8.8	8.2	8.4	8.5±0.3
	3	7.5	7.3	7.1	7.3±0.2
	4	5.5	5.5	5.3	5.4±0.1
	5	15.3	14.7	14.8	14.9±0.4
	6	35.7	36.4	37.0	36.4±0.7

Table 2.7: Energy dependent peak time of the two peaks in Fig.2.13

no smoothing), then with $\sigma = 10$ then with $\sigma = 30$, showing a discrepancy of the order of 0.2 sec (just two points) so it is very stable.

2.5.2   *RHESSI* Data

The *Fermi* satellite was able to record only the first few seconds of emission before the Earth entered the FOV of the sunward detectors, so I used the *RHESSI* satellite for both the lightcurves and imaging.

As shown in Fig.2.49, only the 4th and the 5th channels, which correspond to an energy range of 50-100 keV and 100-300 keV, were usable. Both channels show very sharp variation and highly correlated, with the higher channel having a delay of 1.2 sec with respect to the lower one. The pattern of emission is similar to the radio lightcurve.

The most interesting part of the RHESSI data is the "imaging", since this is a limb flare, and maybe one of the footpoints (or both) is behind the limb.

Fig.2.50 shows that the x-ray photons with energy from 3 to 50 keV come predominantly from the looptop. The location site of the emission is actually **slightly above** the emitting loops (the background image is from *SDO* and shows the emission at 335Å, tracing material with a temperature around $2.5 \cdot 10^6$K). At energies between 50 and 300 keV we see that the source displaces toward the upper footpoints with a very weak residual emission still coming from the looptop. The fact that the upper footpoint seems to be more involved

in the emission than the lower footpoint may have two explanations. The first is that the same thing as the flare from May 15 is occurring, where both footpoints are visible and we actually see more energy is coming from the upper footpoint. The second possibility is that the lower footpoint is actually hidden behind the limb and we don't see its emission.

Fig.2.51 shows the emission at 335 Å from the loops and the contour plot of the *RHESSI* data. Contour plots are shown for *RHESSI* channel 1 (red), 3 (green) and 4 (blue) and the contour levels are 90%, 80% and 70%.
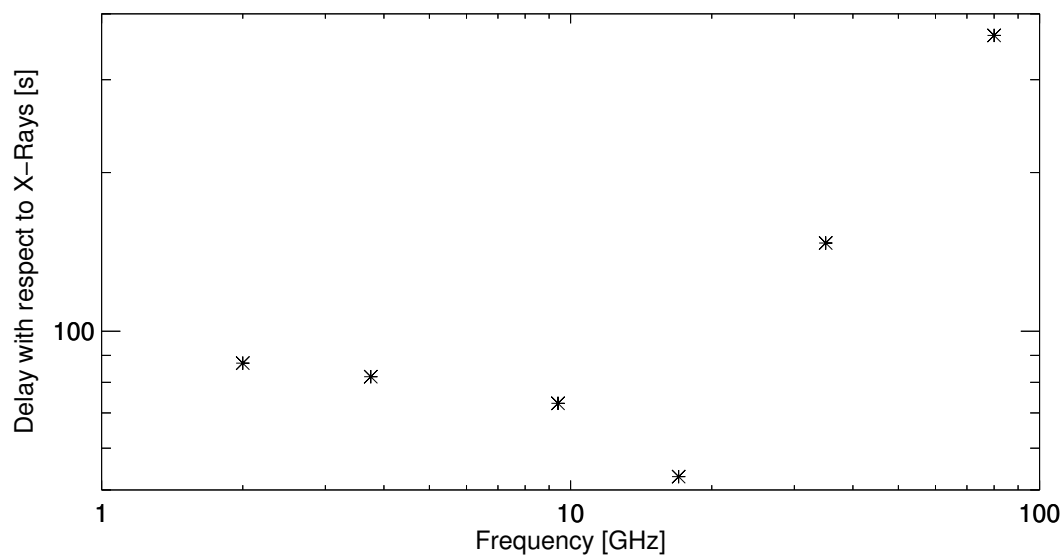
Figure 2.46: Delay curve of radio emission with respect to x-ray emission. The delay has been computed by usint the cross-correlation. The shape is a little bit different from the single-peak analisys performed on the previous flares, but still we find a frequency at which the delay is minimum while the others are delayed with respect to it.
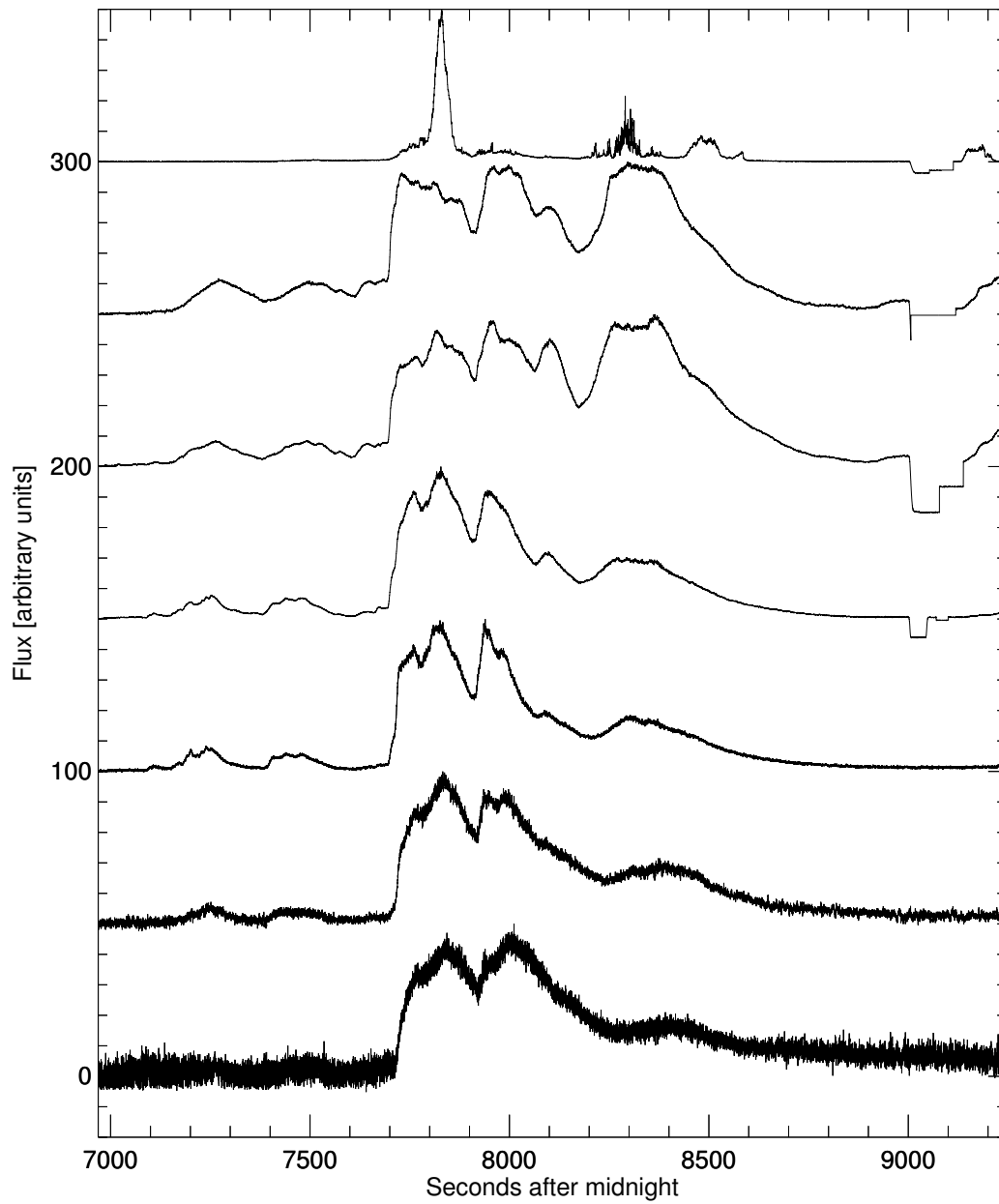
Figure 2.47: The whole NoRP dataset. From top to bottom the frequency goes from 1 GHz to 80 GHz. The step-like feature in the ending phase of the lower frequencies is due to the calibration of the instrument.
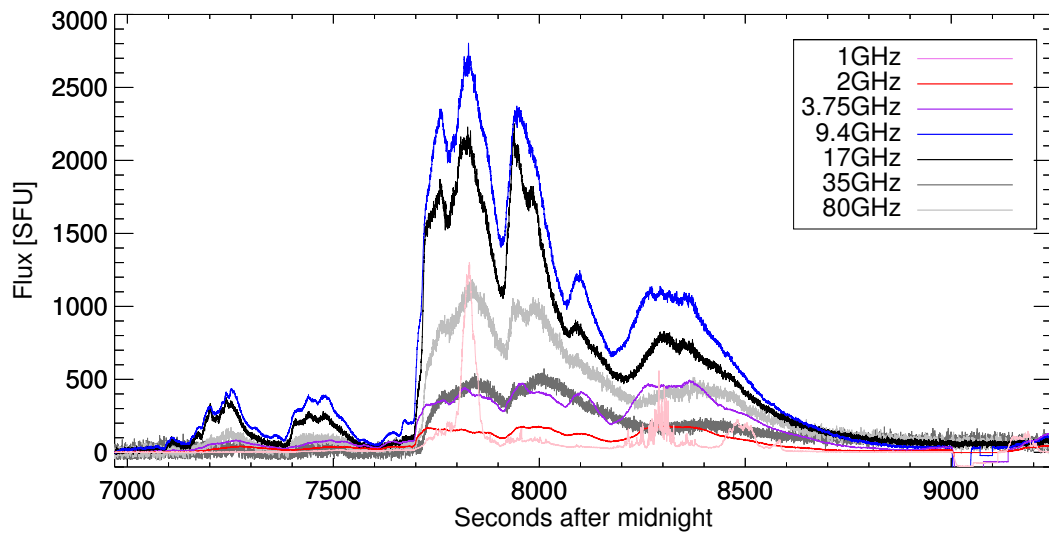
Figure 2.48: The whole unscaled NoRP dataset.
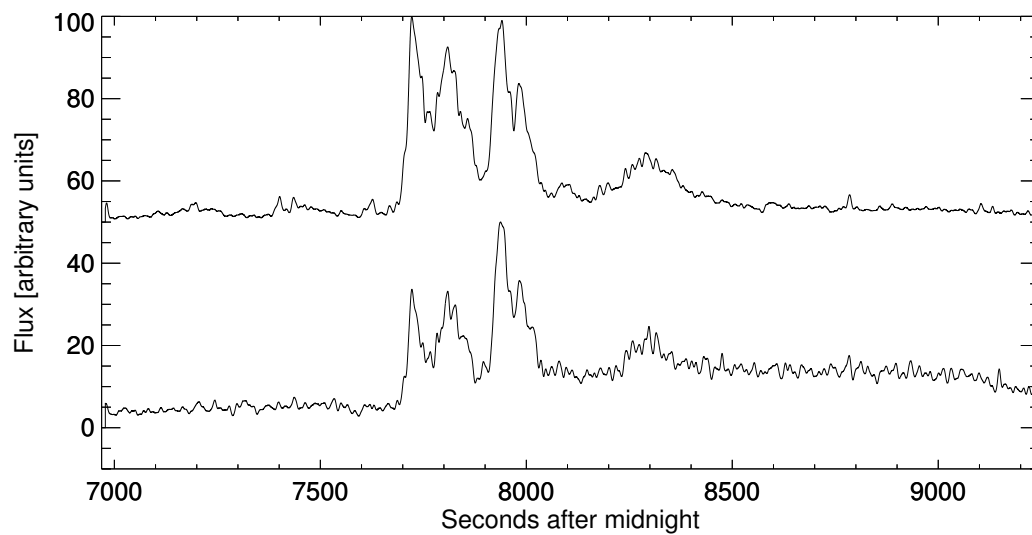
Figure 2.49: Lightcurves from RHESSI. The upper lightcurve shows the 50-100 keV emission and the lower one the 100-300 keV emission.
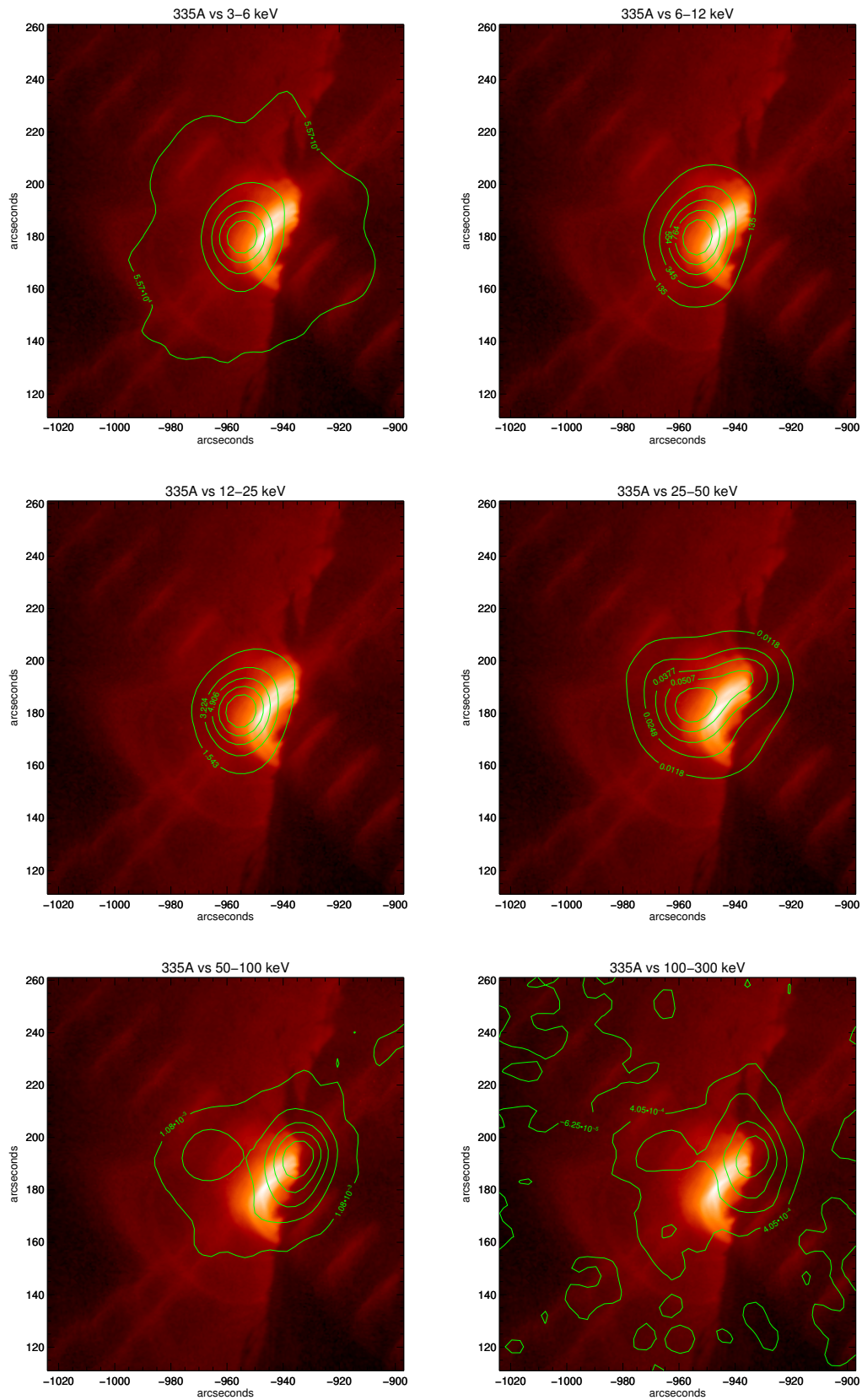
Figure 2.50: HESSI data (green contour in units of photons cm^{-2} s^{-1} arcsec^{-2}) vs *SDO* 335 Å. As seen before, at low energies the emission is predominantly coming from the looptop and it's mostly thermal. As the energy goes up the source seems to shift towards the upper footpoint of the ensemble of loops.
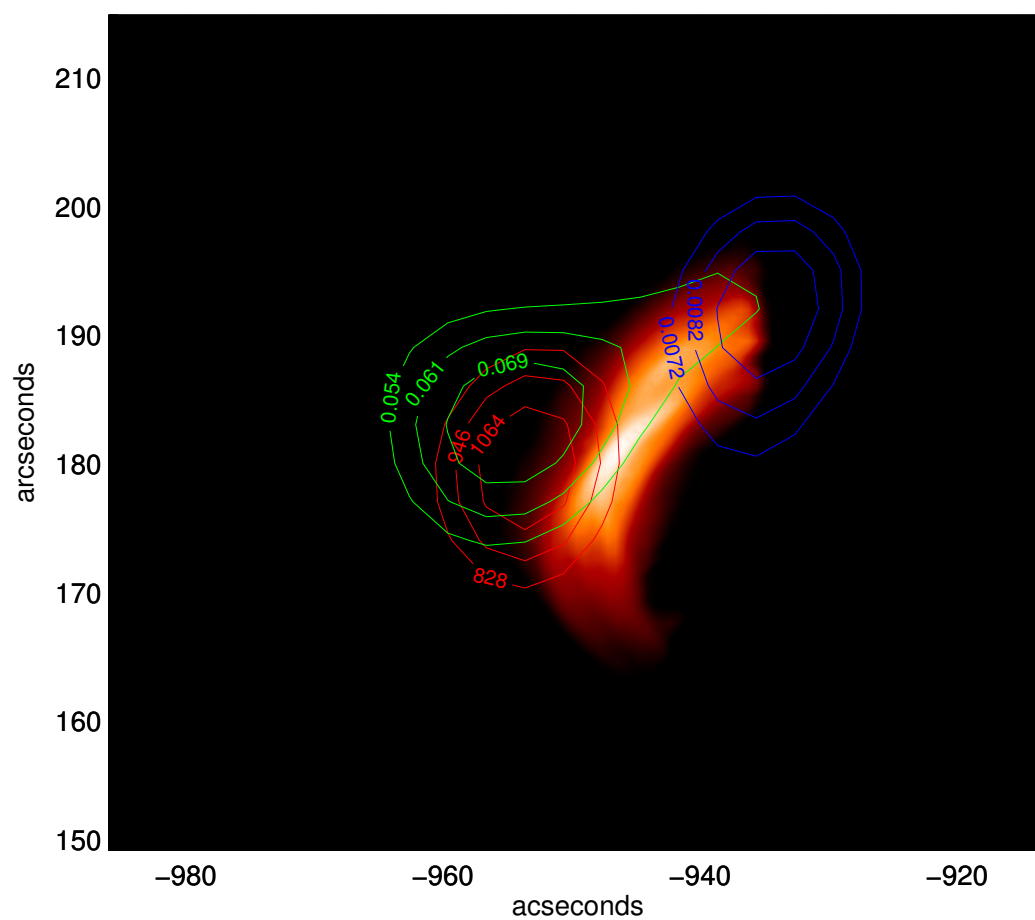
Figure 2.51: The background image is the emission from loops at 335 Å . The contour plots of the *RHESSI* data represent channel 1 (red contour, 6-12 keV), channel 3 (green contour, 25-50 keV) and channel 4 (blue contour, 50-100 keV). The contour levels are 90%, 80% and 70%.

2.5.3   SDO /*AIA* Data

Since this flare was on the limb, the arcade footpoints may be behind the limb, and the emission may be heavily absorbed by the material along the line of sight.
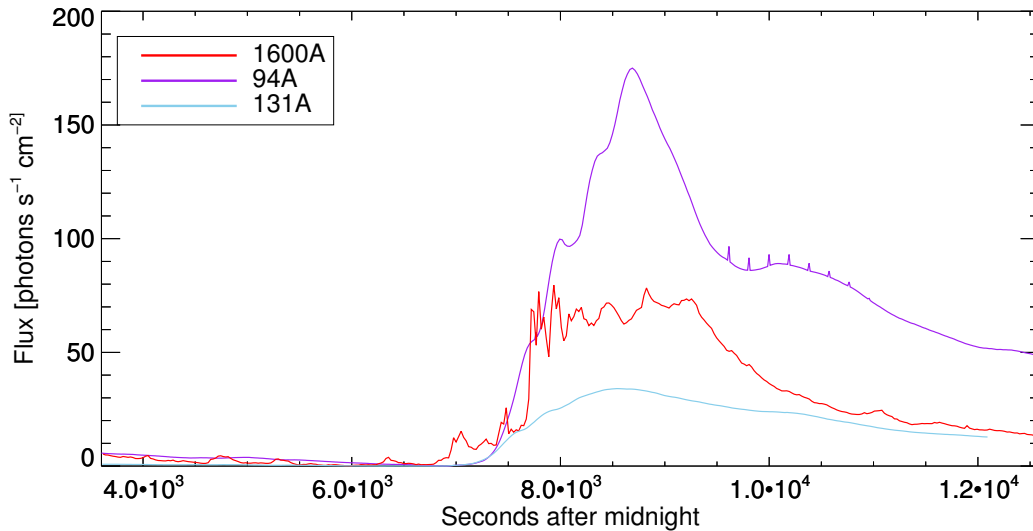
Figure 2.52: UV and EUV lightcurves for the May 13 flare. The 94 Å lightcurve is the one that shows a "bumpy" rising, with timing consistent with a magnetoacoustic oscillations given the computed length of the loops.

This explains the observaton that the part of the 1600 Å emission coincident with the x-ray emission is not much stronger than that coming from the loops (1600 Å band) in the same band but it is almost at the same level (Fig.2.52). For comparison, Fig.2.20 shows that at the peak of 1600 Å emission ($\sim$6000 sec), the flux is more than twice the peak at $\sim$7000 sec (which is the result of the emission from the loops).

Looking at the emission at 171 Å (or also at 211 Å), there is no strong evidence of an emission pattern repetition. But when we look at the 94 Å emission in Fig.2.52 we see that there are some periodic bumps in the rise of the emission, the first two being almost coincident with the peaks at 1600 Å coming from the footpoints, with the next two being delayed by 691 sec. This is comparable to the delay seen in the May 15 flare, where an arcade of similar size emerges. Finally, comparing band 94 Å with band 171 Å and 211 Å in the previous flares we find good match between the overall behavior of the emission. Thus we can say that in general, the oscillation seen in band 94 Å may traces the oscillation of the loops.

2.6   Comparison between datasets

The comparison between dataset in Fig.2.54 shows a good match between radio, x-ray and the part of the 1600 Å emission that come from the footpoints.
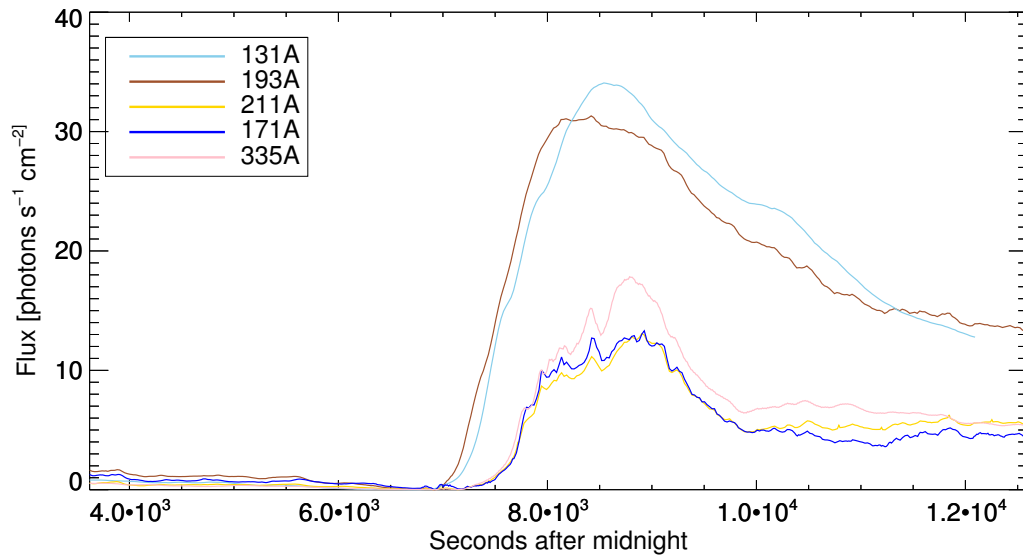
Figure 2.53:   EUV lightcurves for the May 13 flare. In these lightcurves no clear evidence of repetition pattern is found.

The delay between radio and x-ray is shown in Tab.2.7 which shows that there is always a delay in radio emission, while the emission from the footpoints seems to be simultaneous, even though the *SDO* satellite at 1600 Å has a cadence of 24 sec.
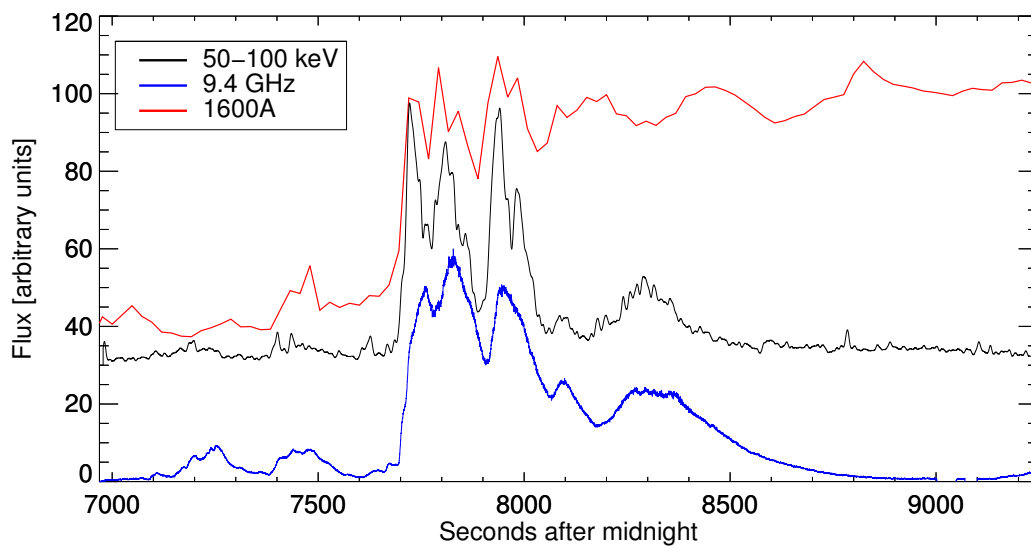
Figure 2.54: Comparison between lightcurves at different energies. Top (red) 1600 Å , middle (black) is *RHESSI* 50 - 100 keV, bottom (blue) is *NoRP* 9.4 GHz.We have to keep in mind that this is a flare on the limb and the footpoints are not clearly visible, and the emission during the impulsive phase is comparable with the cooling phase. Nontheless the temporal pattern of the lightcurve at 1600 Å is consistent with the emission in 50 - 100 keV.

Chapter 3

Discussion

3.1 Energy dependent delay

3.1.1 Radio vs. Radio

I carried out several timing analyses on radio lightcurves (from 1GHx to 80 GHz) and X-ray (12 keV - 300 keV). I performed cross correlation between different channels using the whole lightcurve and, then analyzed single substructures in different channels when they were clearly discernible,. The peaktime was measured "by eye" instead of fitting the peaks with some function because the fitting process could impose a model on the shape of the peaks, and produce systematic errors. I also tested the effects of the subtraction of the underlying trend on the cross correlation analysis.

The most detailed comparison was for May 14 flare, where some substructures were present on almost every lightcurve. In general, the delays between frequencies behaved systematically: one of the frequencies peaked first and the other frequencies followed. The maximum measured delay was 40 sec relative to the peak H between 2 GHz and 35 GHz (the latter peaked later). For other peaks from the same flare, the first peaking frequency (hereafter ν_{fp}) isn't always the same but appears to shift from high frequencies (35 GHz in peak A) to low frequencies (2 GHz in peak H). So as the time increases, ν_{fp} decreases, as shown in Tab.2.5 and in Fig.2.40.

For the May 15 flare the higher frequencies have too low a SNR to distringuish substructures, so only frequencies from 1 GHz to 17 GHz have been used. In this flare ν_{fp}=17 GHz for all substructures with the exception of peak B, where ν_{fp}=9.4 GHz. I performed a cross correlation between lightcurves after detrending the emission by subtraction. To test the consistency of the result I computed two trending curves for subtraction: the first trend was computed convolving a gaussian with σ=100pts, and the second trend with σ=500pts. In both cases the delay behavior is preserved (i.e. ν_{fp}=17 GHz).

For the May 13 flare the structure of the lightcurve impedes the identification of peaks so I computed the cross correlation using the X-ray 50-100 keV lightcurve as the time

reference, fnding that ν_{fp}=17 GHz and the other frequencies are delayed.

Liu et al (2015) found a similar behavior for the emission during the flare of 2005 Feb 22, finding that for one of the substructures the 17 GHz lightcurve peaked first. Their interpretation of the phenomenon follows the studies by Takakura and Scalise [1970] and Wiehl et al. [1980]. Takakura and Scalise [1970] propose that the emission comes from the second harmonic of the gyrosynchrotron emission in a bipolar-like structure and compute the height at which that emission is stronger. The resulting emission at 9.4 GHz comes from a lower region in the atmosphere while lower and higher frequencies are emitted higher in the loop. Wiehl et al. [1980] hypothesize that the emission at different frequencies are due to the passage of a conduction front that starts at the heated footpoints and rises along the loop at the ion sound speed, crossing the locations where the emission at a given frequency is generated: the conduction front promotes emission at progressively higher parts of the loop so the field is lower and the density is lower.

through the part of the loop where the emission at each frequency is higher, giving rise to the observed delays.

This model does not explain why the critical frequency that peak first drifts from higher to lower frequencies with time. I suggest that this effect can be explained by the arcade rising, since both the accelerating and trapping regions move towards regions of the atmosphere where the magnetic field and the ambient density are lower. This does not , however,explain why two of the eight peaks (peak C and maybe peak D) do not show a well defined behavior. The peak delays are also due to the refractive index of the medium through which the waves travel before reaching the observer. A change in density or in temperature can produce a change in the refractive index and then produce the drift.

3.1.2   X-ray vs. Radio

I made the same analysis for the X-ray vs. X-ray finding that no definite behavior was recognizable. Also, LaRosa and Shore [1998] showed that cross correlation techniques for the computation of single peaks delay could fail if the spectral index of the flare is not constant, so the technique used by Aschwanden and Schwartz [1996] can give wrong results. The comparison between the peak time in X-ray and radio showed that, in general, *the X-ray emission leads the radio emission*. Even when the timing of the X-ray emission comes later than ν_{fp}, the timing is still compatible with the general rule within the errors.

What is actually happening is still matter of debate. If the explanation from Liu et al. (2015) is correct, we can say that when the particles are accelerated, those having a lower pitch angle will simply stream towards the footpoints and produce X-rays, while the conduction front moves towards the part of the loop where the emission at a given frequency is maximum. What we know is that the X-ray emission is coincident with the emission from the footpoints, given the cadence of the AIA instrument. The simplest model we can think

of is that, regardless of the process, a population of electrons is accelerated or heated. The distribution of energy will be such that some of the particles will have a pitch angle small enough to enter the loss cone. These will directly precipitate towards the photosphere where they will deposit all their energy through *thick-target bremsstrahlung*. The electron with a high pitch angle remain trapped near the looptop, mirroring along the arms of the loop and emitting through gyrosynchrotron untill when, probably by scattering, their pitch angle will be reduced and they will eventually precipitate.

Dolla et al. [2012] made an analysis on the emission from the X2.2 flare occurred in 2011 February 15. They analyzed an even broader range in the electromagnetic spectrum, and they find that: quasi-periodic pulsations (QPPs) are present, probably due to electron beams injected at different time or modulated by MHD waves; the precipitating particles are responsible of the hard X-ray emission through bremsstrahlung, while higher energy electrons are delayed by trapping effects, so the fluctuations appear first in the X-rays, then in the radio.

Several authors have tried to explain this effect: Cornell et al. [1984a], Lu and Petrosian [1990] and Lee and Wang [2000] among others. But the matter is still being debated and directly related to the other major unresolved phenomenon – particle acceleration.

3.2   Gamma-ray spectra with Fermi/LAT

The role of different flare particle acceleration mechanisms are still not well identified, nor are the relative contributions of electrons and protons in the emission from the flare site. Although the flares in this thesis show no evidences of proton emission, a substantial number of recently studied flares show emission $\geq 100\mathrm{MeV}$.

Ackermann et al. [2014] analyzed in detail the γ-ray energy emission from two M-class flares occurred in 2011 March 7 and 2011 June 11 that showed long lasting, high energetic emission. The March event showed γ-ray emission lasting for 13.3h which is longer than the EGRET instrument on board of the CGRO had ever measured. Moreover, this flare was a "modest" M-class flare, which suggests that energetic Long Duration Events (LDEs) are not exclusively produced only by X-class events. These flares were also associated with CMEs. They combined Fermi/LAT observations with *RHESSI* and *SDO* which located the emission on the Sun, ruling out the CME showk as the acceleration site of γ-ray emitting particles, since at the time the radiation was observed the plasmoid would have been at $100\mathrm{R}_\odot$. They suggest that stochastic acceleration by turbulence is the more plausible mechanism. Although their data could not discriminate between electrons and protons as the agent for LDE, they propose that to accelerate electrons to the requisite energies, very short acceleration timescales are required[1] because most of the energy is emitted rapidly by energetic electrons as synchrotron radiation. In contrast, the energy required to accelerate

---

[1]This constrains the acceleration region in a very small space, which is a situation very difficult to reach.

protons in a way compatible with the observations is actually modest. They find that the total energy in γ-ray emitted during the LDE is several hundred times less than the HXR emitted during the impulsive phase making the proton hypothesis more plausible. Finally, they argue that the *common trap-precipitating model* is not compatible with the spectral evolution of the particle spectrum. They say that this model should lead to a hardening of the particle spectrum because the trapping efficiency needs to be higher for higher-energy particle. Instead they observe a gradual softening of the spectrum suggesting that the acceleration process is active throughout the whole LDE.

3.3 Comparison of the May 13 event with the paradigmatic "Masuda flare"

The Yohkoh[2] satellite produced one of the most remarkable observations in the history of the study of solar flares. It caught a flare on 1992 Jan 13 that had the peculiarity of being located on the limb. Limb flares are very useful despite the fact that the surface is not visible. They permit observing arcades or single loops from the side, consenting the unambiguous location of the emission at different altitudes in the solar atmosphere free of projection effects.

The observation was so important that this flare was named "the Masuda flare". Masuda et al. [1994] concluded that the acceleration region was ∼7Mm above the looptop, and, inside the acceleration region, the hard X-ray emission was coming from a location above the soft X-ray emission site. As shown in Fig.2.51, the combined observations using *SDO /AIA* and *RHESSI* let us compare the 2013 May 13 flare to the Masuda flare. We can see that the 6-12 keV emission is located 3.6 ± 2Mm above the looptop, while 25-50 keV emission is higher, 7.7 ± 2Mm from the looptopwould mean that the harder emission is slightly more distant from the looptop than the softer one. The distance between the two emission region has been computed as 5.7 ± 2Mm. We see also a clearly distinct source of hard X-ray emission located at one of the footpoints (the other footpoint is not visible, probably because is located behind the limb). So we can say that we resolved a different location for different energy channels but the statistical significance is not high because we are still observing the two-dimensional projection of a three-dimensional structure and we may be biased by that (but the Masuda flare is similar in this sense). Although the observed X-ray energy channels are different between these two events we can still say that the May 13 event is compatible with what Masuda et al. [1994] found.

---

[2]This satellite had two instrument to observe soft XRs (SXR) with the "SXT" instrument and Hard XRs (HRX) with the "HXT" instrument. The spatial resolution was 2.45"x2.45" for the SXT and 5"x5" for the HXT. Website: http://ylstone.physics.montana.edu/ylegacy/
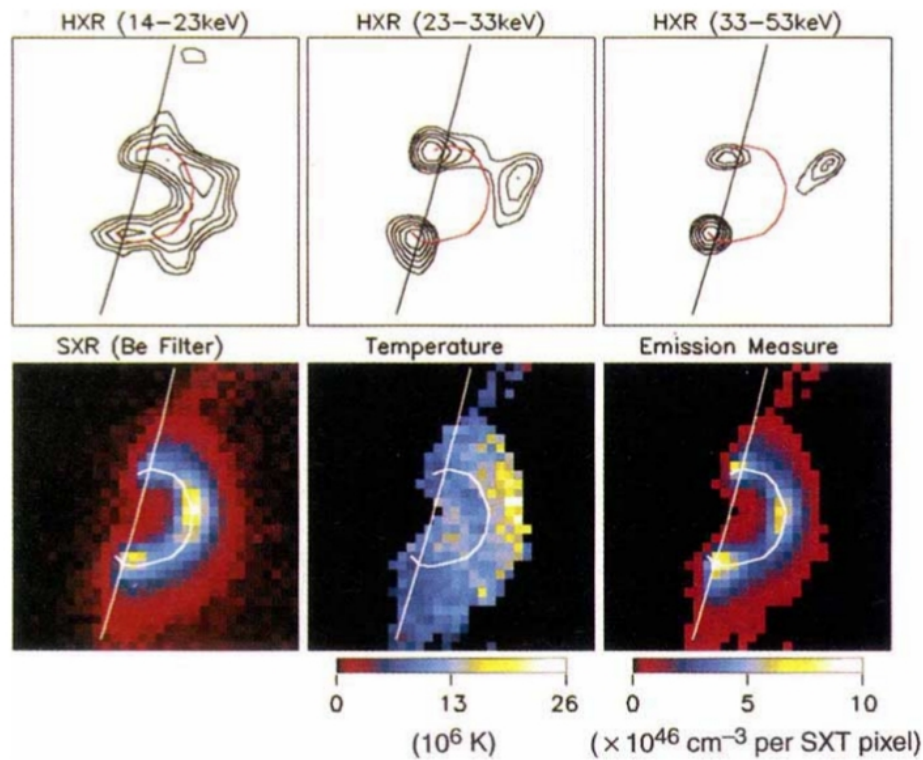
Figure 3.1: adapted from Masuda et al. [1994]. The surface is to the left and the flare footpoints are clearly seen in the 33-53 keV channel. The upper row shows that there is diffuse soft x-ray emission along the loop and as the energy increases, the loop ceases to emit while the only emitting region are at the looptop and at the footpoints. The emission shown in the middle panel (23-33 keV) show also an elongated structure which start at the loop and goes towards the footpoint, which is comparable (in both shape and energy channel) to what I show in Fig.2.51

3.4   Emission Pattern Repetition and Loop Oscillations

The EUV emission is from the loops with no footpoints contribution. Kumar et al. [2013] show an observation of an isolated loop next to a flaring region. They see a wave-like intensity enhancement that propagates along the loop and reflects a couple of times at its end. The timing of the oscillation is consistent with a magnetoacoustic wave propagating along the loop. Their hypothesis is that the flare triggered the injection of plasma into the loop near the footpoint, causing a standing wave inside the loop.

Wang et al. [2003] observed what they interpreted as a slow magnetoacoustic standing wave in 27 observation using SUMER[3]. They found that:

- the phase speed of the wave is comparable with the sound speed inside the loop;

[3]SUMER (Solar Ultraviolet Measurements of Emitted Radiation) in an instrument on board of SOHO (Solar Heliospheric Observatory) which is a satellite orbiting around the L1 point and facing the Sun. The SUMER instrument is a UV spectrograph observing in a range from 1500 Å to 390 Å . More information at http://www2.mps.mpg.de/projects/soho/sumer/text/webluca/ch_inst.html

- the intensity fluctuations lag the Doppler shifts by 1/4 period; this is expected for a standing wave, and not a propagating one;

- the scaling between the slow wave dissipation time and the period agrees with their observation.

Selwa et al. [2005] computed a one dimensional model of a magnetic loop that included main damping mechanisms. That simulation shows that an impulse at one footpoint of a loop can excite the fundamental mode of a slow magnetoacoustic standing wave, while an impulse at the looptop excites the first harmonic of the same wave.

Aschwanden et al. [1999] show that for a slow standing magnetoacoustic wave the period of oscillation is:

$$\tau_{slow} = \frac{2L}{jc_T} = \frac{2L}{jc_0}\left[1 + \left(\frac{c_0}{v_A}\right)^2\right]^{-1/2} \approx 1300\frac{L_{10}}{\sqrt{T_6}}s \tag{3.1}$$

where c_0 is the sound speed, $c_T = \frac{c_0 v_A}{(c_0^2 + v_A^2)^{1/2}}$, L_{10} is the length of the loops in units of 10^{10}cm, T_6 is the temperature in units of 10^6K, and the approximation is in the limit where $c_0 \ll v_A$ and $j = 1$ (the number of the mode).

I tested this hypothesis for the flares in my study to check whether the repetition pattern could be caused by such a wave, excited by the cool material at the photosphere which is heated by the electrons energized by the reconnection process in the corona, filling the loop after the impulsive phase of the flare. While my data cannot unambiguously distinguish the kind of perturbation present in these loops, we rule out everything having a phase speed similar to the Alfven speed because, in that, case the period is much shorter than what we observe. The slow magnetoacoustic wave is the best candidate because the timescale is comparable to that of a pressure wave and because the slow magnetoacoustic wave has a phase speed equal to the minimum between the Alfven speed and the sound speed. Further, the loops have at an average temperature of $2 \cdot 10^6$K, with a length of $\sim 0.8 \cdot 10^{10}$cm, using eq.3.1 we find values for the period that are consistent with the observed periods within an uncertainty of $\pm 10\%$.

It is difficult to discern the presence of oscillations when many loops compose an arcade. Nontheless these oscillations have been seen during observations of single loops. White et al. [2012] found evidence for an oscillating loop in bands 94 Å and 131 Å using the *SDO /AIA* instrument,during the event of 2010 Nov 3. They estimate a loop temperature between 9MK and 11MK, since the loop is invisible in other AIA bands (for instance, 171 Å is a diagnostic for a temperature of $\sim$1MK). As shown in Fig.3.2 they used the method of cutting a line of pixel from each frame to create a space vs. time plot (the same procedure I used for Fig.2.44), and then represented the oscillation of two strands of the loop using a damped cosine. They find that the two strands had a period of 302 $\pm$ 14 sec and 291 $\pm$ 9 sec. They first hypothesize that the plasma is injected in the loop from one footpoint
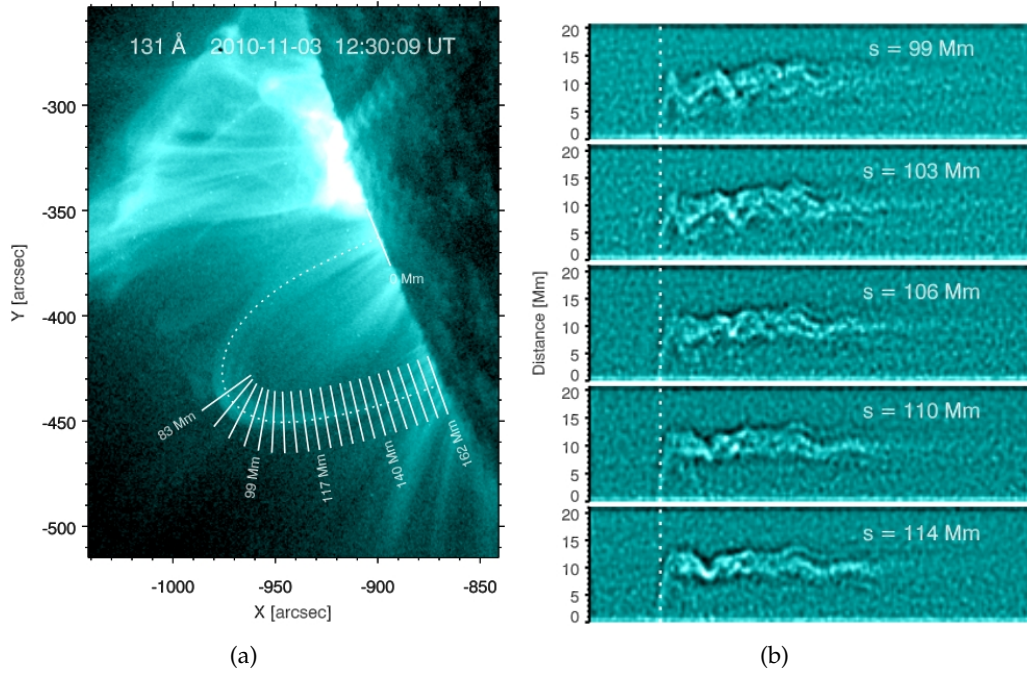
Figure 3.2: Images adapted from White et al. [2012]. Panel *(a)* shows a frame of the observation and the orthogonal cuts on the loops at the distances where the oscillations were computed. Panel *b* shows the profile of oscillation of five different part of the loops.

during the impulsive phase, triggering a fundamental slow magnetoacoustic mode (Selwa et al. [2005]). But the oscillation period is incompatible with the magnetoacoustic mode since its period is about 30min. Instead, they propose that the formation of the loop follows ejection of a plasmoid and that the loop is filled later, after the impulsive phase has ended, and that a second or third harmonic of the kink mode is generated. Thus oscillations of loops are clearly seen in single loops and simulation have shown that different kind of perturbation can trigger different kind of waves (Selwa et al. [2005]).

3.5   Quasi Periodic Pulsation (QPP)

One of the most remarkable features in solar flare lightcurves is the large number of peaks with no well defined periodicities on timescales from a few seconds to several minutes. Usually called "quasi periodic pulsation" (QPP), they appear across the whole electromagnetic spectrum, from radio to X-ray, as has also been shown in this thesis. The QPPs were used in this work to analyze the time of arrival of different frequencies in the radio lightcurves and to compute the delay of the radio emission with respect to the HXR emission (sec.3.1.1), but the physical mechanism that produces this behavior is still under investigation.

Although my analysis of the intrinsic periodicity is not shown here, I performed both Fourier analysis and Wavelet analyses to search for well defined periodic components.

None of the analyzed lightcurve showed any statistically robust periodicity. This result is in line with Gruber et al. [2011]. They used the method proposed by Vaughan [2005] to analyze four impulsive solar flares that showed a lightcurve that seemed periodic. The method uses not-detrended lightcurve and takes into account the fact that solar flares show an intrinsic property: the continuum emission can be approximated as red noise. They first tested the method analyzing the lightcurve of a flare occurred in 2005 Jan 1 which had also been analyzed by Nakariakov et al. [2010] who used the usual "Lomb-Scargle periodogram" (LSP) analysis. Then they repeated the analysis using the Vaughan method. Nakariakov et al. [2010] used *RHESSI* data, having an intrinsic 4 secec periodicity due to the rotation of the satellite, and they used the LSP method to check whether any periodicities could be statistically confirmed. They showed that the LSP revealed two components: one at 0.25Hz was clearly due to the rotation, and another component at 0.025Hz, interpreted as a periodicity due to different reconnection processes triggered by a kink mode oscillation present in a loop near the flaring region. When Gruber et al. [2011] analyzed the same lightcurve using the Vaughan [2005] method, they found the 0.25Hz systematic but found no other periodicities. They conclude that long term periodicities are artifacts of the detrending. Gruber et al. [2011] applied their method to four flares using the GBM, finding that, even though our eye can see some periodicity in the signal, the periodicity is not statistically robust. This is a clue for the origin of the QPPs: the fact that no periodicity is found in the analysis is not enough to rule out some oscillatory instabilities, but may point to stochasticity as an intrinsic property of the acceleration process leading to QPPs in the emission.

3.6   Flux emergence

Magara and Longcope [2002] present a 3-dimensional MHD numerical simulation of the emergence of a magnetic flux tube into the solar atmosphere. They modeled a stratified atmosphere divided into four zones: sub-photosphere, photosphere, low corona, and high corona. The physical parameters of each zone are chosen to produce a model that is realistic, with some small modification to reproduce the temperature and gravity profile in the atmosphere, and they ignore nonadiabatic processes and do not include feedback from the magnetized region to the heating of thew overlying chromosphere an corona. The simulation starts with a horizontal tube of twisted flux embedded in the sub-photosphere (Fig. 3.3). Then the simulation evolves and the results are shown in Fig.3.5.

Fig.3.5 shows three of the last 20 steps of simulations which are the ones that appear to be in best qualitative agreement with the observations. We see that show clearly that the underlying flux tube gradually rises in the atmosphere and the footpoints move apart much like the behavior observed in the May 15 EUV data. In the simulation, each timestep is 49 sec, the length scale is L=540 km and the strongest magnetic field in the region is ~1500 G (Fig.3.5) which yields a simulated region having a total length of ~20000 km and
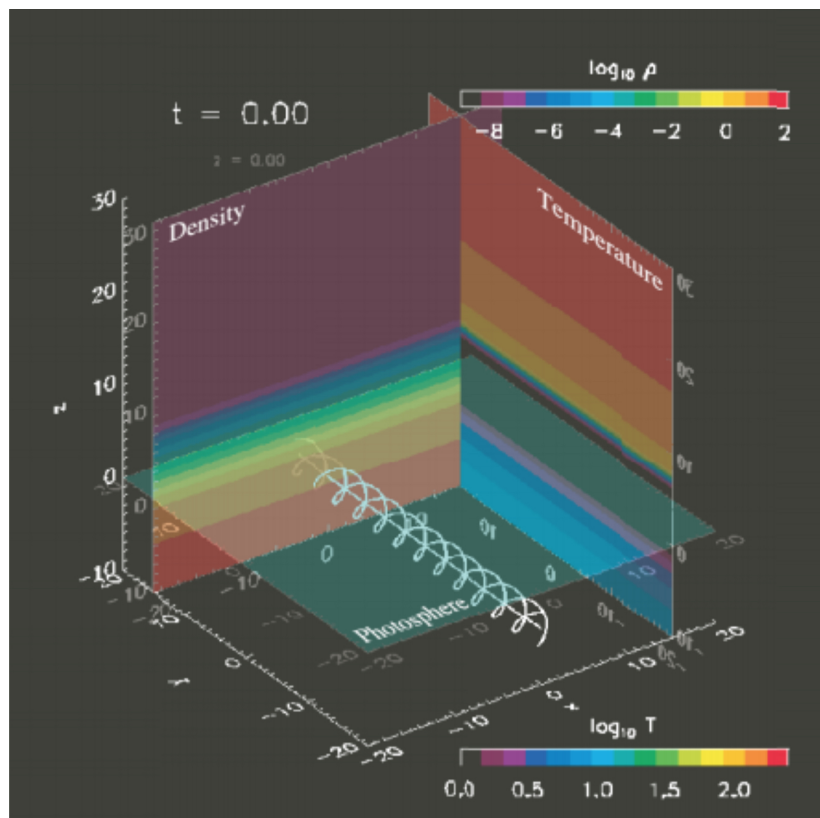
Figure 3.3: The initial stage of the simulation. It shows the photosphere (horizontal layer) and the flux tube is completely submerged under it. The vertical color maps show the variation in temperature and density. The units of the color bars are the logarithm of the scaling factor with respect to the photospheric values. From Magara and Longcope [2002]
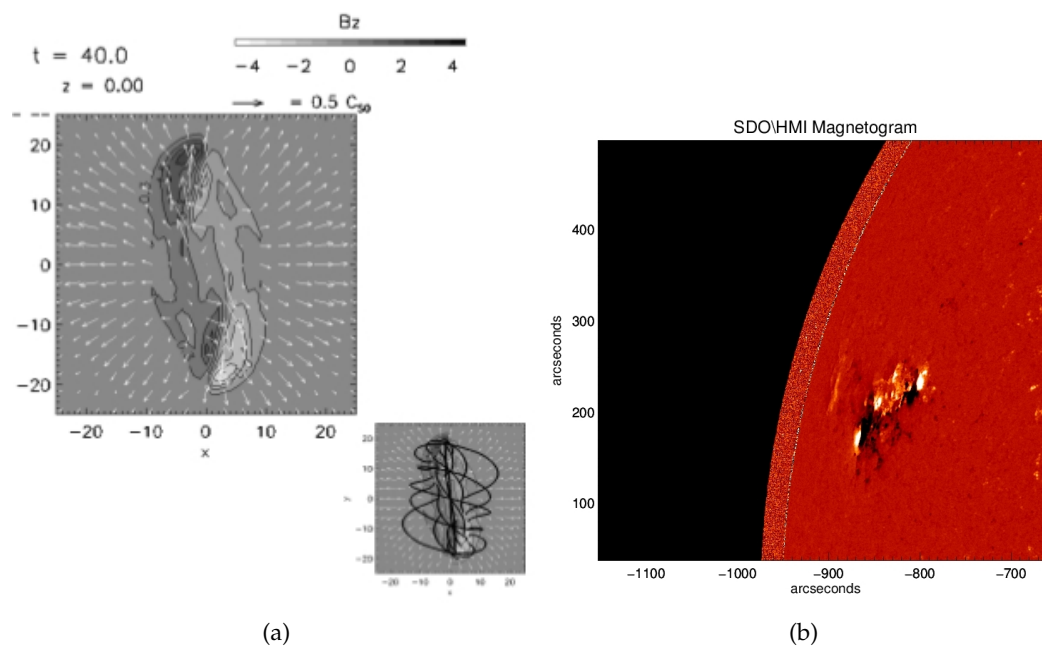
Figure 3.4: Panel *a* shows the simulated magnetic field on the surface from Magara and Longcope [2002]. It shows two pairs of strong field concentration at the two sides of the region and weaker magnetic field positive on the right side and negative on the left side. Panel *b* shows the observation of the photospheric magnetic field at the end of May 15 event. It also shows two couple of strong field at both the eastern and the western side, weaker positive magnetic field on the nothern side and negative magnetic field on the southern side.

a total timescale for the rising of the arcade of $\sim$1000 sec. For comparison, the observed active region has a measured total length of $\sim$60000 km and an estimate timescale for the rising of the arcade of $\sim$3000 sec.

Moreover, they simulated the photospheric magnetic field showing a structure having two pairs of of strongly concentrated magnetic fields (of both signs) at both ends of the region, one half of the region dominated by a weaker positive magnetic field and the other half dominated by a weaker negative one. Fig.3.4 shows a comparison between the simulated region and the real one: the modeled structure is quite similar showing that both the simulation of the emerging loops and the simulation of the photospheric magnetic field is compatible with the observed data. It is worth noting that the simulated region has no relations with the observed one, and the fact that the simulation is qualitatively comparable with the real observation suggests generic behavior from the simulation relative to the Sun.

Taking a step forward, if the sub-photospheric flux tube is larger and twisted enough, the following scenario presents itself: *(a)* the flux tube start rising; *(b)* the external loops of the flux tube expand in the atmosphere and are expelled because of reconnection; *(c)* buoyancy continues to push the flux tube out of the photosphere letting other loops to expand; *(d)* reconnection again occurs and the process continues until the stresses in the flux tube are sufficiently relaxed. To test this hypothesis I used *SDO /AIA* observations covering the period May 13-15. The *AIA* imaging showed that at least two of the expelled loops during the May 14 event had emerged during the previous event. This is consistent with the hypothesis that a large sub-photospheric twisted flux tube rose from beneath the surface due to buoyancy, gradually exposing the bundled loops that are then expelled releasing magnetic energy and relaxing the system.

3.7   Stellar flares

The ubiquity among the stars of the processes we see on the Sun, such as differential rotation, convectively driven acoustic oscillations, presence of an X-ray emitting corona, and a dynamo generated magnetic field and starspots, have been demonstrated repeatedly over the past decades and flares are no less omnipresent. The Kepler[4] spacecraft is designed to observe a group of stars in the Milky Way galaxy to search for extrasolar planets by looking at the small changes in the white-light lightcurve of the stars: when a planet transits the star, the observatory should see a dip in the lightcurve. Since the instruments were continuously observing these stars for four years, not only dips were observed but also a large number of flares, and not only in G stars like our Sun but also in M, K, F and A stars.[5]

---

[4]Kepler website: kepler.nasa.gov

[5]In fact, this demonstrates that "one person's noise is another's science". Starspots and flares confuse the period searching routines designed to detect transits and distort the light curves. The wealth of data that will
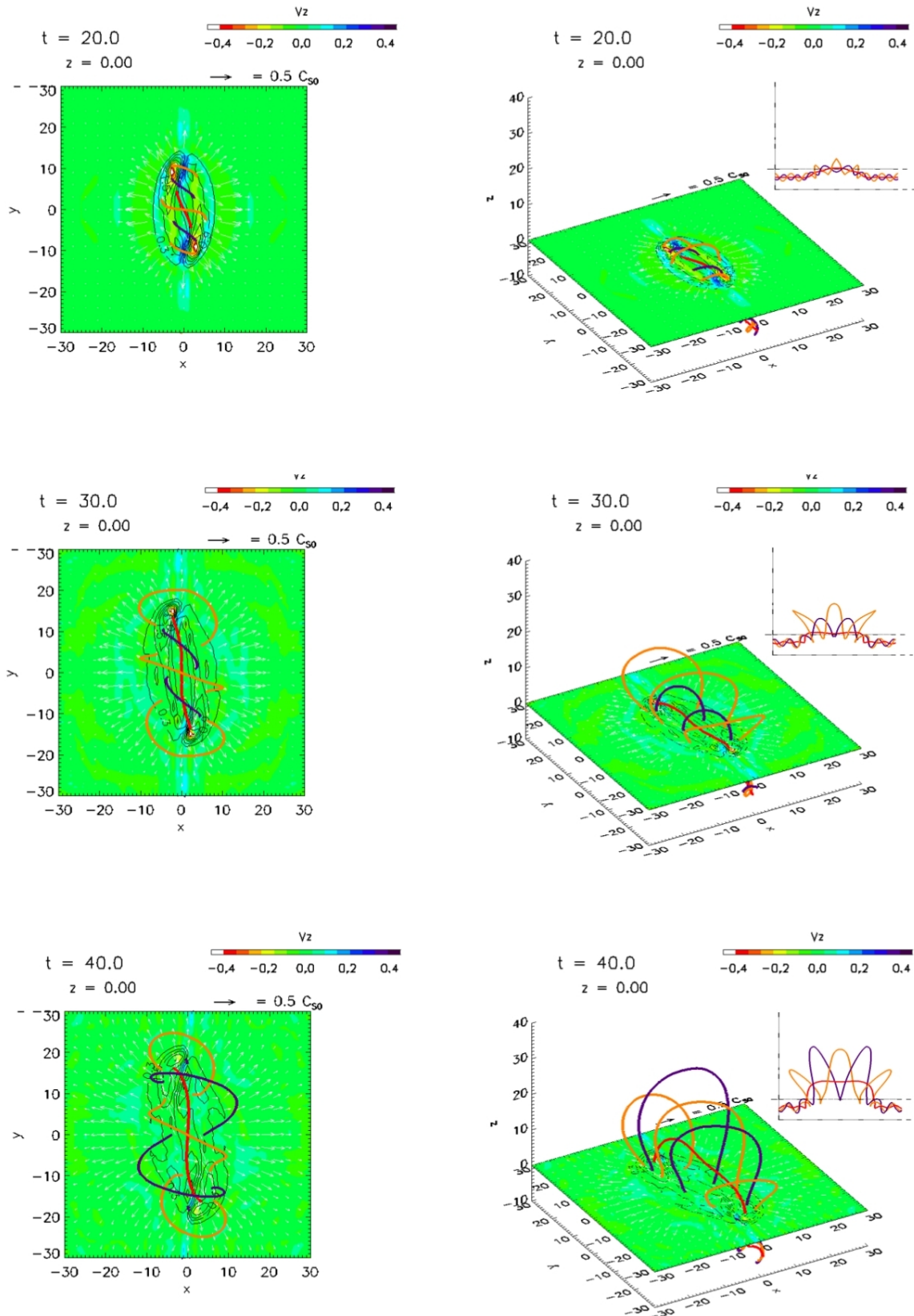
Figure 3.5: Three phases of the simulation from Magara and Longcope [2002] are shown. Top row shows the first loops emerging from the photosphere and this is similar to what *SDO /AIA* observations show for the beginning of the flaring event. Middle and bottom rows show the evolution of the flux tube emerging in the atmosphere.

These are called super-flares because usually the energy emitted is $\sim 10^6$ times greater than solar flares. The fact that we observe only super-flares does not mean that the Sun is different from the other stars but just that the sensitivity of the instruments is such that weaker flares are not observable: if a twin of our Sun would have been in the field of view, Kepler would have not observed any flare on it.

Many studies have shown the presence of stellar flares since they were first identified among the emission line M dwarf stars (the dMe stars) in the 1940's. For instance Walkowicz et al. [2011], Maehara et al. [2012], Shibayama et al. [2013] and Balona et al. [2015] analyzed white light lightcurves to check whether they present common properties with the emission we observe on the Sun, with the limitation that we do not observe flares in white light on the Sun because it is very difficult to observe, and even a strong solar flares are hardly visible. Balona et al. [2015] analyzed 3140 flares in 290 stars, finding 257 flares in 75 stars with a sufficient SNR to detect possible structures in the lightcurve. Among all the stars which presented flares, they claim to have found seven flares on five stars whose lightcurve showed QPPs with timescales between few seconds and several minutes. They say that no *direct* link can be done with the QPPs found in HXR and radio emission from solar flares but the mechanism that creates it may be the same and further investigation is certainly warranted. Hence, this thesis is just the beginning.

---

come from the extended mission has yet to be mined.

Chapter 4

Instruments

To obtain a pan-spectral, comprehensive dataset for each flare covering a broad range of physical siagnostics required using four different, independent observatories:

- Nobeyama Radio Polarimeter (*NoRP*);

- Solar Dynamics Observatory (*SDO*);

- *Fermi* Gamma-Ray Space Telescope (Fermi).

- Reuven Ramaty High Energy Solar Spectroscopic Imager (RHESSI)

4.1   The Nobeyama Radio Polarimeter (*NoRP*)

The Nobeyama radio polarimeter consist of eight antennas on six different mounts, observing both total flux and polarization at 1, 2, 3.75, 9.4, 17, 35 and 80 GHz (see Fig.4.1). Torii et al. [1979] and Shibasaki et al. [1979] describe the antennas from 1 to 9.4 GHz and Nakajima et al. [1985] deal with those from 17 GHz to 80 GHz.

Each antenna is fully automatic and follows the same routine every day: in the morning, it is oriented toward sunrise and it follows the Sun untill sunset. The receiver gain calibration is done about every three hours and lasts two minutes, using an argon-tube noise generator kept in a temperature-controlled box. The receiver input is switched to the argon-tube for one minute, then the argon-tube is turned off for one more minute, after which, the receiver is back on source.

The antennas from 1 GHz to 9.4 GHz operated at Toyokawa Radio Observatory since 1979 and were moved to Nobeyama in 1994, the 17 GHz antenna has been online since 1978, the 35 GHz since 1983 and the 80 GHz since 1984. This homogeneous data from Nobeyama are suitable for both the analysis of small duration events like a flare, and for a long term analysis of solar radio emission.

The data are public and available online at the Nobeyama Radio Polarimeter website The available data ready for the analysis in IDL are divided into:

Figure 4.1: Nobeyama Radio Polarimeter, image from http://www.nro.nao.ac.jp/en/gallery/images/rp_002.jpg. On the left there's the single mount with three antennas, where the central one is for the 35 GHz observations while the other two are for the 80 GHz observations; the other antennas, from left to right, are for 17, 9.4, 3.75, 2 and 1 GHz observations.

Nominal Freq (GHz)	1.0	2.0	3.75	9.4	17	35	80
Real Freq (GHz)	1.06	2.06	3.7325	9.411	n.d.	n.d.	n.d.
Diameter of the Paraboloid (cm)	300	200	150	85	85	30	25
"Null to null" beamwidth (deg)	7.4	5.6	3.8	2.6	1.67	1.0	1.02

Table 4.1: Summary of the specifications of the radio-polarimeters

- Daily Light Curve: a light curve for each frequency, covering the whole day from sunrise to sunset. The cadence is 1 s;

- Event Light Curve: a light curve for each frequency, covering the time window during which an event occurs. The cadence is 0.1 s.

The daily light curve goes from 22:09:59 UTC to 07:09:52 UTC at the winter solstice, while it goes from 20:59:59 UTC to 08:59:59 UTC at the summer solstice. The event light curve covers only the time over which the flare is ongoing. This time window is determined by the Nobeyama Radio Heliograph: the *averaged correlation amplitude* (ACP) is constantly calculated, and the event time window is defined as the time during which the ACP is above the value of 0.01526 (see, http://solar.nro.nao.ac.jp/norh/doc/databook_vol3/).

The data are downloadable in "XDR" format, and include eight variables as follows:

- **DAY**;

- **FI**: contains all the seven components of flux density at each frequency. The right polarized flux is summed to the left polarized one (R+L);

- **FIAVG**: contains the average of the flux density at each wavelength;

- **FV**: contains all the seven components of flux density at each frequency. The left polarized flux is subtracted from the right one (R-L);

- **FVAVG**: same of FIAVG, but relative to FV;

- **FREQ**: list of the observing frequencies in unit of GHz;

- **MVD**: an array formed by 0 and 1, defining which point of the data are valid and which not;

- **TIM**: a structure containing the information about the time of the observation, in milliseconds elapsed after the midnight of the reference day.

The structure of the content of the "XDR" file is the same for both the daily light curve and the event data. However, there's a caveat when using these data in analyzing flares: the FIAVG and FVAVG values *may* be used as an estimate of the background, because they represent the daily average of the flux, computed after the automatic removal of the events data. This, in general, is a good approximation for the background. But it may not be always the case. The automatic removal of the events data do not include interference with artificial sources and the effect of the skyline (which is strong for frequencies above 4 GHz, especially in the early morning). To overcome this problem, at the beginning of every month, *NoRP* releases a list of daily average of the previous month[1], where all effects not related to the flare event are removed manually[2].

---

[1] Data available at ftp://solar.nro.nao.ac.jp/pub/nsro/norp/data/daily/.

[2] Dr. Masumi Shimoyo, private communication

These data are available only for the frequencies from 1 to 17 GHz, i.e. the frequencies for which any method for reducing the background noise has been used. Instead, two different methods have been used for the 35 GHz and 80 GHz observation to subtract the effects that cause fluctuations (see Nakajima et al. [1985]):

- *Compensation of the absorption of quiet sun by atmospheric emission*: this method is used for the 35 GHz radiotelescope to get rid of the fluctuations due to the change of the optical depth (τ) of Earth atmosferic clouds so that it is possible to observe also small flares. If we call T_Q the antenna temperature of the quiet sun and T_C the cloud one, we can say that the total antenna temperature T_A is given by:

$$T_A = T_Q\, e^{-\tau} + T_C(1 - e^{-\tau}) = (T_Q - T_C)e^{-\tau} + T_C \qquad (4.1)$$

  then, if $T_Q \simeq T_C$ (condition that can be reached by making an antenna with a certain, predetermined diameter), we have that $T_A \simeq T_C$ and the signal is essentially independent from τ.

  The signal is then calculated as the ratio $T_B\, e^{-\tau}/T_Q\, e^{-\tau}$, where T_B is the excess temperature due to a flare.

- *Correlation of two antennas to cancel the quiet sun component*: for the 80 GHz radiometer two small antennas are used separated by 330 wavelengths. The plot of the visibility function in Figure 4.2, calculated with the 17 GHz interferometer (described in Nakajima et al. [1980]), shows that the correlation between the signal of two antennas whose beams cover the full Sun goes to zero for some values of the distance between them. So, when the visibility is zero, the signal coming from each of the two antennas is completely uncorrelated, while the system has still full sensitivity to a signal coming from a region smaller than the full disk, thus removing the fluctuations of the quiet Sun. The two antennas are mounted on a common equatorial mount so the projected baseline remains constant during the day.

4.2 The Solar Dynamics Observatory (*SDO*)

The Solar Dynamics Observatory is a space telescope that has on board three main imagers (see Pesnell et al. [2012] and Fig.4.3):

- the Atmospheric Imaging Assembly (*AIA*);

- the Extreme ultraviolet Variability Experiment (EVE);

- the Helioseismic and Magnetic Imager (HMI).

It was launched on 2010 February 11 from Kennedy Space Center. It is in geosynchronous orbit with an inclination of $28°$ at 35800 Km above its ground station in New
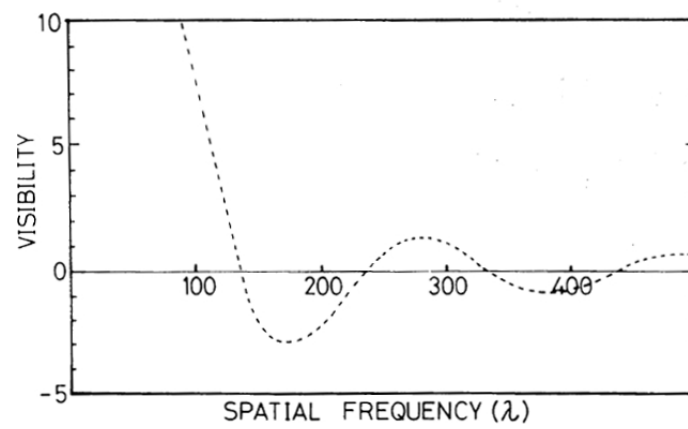
Figure 4.2: Visibility function for the quiet Sun calculated using the 17 GHz interferometer. When the function crosses the zero point, the quiet Sun signal is uncorrelated, but the system has still full sensitivity to a signal coming from a smaller region of the sun. From Nakajima et al. [1985], Fig.1.
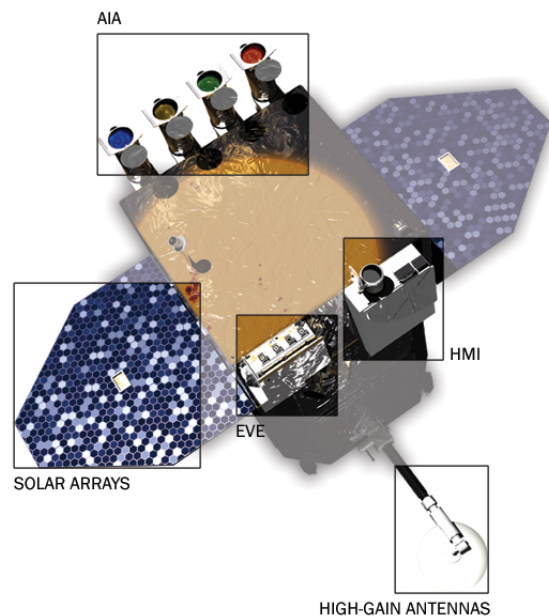
Figure 4.3: Image of the Solar Dynamics Observatory satellite. From sdo
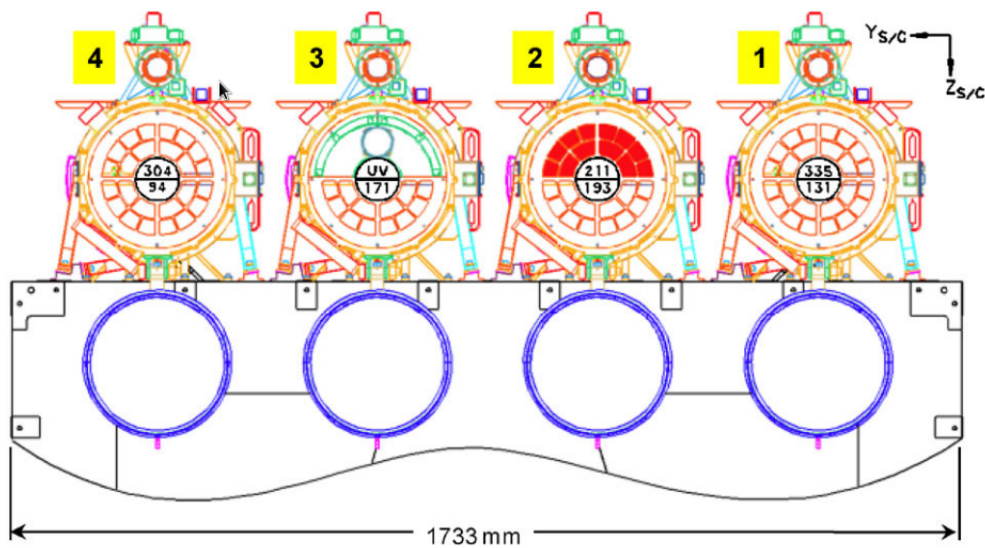
Figure 4.4: Schematic of the frontal view of the four telescopes composing the AIA instrument on board of the SDO. From Lemen et al. [2012]

Mexico. the orbit has an inclination of 28°. This orbit was chosen to permit continuous observations of the Sun and continuous contact with a single ground station. The satellite acquires a huge amount of data during the observation (a two hours observation at the highest cadence using the AIA instrument alone produces $\sim 5GB$ of data) and a low Earth orbit would have required an on-board storage system capable of recording the data when a ground station was out of sight, and multiple stations around the Earth for receiving data downlinks.

However, this of orbit has also some disadvantages: there are two three-week periods during which the Earth eclipses the Sun as viewed from the *SDO* and that the satellite is at the outer edge of the radiation belt, which means the satellite is continuously exposed to a high energy particle background that requires considerable shielding. In the following subsections two instruments will be briefly described.

4.2.1 The Atmospheric Imaging Assembly (*AIA*)

The Atmospheric Imaging Assembly (*AIA*) instrument is composed of four Cassegrain telescopes, each one at (at least) two different wavelengths (see Lemen et al. [2012]). The telescopes have a primary mirror of 20 cm and an focal length of 4.125 m, making it an f/20. The Table 4.3 summarize the recap of the characteristic of the telescopes.

The aim of this instrument is to imaging the corona and the transition region of the solar atmosphere. It observes in eleven bands *almost* simultaneously (see Table 4.2). In fact the primary mirror of each telescope has multilayer coatings with specific bandpasses.

The instrument observes narrow emission lines produced by the radiative de-excitation of coronal Fe ions. The ions may be either already ionized because of the temperature of
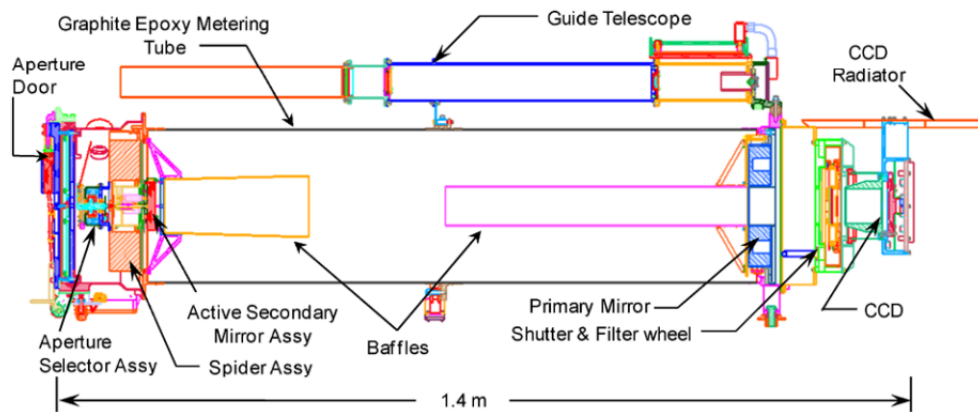
Figure 4.5: Schematic of the side view of the telescopes composing the AIA instrument. From Lemen et al. [2012]

the surrounding medium or they are ionized by collisions with streaming particles created during the reconnection process.

Each ionization state is sensitive to a particular temperature, since under coronal and chromospheric conditions collision dominate over photo-ionization. The higher the temperature, the stronger the collisions, and the more highly ionized the atom. For this reason we can associate a certain degree of ionization with a specific temperature.

However, the corona is not in thermal equilibrium because the density is so low that the time scale for the collision rate is lower than the time scale for the de-excitation so following collisional excitation the atom emits a photon at a precise wavelength that can then be observed by a telescope having some specifically tuned narrow bandpass filters.

Figure 4.4 shows the schematic of the frontal view of the four telescopes: telescope 1, 2 and 4 have two bandpasses and 3 has a 171 Å bandpass and a broad UV filter (1600Å, 1700Å, 4500Å).

Telescopes 1, 3 and 4 select the band by a filter wheel mounted in front of the focal plane (see Figure 4.5) while the telescope 3 has a blade in front of the aperture that selects which half of the primary mirror is to be used. Filters at the entrance of each telescope block both visible and infrared radiation, rendering the instrument blind to photospheric contamination.

4.2.1.1   The observations and the problem of the alignment

The observations have a maximum cadence of 12 seconds. The time required from the telescope to observe using both filters is divided into two exposures ≤ 2.9 seconds and the remaining time is needed for to readout the CCD and to switch filters (or the rotation of the entrance blade on telescope 3).

Since the satellite moves during the observation, the data will be taken from slightly different line of sight so two successive frames may be not perfectly aligned. The satellite

also suffers small rotations around the axis coincident with the line of sight, resulting in a small rotation of the acquired image.

Thus, if we want to display all the frames of an observation as a video, a correction should be applied, as explained in the following section.

4.2.1.2   AIA Data

The *SDO* satellite does not store any data on-board, but the data are continuously transmitted to the groundstation where they are sent to the Joint *SDO* Operations Center (JSOC) where the data (labeled as Level 0) are archived.

The Level 0 data are, then, processed to Level 1. The processing involves several step:

 i) the removal of the over-scan rows and columns (i.e. remove the residual charge on the CCD);

 ii) the removal of a dark image to account for the digital offset of the camera, CCD read noise and dark current;

 iii) the application of a flat field correction, to correct non-uniformities of the detector.

 iv) a correction is applied to individual pixel is applied to correct bad pixels. When a bad pixel is found, the information about the correction is stored so that further checks on that pixel are not required;

 v) the AIA images are flipped to put solar North at the top of the array.

The images are then fully calibrated and ready to be analyzed for scientific purposes. One advantage of the AIA is that it acquires high resolution images with a higher cadence than previous space solar missions, so the images may be displayed as a movie sequence. However the Level 1 data are not suitable for that purpose and an additional sequence of correction has to be made, i.e. they have to be processed to Level 1.5.

The process applies three corrections in a single step: rotating the image so solar North is at the top of the image, i.e. at 0°; the plate-scale size of the image is corrected to 0.6 arcseconds per pixel; the images are aligned in the north-south and east-west direction.

The last operation performed is the updating of the header of the images with the new informations.

4.2.2   The Helioseismic and Magnetic Imager (HMI)

The *HMI* instrument (described in Schou et al. [2012] and Liu et al. [2012]) observes the full solar disk in the Fe I absorption line at 6768 Å formed in the photosphere. It observes the Zeeman splitting to derive the line-of-sight (projected) photospheric magnetic field. The splitting is computed using (Fig.4.6):

Channel (Å)	Primary Ion(s)	Region of atmosphere	Log(T)
4500	continuum	photosphere	3.7
1700	continuum	temperature minimum, photosphere	3.7
304	He II	chromosphere, transition region	4.7
1600	C IV, IV + cont. (+ He II)	transition region, upper photosphere	5.0
171	Fe IX	quiet corona, upper transition region	5.8
193	Fe XII, XXIV	corona and hot flare plasma	6.2, 7.3
211	Fe XIV	active-region corona	6.3
335	Fe XVI	active-region corona	6.4
94	Fe XVIII	flaring corona	6.8
131	Fe VIII, XXI	transition region, flaring corona	5.6, 7.0

Table 4.2: Wavelength on which each filter is centered, the relative ion or ions, the part of the atmosphere observed and the characteristic logarithm of the temperature. From Lemen et al. [2012]

Mirror	Multilayer-coated Zerodur
Primary diameter	20 cm
Effective focal length	4.125 m
Field of view	41 × 41 arcsec
Pixel size/Resolution	0.6 arcsec (12 μm)/1.5 arcsec
CCD Detector	4096 × 4096, thinned, backilluminated
Cadence (Full frame readout)	8 wavelength in 12 seconds
Typical exposure time	from 0.5 to 3 seconds

Table 4.3: A recap of the characteristic of the AIA telescopes. It's worth noting that the nominal candence is from 10 to 12 seconds. Actually, 12 seconds is the shorter cadence available. The full table is in Lemen et al. [2012]
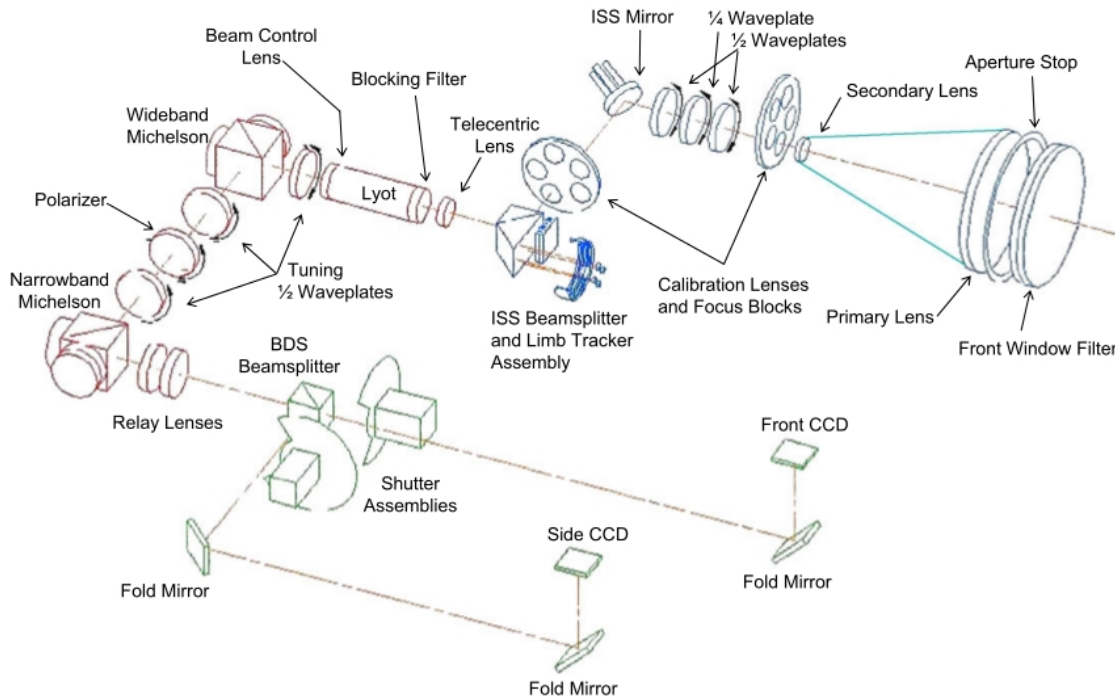
Figure 4.6: Schematic of the elements composing the *HMI* instrument. From Schou et al. [2012].

- a refracting telescope with 140 mm aperture and diffraction limit (λ/D) of 0.91 arcseconds;

- a polarization selectors which splits the light in left-circular polarization (LCP) and right-circular polarization (RCP);

- a set of filters (front window, blocker filter, tunable Lyot filter, Michelsons interferometers) which result in a tunable bandpass filter in steps of 76 mÅ with a total range of 690 mÅ around the nominal wavelength of the observed line (Fig.4.7);

- two 4096x4096 CCDs (front camera and side camera, pixel size 12 μm), which are very similar to the *AIA* CCDs except that the *HMI* CCDs are front-side illuminated, while the *AIA* CCDs are back-side illuminated.

The cadence of the instrument is 45s since the front camera acquires filtergrams at six wavelengths (by tuning the filters before each acquisition) for two polarization (LCP and RCP), for a total of 12 acquisitions, each one of them taking 3.75 sec. The filtergrams are sent to ground and reduced to compute the Zeeman splitting (which is proportional to the strength of the magnetic field) to obtain dopplergrams and line-of-sight magnetograms.
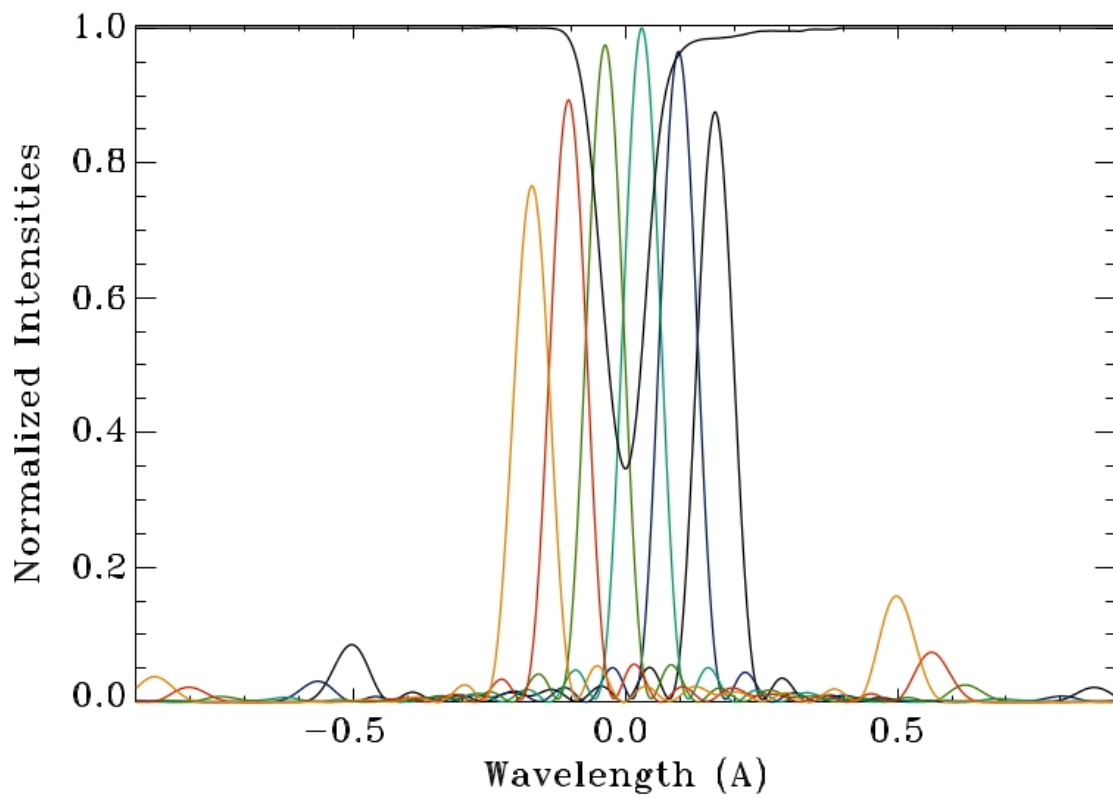
Figure 4.7: The black line in absorption represents the Fe I line at rest. The filters are tuned to obtain six bandpasses to measure different parts of the line and the distortion induced by the presence of the magnetic field. From Schou et al. [2012].

4.3   The *Fermi* Gamma-Ray Space Telescope

The *Fermi* satellite is a low Earth orbiting observatory that continually scans the sky in the energy range from 10 keV - 300GeV. It consist of two main instruments: the Large Area Telescope (LAT) and the Gamma-ray Burst Monitor (*GBM*) and represents a drastic improvement in the high energy observations relative to the Energetic Gamma Ray Experiment Telescope (EGRET) and on the Burst And Transient Source Experiment (BATSE), two of the instrumentsof the Compton Gamma Ray Observatory (CGRO, 1991- 2000).

The LAT instrument has a field of view (FOV) of 20% of the sky (2.4 secr) and it is capable of observing the whole sky every 3h (i.e. every two orbits). The standard observing mode, the "all sky survey", is such that during the first orbit it observes the nothern hemisphere, then during the second orbit it rocks southward and observes the southern hemisphere. Its FOV is so wide that every point in the sky is observed for 30min every 3h.

The *GBM* instrument is a "whole sky instrument" and continuously observes the whole unocculted sky, and was primarily intended as a low energy extension for LAT and as a "sentinel" for the discovery of Gamma Ray Bursts (GRB), but, as explaned later, it is also a very useful tool for solar flares observation.

Fermi was launched on 2008 Jun 11 on board of a Delta II rocket from Cape Canaveral. Its orbit has altitude of 550 km and an inclination of 25.6°. In 2013 NASA extended the mission for the period 2013-2018.

4.3.1   The Large Area Telescope (LAT)

The Fermi/LAT instrument is fully described in Atwood et al. [2009]. It is a *pair-conversion* telescope which consists of an Anti Coincidence Detector (ACD), a tracker and a calorimeter. The principle used to observe high energetic photons is based on the fact that when an high energetic photon encounter a high Z layer, it converts in a e^+-e^- (positron - electron) pair. The path of the pair is tracked and the direction of the photon is computed. Finally
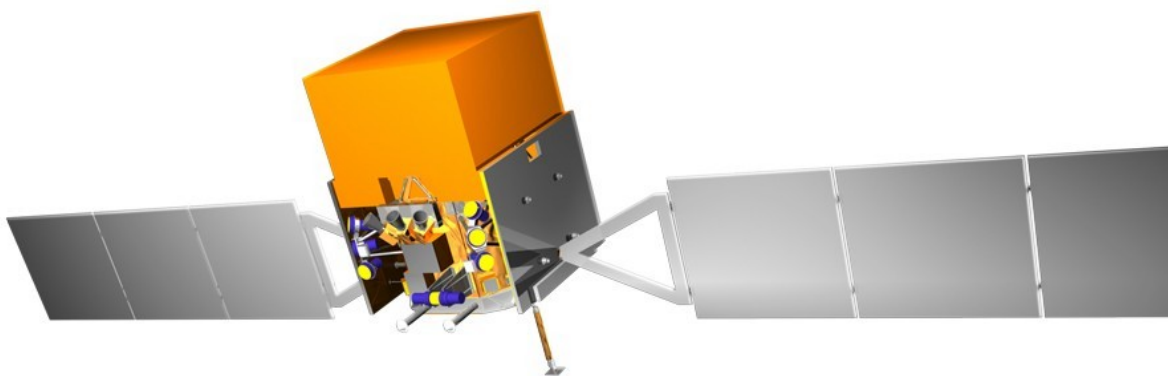
Figure 4.8: The *Fermi* Gamma-ray Space Telescope. From: http://gammaray.msfc.nasa.gov/gbm/
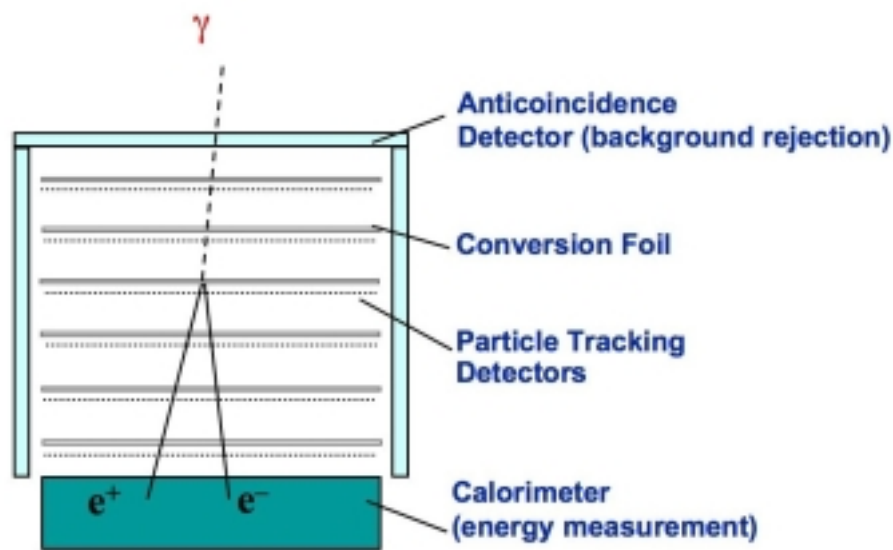
Figure 4.9: Schematic of the high energy photons tracking method. From: https://veritas.sao.arizona.edu/documents/Proceedings/Cannon_8th_INTEGRAL.pdf

the positron and the electron hit the calorimeter where they deposit their kinetic energy, the measurement of which yields the energy of the incident photon. (see Fig.4.9).

The *ACD* has the purpose of detect and reject the events produced by the observation of a cosmic ray (electron or positron) that can disturb the tracking of the particles created inside the telescope by the conversion of a photon.

has 16 planes of tungsten (conversion foil) between each two of which are layered the tracking planes. These consist of

The *Tracker* is composed by 16 towers (in 4x4 configuration) each of them has 16 planes of tungsten (conversion foil) between each two of which are layered the tracking planes. These consist of two layers of single-sided silicon strip detectors (to track both the x and the y position). When a photon hits a tungsten layer it converts into a pair and the position of each particle is computed by the tracking planes. The improvement with respect to EGRET is that no consumables (such as gas) are used by the instruments, thus avoiding both deterioration and exhaustion of supply and increasing the instrument lifetime relative to CGRO.

The *calorimeter* consists in 96 CsI(Tl) crystals for each of the 16 towers, where the kinetic energy of the particles in converted in a signal proportional to the deposited energy. It can measure energies up to few TeV.

4.3.2 The Gamma-ray Burst Monitor (GBM)

The *GBM* instrument consists of 12 NaI(Tl) detectors observing in the 4 keV - 2MeV range, and 2 BGO (Bismuth Germanium Oxide) detectors observing in the 150 keV - 30MeV energy

Quantity	EGRET	LAT
Energy Range	20 MeV - 30 Gev	20 Mev - 300 GeV
Peak Area	1500 cm^2	8000 cm^2
Field of View	0.5 sr	2.4 sr
Angular Resolution	5.8°	<3.5°(100MeV) - <0.15°(> 10GeV)
Energy Resolution	10%	10%
Dead Time	100ms	<100 μs
Source Location Det.	15′	<0.5′

Table 4.4: Comparison between EGRET and LAT performances. From ??

range to overlap with the LAT energy range. The instruments are mounted in a way that let the observation of the whole sky be possible (see Fig.4.10). The NaI(Tl) detectors alone have a total FOV of ∼8 secterad while the BGO observes nearly the whole sky and the detectors are oriented in such way that the location of an event can be derived by comparing the count rates of each detector.

When a photon enters the instrument a signal is measured by a pulse height analyzer. The more energetic the photon, the higher the signal produced, hence the height of the signal is measured and it is converted into 128-channel resolution and 8-channel resolution. The first kind of data is called CSPEC, the produced lightcurves have a cadence of 4.092 sec in *idle* mode and 1.024 in *triggered* mode, while for the second kind of data, called (CTIME), the cadence is 0.256 sec in *idle* mode and 0.064 sec in *trigger* mode.

thus avoiding both deterioration and exhaustion of supply and increasing the instrument lifetime relative to CGRO. The instrument triggers when at least two of the twelve detectors measure an excess over a threshold, specified in units of standard deviation above the background. The background is computed in the 50 keV - 300 keV range over the previous 1.024 seconds and the standard threshold is set at 4.5σ above the background.

4.3.2.1 GBM energetic pileup

When a photon enters the instrument a pulse is generated (Fig.4.11), the height of which depends on the incident photon's energy, calibrated within an interval.

Since the deadtime of the instrument is 2.6μs and the time needed to the pulse shape to recover from the counting is 4μs, if the flux of particle is such that two photons enters the instrument with a delay less than the recovering time, the generated signal will be distorted resulting in an error in the counting process. Chaplin et al. [2013] show that different distortions can be produced (Fig.4.12 and Fig.4.13). In particular, the effect shown in Fig.4.13 (panel *a*) is relative to the event in which two photons with the same energy enter the detector almost simultaneously: the result is that they are counted as a single photon with twice the energy. This more seriously impacts the low energy channels in all
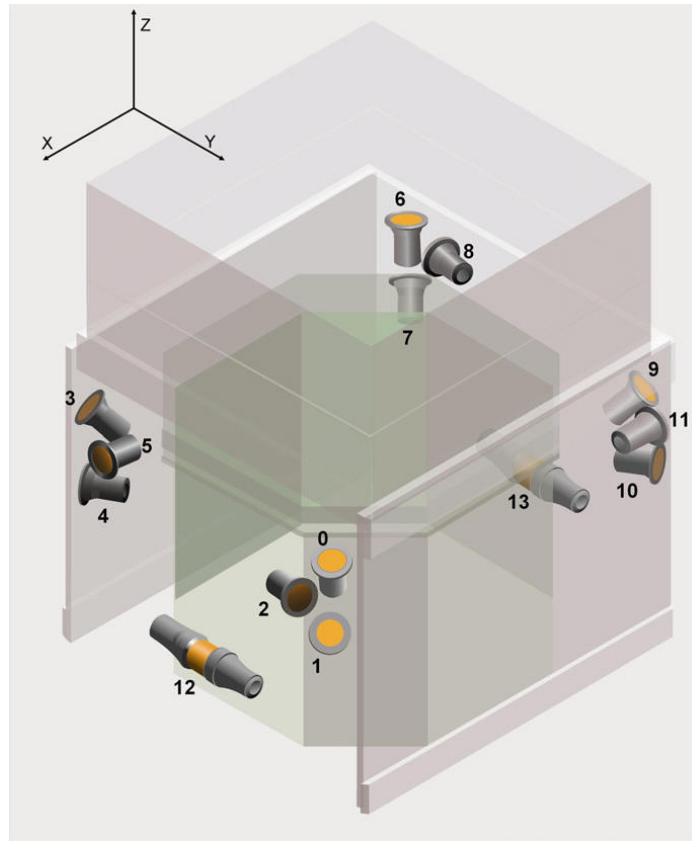
Figure 4.10: Schematic of the position of the 14 elements composing the *GBM* instrument. The NaI detectors are labeled from 0 to 11. BGO are labeled with 12 and 13. From Meegan et al. [2009]

Quantity	BATSE	*GBM*
	Large Area Detectors	**Low-energy Detectors**
Detectors	8 NaI(Tl)	12 NaI(Tl)
Area	2025 cm^2	126 cm^2
Thickness	1.27cm	1.27cm
Energy Range	25 keV to 1.8MeV	4 keV to 2MeV
	Spectroscopy Detectors	**High-energy Detectors**
Detector	8 NaI(Tl)	2 BGO
Area	126 cm^2	126 cm^2
Thickness	7.62cm	12.7cm
Energy Range	30 keV to 10MeV	150 keV to 30MeV

Table 4.5: Comparison between BATSE and *GBM* performances. From http://grbworkshop.wdfiles.com/local–files/s3-4-gbm-hands-on/vc_gbm_intro.pdf
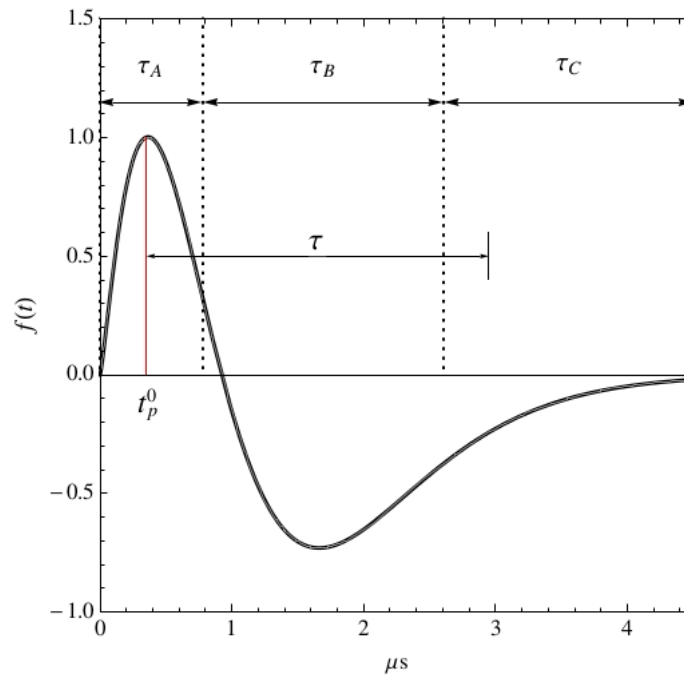
Figure 4.11: Pulse generated by a photon detected in one of the NaI(Tl) detectors. From Chaplin et al. [2013]

datasets used in this thesis.

4.3.2.2   GBM Data

The *GBM* data were obtained using the *ospex* tool in the SolarSoft package. It lets the user specify a flare event and download the raw data. The data are reduced (except the background removal) and displayed to the user. Two kinds of data are available: *i)* CSPEC, 128 energy channels, 4.096 sec/1.024 sec cadence in *idle/triggered* mode; *ii)* CTIME, 8 energy channels, 0.256 sec/0.064 sec cadence in *idle/triggered* mode.

The data can be analyzed within the tool or exported in IDL. When exported, the
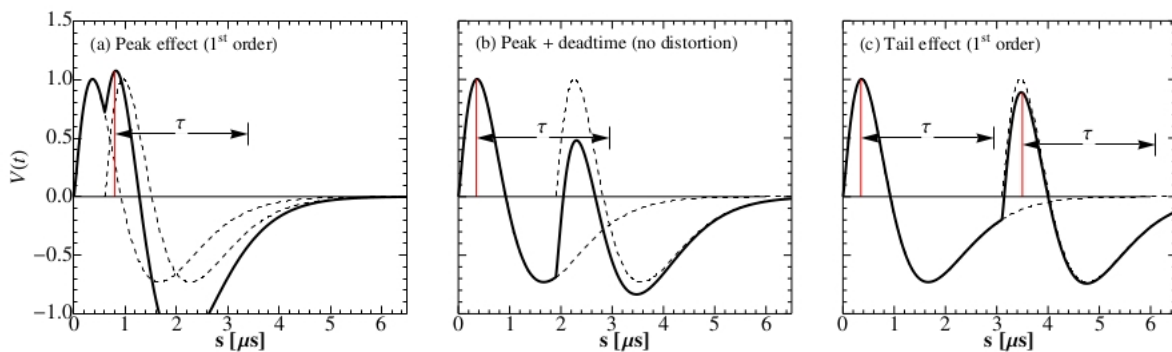
Figure 4.12: First order distorsion in the pulse. From Chaplin et al. [2013]
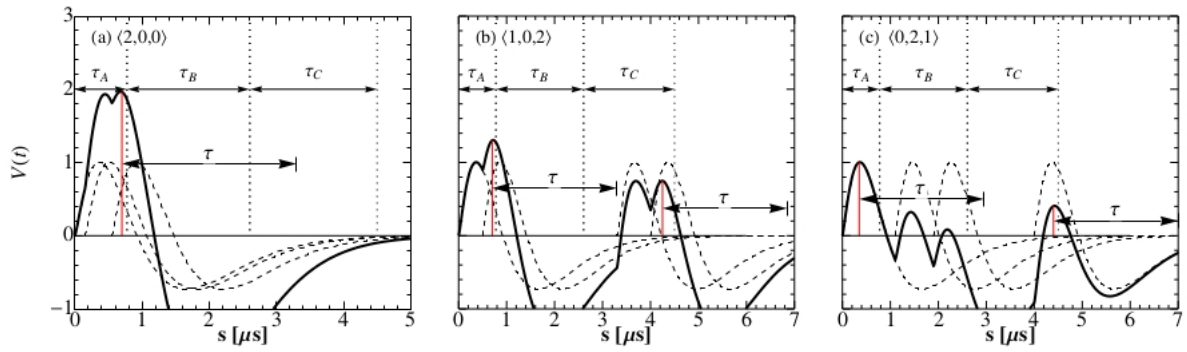
Figure 4.13: Second order distorsion in the pulse. From Chaplin et al. [2013]

lightcurves are subdivided in energy channels and are in units of "counts per timebin", and another vector is downloaded, containing the duration of each bin.

For this thesis, the raw data have been downloaded and the first step of the work has been the reproduction of the lightcurves already reduced by the tool, in order to be conscious of the reduction process.
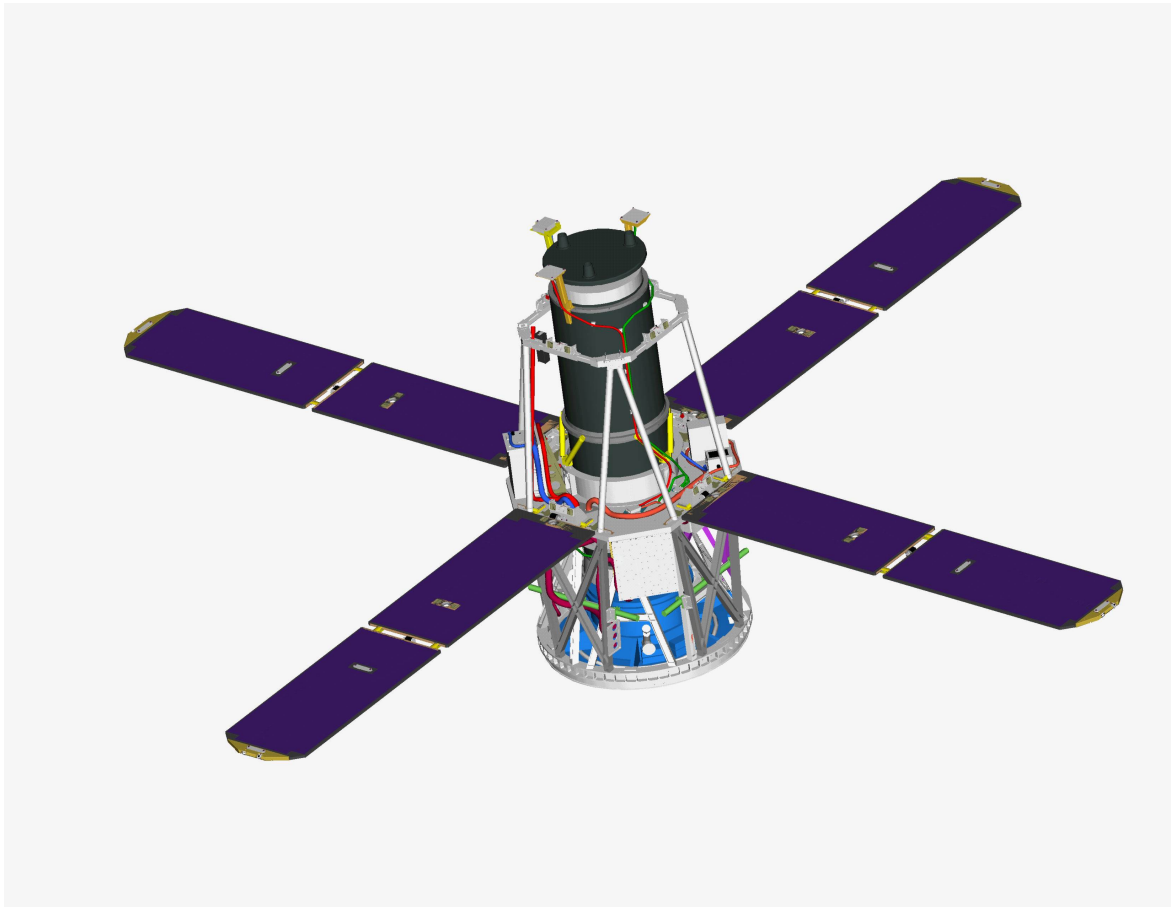
Figure   4.14:   A   model   of   the   *RHESSI*   satellite.   From:
http://hesperia.gsfc.nasa.gov/hessi/Hardware.htm

4.4   The Reuven Ramaty High Energy Solar Spectroscopic Imager (RHESSI)

The *RHESSI* satellite (Fig.4.14) is observing the Sun in the X-ray and γ-ray energy range
(Lin et al. [2002]). It was launched on 2002 Feb 05 from Cape Canaveral and it orbits the
Earth at an altitude of 600 km. The primary scientific objective of *RHESSI* is to understand
the processes involved in the particle acceleration during solar flares and it does so by doing
high resolution imaging spectroscopy observations. The imaging is accomplished using
nine Rotating Modulation Collimator (RMCs), consisting of a pair of separated grids that
rotates with the satellite. Behind each RMC there is a germanium detector with sensitivity
in the 3 keV - 17 MeV energy range. The whole system is mechanically cryocooled.

Since X-rays are unfocussed by the detectors, *RHESSI* uses a Fourier-transform imaging
system. Each collimator consists in a pair of widely separated grids that are planar arrays
of equally-spaced slats (opaque to the X-rays) separated by transparent slits (Fig.4.15). The
pitch of each pair of slits (marked with p in the figure) is identical and the slits are parallel,
so the transmission through the slit pair depends only on the direction of the incident
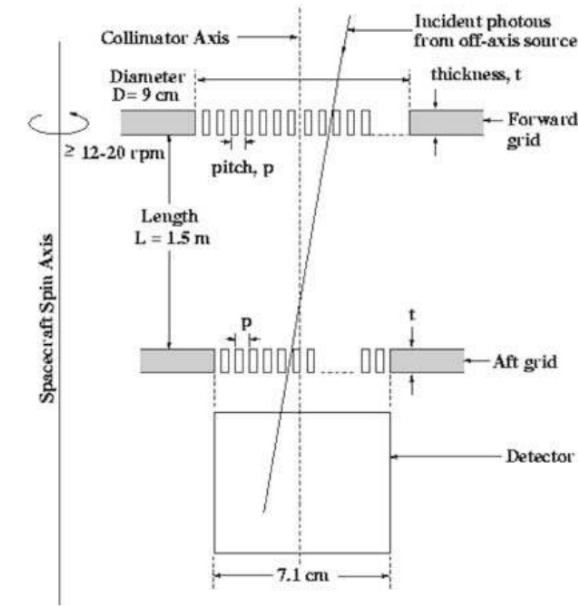
Figure 4.15: The *RHESSI* imaging system. From Lin et al. [2002].

photon. Calling L the distance between the two grids, we observe that the signal from a source is modulated form zero, to a maximum, and back to zero when the angle between the source and the collimator axis (hence the satellite axis) changes of an angle p/L so the angular resolution is $p/2L$.

The modulation of the transmission through the grid of the photons emitted from the source is achieved by the rotation of the whole satellite; then the detectors behind the collimator register the single photon energy and arrival time so that the counting rate is determined as a function of the rotation angle. Fig.4.16 shows the signal from a source located in different places of the solar disk as it is received by the detector. The amplitude of the signal is proportional to the intensity of the source, the angle with the solar equator is defined by the phase of the signal and the displacement along the radius changes its frequency.

The pitch of the grids ranges from $p=34\mu$m to $p=2.75$mm and the provided angular resolution goes from 2.3arcsec to $\sim$3arcmin which allows the satellite to image the sources over differents angular scales. The satellite measures 1100 Fourier components every half rotation (which lasts 2 sec). For comparison, the Yohkoh HXT instrument (used by Masuda et al. [1994] for their observation) could measure only 32 Fourier components, so the *RHESSI* satellite produces observations that far higher resolution. Tab.4.6 summarizes the characteristics of the satellite.
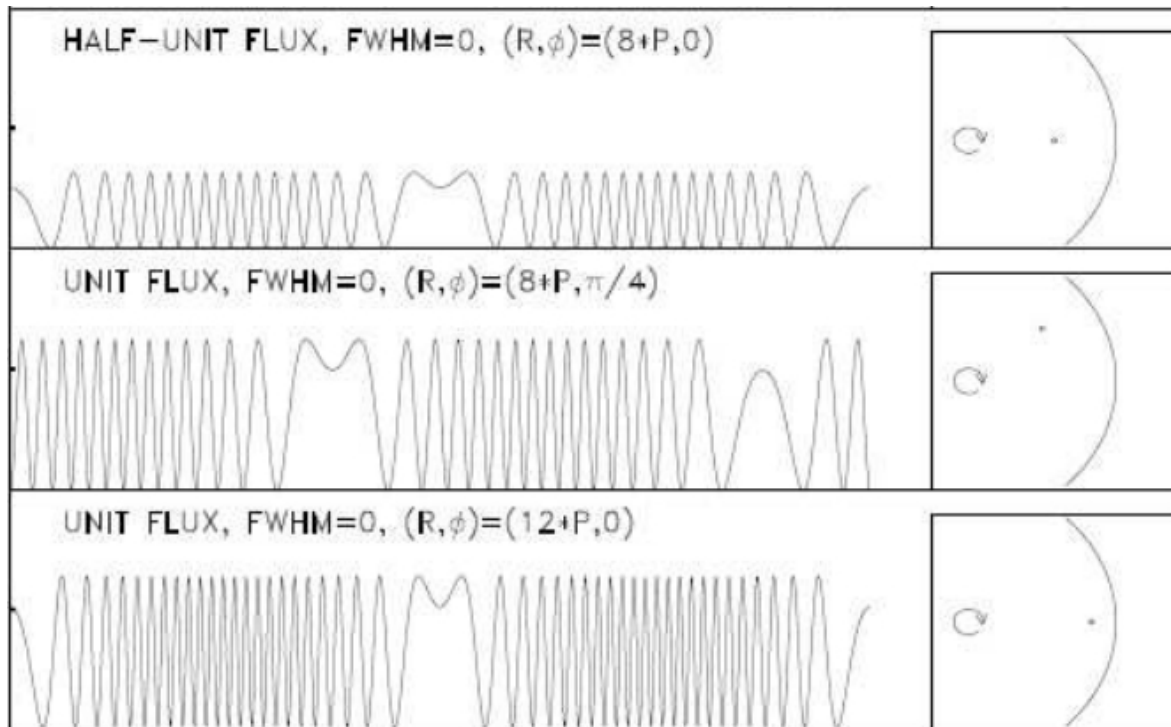
Figure 4.16: An example of the signal acquired from the detectors along one rotation period. Top panel shows a standard signal from a source; the middle panel shows the signal from the a source with twice the power and displaced by a 45°angle (the phase changes); bottom panel shows the signal from the same source but now it is displaced along the radial coordinate (the modulation frequency changes). From http://www.astro.gla.ac.uk/solaire/RHESSI_MATERIAL/rhessi_imaging.pdf

Characteristic	
Energy range	3 keV - 17 Mev
Energy resolution (FWHM)	$\leq$1 keV at 3 keV, down to $\sim$5 keV at 5MeV
Angular resolution	2.3arcsec to 100 keV, 7arcsec to 400 keV
Temporal resolution	2 sec for detailed image
Field of view	$\sim$1°
Detectors	9 germanium detectors (7.1cm dia. x 8.5cm) cooled to $\sim$75K
Imager grids	9 pairs, pitches from 34μm to 2.75mm
Grids separation	1.55m

Table 4.6: RHESSI characteristics.

Appendix A

IDL Code

A.1   aac_sdolightcurve.pro

```
function aac_sdolightcurve ,  list ,  window,path=path ,width ,timeframesec ,$
points=points ,gauss=gauss ,smooth=smooth, silent=silent ,motion=motion ,$
r_sun=r_sun ,region=region


;——————————————————————————————————————————————————————————————————————————
;PURPOSE: this procedure let you compute the lightcurve of each
;resolved element in a SDO/AIA set of observations. The most important
;thing is that the procedure follows the rotation of the Sun during
;the observation and corrects the position from which it takes the
;lightcurve accordingly .
;It is interactive by default: when you call the procedure , it opens a
;window displaying the first frame of the observation and asks you to
;click on the region of the Sun you want the lightcurve from.
;If the POINTS keyword is used , it skips the interactive part and
;calculates the lightcurve for each specified point, returning an
;array of lightcurves , one for each point.
;When it computes the lightcurve , you can choose to smooth the data
;before the integration , either with a box function or with a gaussian function .
;If the REGION keyword is set , this procedure
;produces a composit image overimposing the selected region of each
;frame one on the other .
;
;
;LIST: put here the list of the frame of the band you want the
;       lightcurve for .
;WINDOW: is the number of the window in which the program will plot
;         the image used to select the point of which you want the
;         lightcurve for (note that you can even choose 0, but I
;         suggest at least 1!).
```

115

```
;PATH: is the path in which the fits of each frame are.
;WIDTH: the number of pixels around the point over which the
;         lightcurve will be integrated: if you set width=n, the value
;         of the lightcurve at each frame will be the total of the box
;         given by [x-n:x+n,y-n:y+n].
;TIMEFRAMESEC= is the time vector of each band. It can be produced by
;             the procedure aac_timeframesec.pro.
;             Example: timeframesec1600=aac_timeframesec(list1600 [,path])
;POINTS= if set, the procedure skip the interactive part in which you
;         select the point on the surface. Instead, it calculates the
;         lightcurve of each point specified using this format:
;         points=[[x1,y1],[x2,y2], ... ,[xn, yn]]
;         Then it returns an array containing all the lightcurves.
;GAUSS= set it to smooth the surface with a gaussian. If set, you will
;         be asked to type the sigma of the gaussian in unit of pixels (i.e.if
;         you type 3, the sigma will be three pixels).
;SMOOTH= the same as GAUSS but the smoothing will be done using a
;         boxcar function instead of a gaussian.
;SILENT= set it if you want the minimum of the output printed on screen.
;MOTION= set it if you want the x_position printed at each frame.
;R_SUN= set it to tell the procedure which is the radius of the sun in
;         pixel unit. Default is 1590.
;REGION= settin this keyword will not produce a lightcurve. Instead
;         the procedure will create a image which is the sum of each frame. The
;         image will have the dimensions [2*width+1,2*width+1].
;
;
;EXAMPLE: lc=aac_sdolightcurve(list171,0,path='/home/data/',1,time171,/gauss)
;
;         In this case the procedure will be in interactive mode, will
;         integrate in a 3x3 box around the selected point, performing
;         a gauss smoothing and you'll be asked for the sigma of the
;         gaussian kernel.
;────────────────────────────────────────────────────────────────────────
```

```
;────────────────────────────────────────────────────────────────────────
```

```
;Coefficients of the equation which describes the differential motion of
;the surface of the Sun with latitude:
```

```
urad=0.000004848137D
a=0.6134D*urad
b=-0.099833333d*urad
c=-0.074458333d*urad
;───────────────────────────────────────────────────────────────────────

;Opening the first frame and checking the keywords:
;frame=mrdfits(strcompress( string(path) +list(0),/remove_all),0,h,/silent)
frame=mrdfits(path+list[0],0,h,/silent)
result=keyword_set(points)
gauss=keyword_set(gauss)
smooth=keyword_set(smooth)
silent=keyword_set(silent)
k_motion=keyword_set(motion)
k_r_sun=keyword_set(r_sun)
k_region=keyword_set(region)
k_suncoord=keyword_set(suncoord)


;─────────────────────────CREATING THE GAUSSIAN FUNCTION FOR CONVOLUTION─────────
if (gauss eq 1) then begin


    g_temp=dblarr(201,201)
    print , 'Type_the_sigma_of_the_gaussian_function:'
    read , sig
    mean=(n_elements(g_temp(*,0)-1))/2
    for i=0,200 do begin
        for j=0,200 do begin
            g_temp(i,j)=(1./sig)*(1./sqrt(2.*!pi))*exp(-(((i-mean)^2)/(2.*(sig)^2)$
)) * (1./sig)*(1./sqrt(2.*!pi))*exp(-(((j-mean)^2)/(2.*(sig)^2)))

        endfor
    endfor
    g=dblarr(n_elements(where(g_temp(100,*) gt 0.00009)),$
n_elements(where(g_temp(*,100) gt 0.00009)))
    g=g_temp[100-(n_elements(g(0,*))-1)/2:100+(n_elements(g(*,0))-1)/2,100-$
(n_elements(g(*,0))-1)/2:100+(n_elements(g(*,0))-1)/2]


endif
;───────────────────────────────────────────────────────────────────────


;─────────────────────────CREATION OF THE BOX FUNCTION FOR CONVOLUTION───────────
if (smooth eq 1) then begin
    print , 'Type_the_dimension_of_the_side_of_the_box:'
    read , dim
```

```
   box=dblarr(dim, dim)
   box[0:dim−1,0:dim−1]=1
   box=box/total(box)
endif
;————————————————————————————————————————————————————————————

;——Checks whether the keyword 'points' has been set. If not, it opens a
;new window for the interactive mode:——————————————————————————

if (result eq 0) then begin
   window,window, xsize=1000, ysize=750

   if (min(frame) eq −2147483648) then begin   ;this it is needed in order to
      frame[where(frame lt −2000)]=−2000        ;display the BLOS images, otherwise
      frame[where(frame gt 2000)]=2000          ;they will not be visible because
                                                ;of scaling.
   endif

   cgcontour, frame, nlevel=255,/fill ,background='black', color='white',$
position =[0.05,0.05,0.95,0.95]

   print, 'Click␣on␣the␣pixel␣you␣want␣the␣lightcurve␣for:'
   xycursor, x,y
   print, x,y

   if k_r_sun eq 0 then begin                   ;this let you choose whether to
                                                ;use the radius of 1590 pixel or
      r_sun=1590.                               ;the radius specified in the
                                                ;header of the fits file.
   endif else begin                             ;The value of 1590 seems to me to
                                                ;be the most reliable in tracking
                                                ;the points.
      r_sun=sxpar(h,'r_sun')
   endelse

   crpix1=sxpar(h,'crpix1')
   crpix2=sxpar(h,'crpix2')
   x_cen=x−crpix1                               ;distanza del punto prescelto dall'
                                                ;asse y passante per il centro del sole

   if k_suncoord eq 1 then print, 'X␣position␣relative␣to␣the␣center␣of␣the$
␣Sun:'+x_cen
   y_cen=y−crpix2                               ;distanza del punto prescelto dall'
                                                ;asse x passante per il centro del sole
```

```
   if k_suncoord eq 1 then print , 'Y_position_relative_to_the_center_of_the$
_Sun:'+y_cen


   limb_cen=−sqrt(r_sun^2. − y_cen^2.)  ;distanza del limb (all'altezza del punto
                                         ;) dall'asse x passante per il
                                         ;centro del sole (NEGATIVO PERCH DEVE
                                         ;ESSERE NEL SECONDO QUADRANTE)


    limb_ref=crpix1+limb_cen                 ;coordinata x del limb nel sistema di
                                             ;riferimento del frame


   print , 'The_coordinates_of_the_limb_are:' + string(limb_ref) + string(y)


   latitude=asin(y_cen/r_sun)
   omega=a + b∗(latitude)^2. + c∗(latitude)^4.
   t_0=(acos((x_cen)/(limb_cen)))/omega


   if k_region eq 0 then begin
       lightcurve=dblarr(n_elements(list))
   endif else begin
       sumregion=dblarr(2∗width+1,2∗width+1)
   endelse


   for i=0,n_elements(list)−1 do begin


       frame=mrdfits(path+list[i],0,h,/silent)


       if (gauss eq 1) and (smooth eq 0) then begin


         dt=timeframesec(i)−timeframesec(0)
         x_position =((limb_cen)∗cos(−omega∗(t_0+dt)))+crpix1
         if k_motion eq 1 then print , i,x_position
         im=convolve(frame(x_position −40:x_position +40,y−40:y+40),g)
         if (silent eq 0) then begin
         print , 'I_am_convolving_with_a_gaussian ,_be_patient'
         endif
         lightcurve(i)=total(im(40−width:40+width,40−width:40+width))


       endif


       if (smooth eq 1) and (gauss eq 0) then begin


           dt=timeframesec(i)−timeframesec(0)
```

```
            x_position =((limb_cen)*cos(−omega*(t_0+dt)))+crpix1
            if k_motion eq 1 then print, i,x_position
            im=convolve(frame(x_position−40:x_position+40,y−40:y+40),box)
            if (silent eq 0) then begin
                print, 'I_am_convolving_with_a_box,_be_patient'
            endif
            lightcurve(i)=total(im(40−width:40+width,40−width:40+width))
        endif


        if (gauss eq 0) and (smooth eq 0) then begin
          dt=timeframesec(i)−timeframesec(0)
          x_position =((limb_cen)*cos(−omega*(t_0+dt)))+crpix1
          if k_motion eq 1 then print, i,x_position
          lightcurve(i)=total(frame[x_position−width:x_position+width,y−width:y+width])
        endif


        if (gauss eq 1) and (smooth eq 1) then begin
          print, 'You_cannot_use_smooth_and_gauss_at_the_same_time!'
          lightcurve=0
        endif


        if k_region eq 1 then begin
          dt=timeframesec(i)−timeframesec(0)
          x_position =((limb_cen)*cos(−omega*(t_0+dt)))+crpix1
          sumregion=sumregion+frame[x_position−width:x_position+width,y−width:y+width]
        endif



      endfor

    print, 'And_the_last_x_position_is:' + string(x_position)

    if k_region eq 0 then begin
        return, lightcurve
    endif else begin
        return, sumregion
    endelse

;——————————————PART−ACTIVE−IF−YOU−HAVE−CHOOSEN−A−SET−OF−POINTS——————————————

endif else begin

    print, 'You_have_entered_a_list_of_points!_Wait_until_the_lightcurves_are$
_'calculated! Unless you have an extremely powerful computer, you better go $
```

```
 and have a coffee!'
    lightcurve=dblarr(n_elements(points(0,*)),n_elements(list))

if k_region eq 0 then begin
      lightcurve=dblarr(n_elements(points(0,*)),n_elements(list))
   endif else begin
      sumregion=dblarr(2*width+1,2*width+1)
   endelse

for j=0,n_elements(points(0,*))-1 do begin
   print,' '
   print,'I am calculating the lightcurve for the point:'+ $
string(points(0,j))+string(points(1,j))

   x=points[0,j]
   y=points[1,j]



   r_sun=1590.
   crpix1=sxpar(h,'crpix1')
   crpix2=sxpar(h,'crpix2')
   x_cen=x-crpix1                     ;distanza del punto prescelto dall'asse
                                      ;y passante per il centro del sole

  if k_suncoord eq 1 then print, 'X position relative to the center of the Sun:'+x_ce
  y_cen=y-crpix2                      ;distanza del punto prescelto dall'asse x pas
                                      ;sante per il centro del sole
  if k_suncoord eq 1 then print, 'Y position relative to the center of the Sun:'+y_ce

  limb_cen=-sqrt(r_sun^2. - y_cen^2.) ;distanza del limb (all'altezza del
                                      ;punto) dall'asse x passante per il
                                      ;centro del sole

  limb_ref=crpix1 + limb_cen          ;coordinata x del limb nel sistema di
                                      ;riferimento del frame

  print, 'The coordinates of the limb are:' + string(limb_ref) + string(y)


  latitude=asin(y_cen/r_sun)
  omega=a + b*(latitude)^2. + c*(latitude)^4.
  t_0=(acos((x_cen)/(limb_cen)))/omega
  for i=0,n_elements(list)-1 do begin
```

```
frame=mrdfits(path+list[i],0,h,/silent)
if (gauss eq 1) and (smooth eq 0) then begin

    dt=timeframesec(i)-timeframesec(0)
    x_position=((limb_cen)*cos(-omega*(t_0+dt)))+crpix1
    if k_motion eq 1 then print, i,x_position
    im=convolve(frame(x_position-40:x_position+40,y-40:y+40),g)
    if (silent eq 0) then begin
    print, 'I_am_convolving_with_a_gaussian,_be_patient'
    endif
    lightcurve(j,i)=total(im(40-width:40+width,40-width:40+width))

endif


  if (smooth eq 1) and (gauss eq 0) then begin

    dt=timeframesec(i)-timeframesec(0)
    x_position=((limb_cen)*cos(-omega*(t_0+dt)))+crpix1
    if k_motion eq 1 then print, i,x_position
    im=convolve(frame(x_position-40:x_position+40,y-40:y+40),box)
    if (silent eq 0) then begin
        print, 'I_am_convolving_with_a_box,_be_patient'
    endif
    lightcurve(j,i)=total(im(40-width:40+width,40-width:40+width))
  endif


  if (gauss eq 0) and (smooth eq 0) then begin
    dt=timeframesec(i)-timeframesec(0)
    x_position=((limb_cen)*cos(-omega*(t_0+dt)))+crpix1
    if k_motion eq 1 then print, i,x_position
    lightcurve(j,i)=total(frame[x_position-width:x_position+width,y-width:y+width]
  endif


  if (gauss eq 1) and (smooth eq 1) then begin
    print, 'You_asshole,_you_cannot_use_smooth_and_gauss_at_the_same_time!'
    lightcurve=0
  endif


  if k_region eq 1 then begin
    dt=timeframesec(i)-timeframesec(0)
    x_position=((limb_cen)*cos(-omega*(t_0+dt)))+crpix1
    sumregion=sumregion+frame[x_position-width:x_position+width,y-width:y+width]
  endif
```

```
;print , j , i
;print , x_position
    endfor
    print , 'The␣final␣position␣of␣the␣point␣is:'+ string(x_position) + string(y)


endfor

    if k_region eq 0 then begin
        return , lightcurve
    endif else begin
        return , sumregion
    endelse

ENDELSE

end
```

A.2   aac_comparison.pro

```
pro aac_comparison , time1=time1 , time2=time2 , time3=time3 , time4=time4 , time5=time5 , $
list1=list1 , list2=list2 , list3=list3 , list4=list4 , list5=list5 , path , plot_window , $
tv=tv , log=log , noclose=noclose , crop=crop ,mag=mag , silent=silent , noscale=noscale

;PURPOSE: this procedure let you click on a point in time of an
;already plotted lightcurve of a flare (any band , provided that the
;time vector is in seconds after midnight and it is relative to a SDO
;observation you hve saved on your harddrive) and show you the frame
;of the SDO observation at that time up to five different bands.
;
;
;TIME*= time vector relative to list* created using the procedure
;      "aac_timeframesec . pro"
;
;LIST*= a string array containing the list of the filenames of each
;      frame of the observation
;
;MAG= real number , is the magnification factor (you'll need it if you choose
;     a small crop area)
;
;NOCLOSE= keep the image window open , after you close the program
;
```

```
;
;CROP=[[x1,y1],[x2,y2]] where x1 and y1 are the coordinates of the
;       low−left point and x2 and y2 are the coordinates of the up−right
;       point defining the rectangle to crop.
;LOG= display the images in a logarithmic intensity.
;
;PATH= string containing the path where the frames of the observation
;        are located
;PLOT_WINDOW: the active window containing the already plotted lightcurve
;
;SILENT= does not print the time you've selected
;
;For istance, let's say you want to see the observation of two
;bands (1600 and 335) in logarithmic scale, already plotted in window
;3. You'll call the procedure as following:
;
;   aac_comparison, time1=time1600, list1=list1600, time2=time335,
;                   list2=list335, '/home/',3, /log
;
;When you want to close the procedure, just right−click on the
;lightcurve.
;
;DEPENDENCIES: aac_showframe.pro




noscale=keyword_set(noscale)
log=keyword_set(log)
noclose=keyword_set(noclose)
silent=keyword_set(silent)
key_crop=keyword_set(crop)
key_multilist=keyword_set(multilist)
key_mag=keyword_set(mag)
key_list1=keyword_set(list1)
key_list2=keyword_set(list2)
key_list3=keyword_set(list3)
key_list4=keyword_set(list4)
key_list5=keyword_set(list5)
key_time1=keyword_set(time1)
key_time2=keyword_set(time2)
key_time3=keyword_set(time3)
key_time4=keyword_set(time4)
key_time5=keyword_set(time5)
```

```
esc=0

frameshow=mrdfits ( path+list1 (0) ,0 ,hh,/ silent )

if (key_mag eq 0) then mag=1
if (key_crop eq 1) then begin
      crop=crop

   endif else begin
   crop =[[0 ,0] ,[ n_elements (frameshow (*,0)) −1 , n_elements (frameshow (0 ,*)) −1]]
endelse
```

```
;──────────CREATING THE STRING ARRAY FOR THE TITLES OF THE WINDOWS──────────
title_list=strarr (5)
if key_list1 eq 1 then begin
   temp=mrdfits ( path+list1 (0) ,0 ,h,/ silent )
   title_list (0)=sxpar (h, 'WAVE_STR')
endif
if key_list2 eq 1 then begin
   temp=mrdfits ( path+list2 (0) ,0 ,h,/ silent )
   title_list (1)=sxpar (h, 'WAVE_STR')
endif
if key_list3 eq 1 then begin
   temp=mrdfits ( path+list3 (0) ,0 ,h,/ silent )
   title_list (2)=sxpar (h, 'WAVE_STR')
endif
if key_list4 eq 1 then begin
   temp=mrdfits ( path+list4 (0) ,0 ,h,/ silent )
   title_list (3)=sxpar (h, 'WAVE_STR')
endif
if key_list5 eq 1 then begin
   temp=mrdfits ( path+list5 (0) ,0 ,h,/ silent )
   title_list (4)=sxpar (h, 'WAVE_STR')
endif
;──────────────────────────────────────────────────────────────────────────────

;──────OPEN THE CORRECT NUMBER OF WINDOWS WITH THE PROPER DIMENSIONS──────────
;──────AND TITLE────────────────────────────────────────────────────────────────

number_of_windows=total ( key_list1+key_list2+key_list3+key_list4+key_list5 )
print , number_of_windows
```

```
for i=0,number_of_windows−1 do begin
    index=i+1
    window, 30−i , xsize =(crop(0,1)−crop(0,0))∗mag,$
             ysize =(crop(1,1)−crop(1,0))∗mag, title ='list '+title_list(i)
    endfor
;————————————————————————————————————————————


;———————————SHOW THE FRAME———————————————————————————


repeat begin
    wset , plot_window
    cursor , x, y,/down
    if (!mouse.button eq 4) then esc=1
    if not esc then begin

if (key_list1 eq 1) then aac_showframe, time1, list1 ,x,path ,30 ,crop ,noscale ,$
log , silent ,mag
if (key_list2 eq 1) then aac_showframe, time2, list2 ,x,path ,29 ,crop ,noscale ,$
log , silent ,mag
if (key_list3 eq 1) then aac_showframe, time3, list3 ,x,path ,28 ,crop ,noscale ,$
log , silent ,mag
if (key_list4 eq 1) then aac_showframe, time4, list4 ,x,path ,27 ,crop ,noscale ,$
log , silent ,mag
if (key_list5 eq 1) then aac_showframe, time5, list5 ,x,path ,26 ,crop ,noscale ,$
log , silent ,mag

  endif
endrep until esc eq 1
;————————————————————————————————————————————


;—————————————————CLOSE THE WINDOWS———————————————————————
if (noclose eq 0) then begin
 for i=0,number_of_windows−1 do begin
    wdelete ,30−i
 endfor
endif
;————————————————————————————————————————————


end
```

A.3   aac_showframe.pro

```
pro aac_showframe , timeframesec , list ,x,path , w_number,crop ,noscale ,log , silent ,$
mag
```

```
;————————————————————————————————————————————————————————————————
;PURPOSE: this procedure is used by the procedure aac_comparison.pro
;to show the frame of the selected band at the time provided in the
;variable x.
;
;TIMEFRAMESEC= the time vector of the observation created by the
;procedure aac_timeframesec.pro
;
;LIST= a string array containing the ordered filenames of each frame
;of the observation
;
;X= the time in seconds after midnight of the wanted frame of the
;observation
;
;PATH= the path where the frames listed in LIST are
;
;W_NUMBER= the window in which you want the frame plotted
;
;CROP=[[x1,y1],[x2,y2]] where x1 and y1 are the coordinates of the
;       low-left point and x2 and y2 are the coordinates of the up-right
;       point defining the rectangle to crop.
;
;NOSCALE= plot the unscaled frame
;
;LOG= plot the frame in logarithmic scale
;
;SILENT= the procedure will not plot any information
;
;MAG= the magnification factor for the frame plotted
;
;
;————————————————————————————————————————————————————————————————


if (mag eq 0) then mag=1

k=where(timeframesec ge x)
    ;window, 30,xsize=1000,ysize=750
    if noscale eq 1 then begin

        frameshow=mrdfits(path+list(k(0)),0,hh,/silent)
        wset,w_number
        if (log eq 1) then begin
            tv,alog(congrid(frameshow(crop(0,0):crop(0,1),crop(1,0):crop(1,1))>10$
```

```
<16000,(crop(0,1)−crop(0,0))*mag,(crop(1,1)−crop(1,0))*mag))
            endif else begin
        tv,congrid(frameshow(crop(0,0):crop(0,1),crop(1,0):crop(1,1)),(crop(0,1)−$
crop(0,0))*mag,(crop(1,1)−crop(1,0))*mag)
      ;tv, frameshow
           endelse
      if (silent eq 0) then print, 'the_time_you_have_choosen_is '+string(x)
      if (silent eq 0) then print, 'the_time_of_the_frame_is '+$
string(timeframesec(k(0)))


        endif else begin
          frameshow=mrdfits(path+list(k(0)),0,hh,/silent)
          wset,w_number
          if (log eq 1) then begin
           tvscl,alog(congrid(frameshow(crop(0,0):crop(0,1),crop(1,0):crop(1,1))$
>10<16000,(crop(0,1)−crop(0,0))*mag,(crop(1,1)−crop(1,0))*mag))

           endif else begin
        tvscl,congrid(frameshow(crop(0,0):crop(0,1),crop(1,0):crop(1,1)),$
(crop(0,1)−crop(0,0))*mag,(crop(1,1)−crop(1,0))*mag)
          ;print, 'puppa'
       endelse

;tvscl, frameshow
          if (silent eq 0) then print, 'the_time_you_have_choosen_is '+string(x)
          if (silent eq 0) then print, 'the_time_of_the_frame_is '+$
string(timeframesec(k(0)))
       endelse
end
```

A.4   aac_corr.pro

```
function aac_corr,lc1, lc2,gauss_smooth1,gauss_smooth2, $
gauss_trend1=gauss_trend1,gauss_trend2=gauss_trend2,crosstime=crosstime,$
matrix=matrix


;——————————————————————————————————————————————————————————————————————
;PURPOSE: this procedure let you perform the crosscorrelation between
;two lightcurve. It let you smooth each lightcurve using the
;"gaussian smoothing" and let you compute the crosscorrelation of the
;"detrended" lightcurve, i.e. lightcurves from which their trend has
;been subtracted. The trend is computed convolving a wide gaussian
;with the lightcurve. It also let you automatically compute the
```

```
;crosscorrelation between a dataset (for istance, NoRP dataset is
;composed by seven lightcurve).

;
;LC1= lightcurve you want to crosscorrelate
;
;LC2= same as LC1
;
;GAUSS_SMOOTH1= the "sigma" of the gaussian used to smooth the LC1
;
;GAUSS_SMOOTH2= same as GAUSS_SMOOTH1
;
;GAUSS_TREND1= the width of the gaussian to convolve with LC1 to
;create the trend
;
;GAUSS_TREND2= same as GAUSS_TREND1
;
;CROSSTIME= it is the time vector used to crosscorrelate the
;lightcurves. If not provided, the procedure will compute it as
;"crosstime=findgen(n_elements(lc1)*2-1)-n_elements(lc1)+1"
;
;MATRIX= if set, the procedures performs the crosscorrelation of a
;whole dataset, returning a matrix where the coefficient (i,j) is the
;shift between the lightcurves that gives the maximum
;crosscorrelation. In this case both LC1 and LC2 have to contain the
;same dataset.
;————————————————————————————————————————————————————————————————————

if keyword_set(matrix) eq 0 then begin
 if keyword_set(crosstime) eq 0 then $
crosstime=findgen(n_elements(lc1)*2-1)-n_elements(lc1)+1


  print, n_elements(lc1)
  print, n_elements(crosstime)

  if keyword_set(gauss_trend1) eq 0 then begin

    ppp=c_correlate(aac_pm(gauss_smooth(lc1,gauss_smooth1,/nan,/edge_zero)),$
aac_pm(gauss_smooth(lc2,gauss_smooth2,/nan,/edge_zero)),crosstime)

  endif else begin

    ppp=c_correlate(aac_pm(gauss_smooth(lc1,gauss_smooth1,/nan,/edge_zero)-$
```

```
aac_gauss_smooth(lc1,gauss_trend1,/nan,/edge_zero)),$
aac_pm(gauss_smooth(lc2,gauss_smooth2,/nan,/edge_zero)-$
aac_gauss_smooth(lc2,gauss_trend2,/nan,/edge_zero)),crosstime)

   endelse


   puppa=max(ppp)
   print, puppa,crosstime(!c)
;the system variable !C is set to the one-dimensional subscript of the
;maximum element

   return, ppp

endif else begin

size_lc1=size(lc1)
size_lc2=size(lc2)
crosstime=findgen(size_lc1(2)*2-1)-size_lc1(2)+1
help, crosstime
print, size_lc1(2)
ccm=dblarr(size_lc1(1),size_lc2(1))

for i=0,size_lc1(1)-1 do begin
   for j=0,size_lc2(1)-1 do begin
      ppp=c_correlate(aac_pm(gauss_smooth(lc1(i,*),gauss_smooth1,/nan,$
/edge_zero)),aac_pm(gauss_smooth(lc2(j,*),gauss_smooth2,/nan,/edge_zero)),$
crosstime)
      puppa=max(ppp)
      ccm(i,j)=crosstime(!c) ;the system variable !C is set to the
;one-dimensional subscript of the maximum element
      print, i,j
   endfor
endfor

endelse
return, ccm




end
```

A.5   aac_timeframesec.pro

function aac_timeframesec , list ,path=path

```
;——————————————————————————————————————————————
;PURPOSE: given a SDO dataset this procedure let you create the time
;vector associated to the observation by reading the DATE–OBS keyword
;from the header of each frame and transforming it in "seconds after
;midnight".
;
;LIST: a string array containing the ordered filenames of each frame
;of the observation
;
;PATH= the path where the frames listed in LIST are
;
;——————————————————————————————————————————————

if keyword_set(path) eq 0 then path=''
timeobs=strarr(n_elements(list))

for i=0,n_elements(list)−1 do begin
   frame=mrdfits(path+list(i),0,h,/silent)
   timeobs(i)=sxpar(h,'DATE–OBS')
ENDFOR

timeframesec=dblarr(n_elements(list))

for i=0,n_elements(list)−1 do begin
   result=strsplit(timeobs(i),'T',/extract)
   result1=strsplit(result(1),':',/extract)
   result1db=double(result1)
   timeframesec(i)=result1db(2) + result1db(1)*60. + result1db(0)*60.*60.
endfor

return , timeframesec

end
```

A.6   aac_xsdo.pro

function aac_xsdo , header
```
;——————————————————————————————————————————————
;PURPOSE: This function returns the calibrate x coordinate for SDO images given
;the header of the image.
```

```
;
;HEADER= a string array containing the header of the array.
;
;***IT WORKS WITH ANY IMAGE FROM ANY OBSERVATORY READ USING THE
;PROCEDURE mrdfits.pro ,PROVIDED ITS HEADER CONTAINS THE FOLLOWING KEYWORD:
;
;−NAXIS1
;−CRPIX1
;−CDELT1
;————————————————————————————————————————————————————————————————————
```

```
xvec=(findgen(sxpar(header, 'naxis1'))−sxpar(header,'crpix1'))*sxpar(header,$
'cdelt1')
print, sxpar(header, 'naxis1')
print, sxpar(header,'crpix1')
print, sxpar(header,'cdelt1')

return, xvec
end
```

A.7   aac_ysdo.pro

```
function aac_ysdo, header
```

```
;————————————————————————————————————————————————————————————————————
;PURPOSE: This function returns the calibrate x coordinate for SDO images given
;the header of the image.
;
;HEADER= a string array containing the header of the array.
;
;***IT WORKS WITH ANY IMAGE FROM ANY OBSERVATORY READ USING THE
;PROCEDURE mrdfits.pro ,PROVIDED ITS HEADER CONTAINS THE FOLLOWING KEYWORD:
;
;−NAXIS2
;−CRPIX2
;−CDELT2
;————————————————————————————————————————————————————————————————————
```

```
yvec=(findgen(sxpar(header, 'naxis2'))−sxpar(header,'crpix2'))*sxpar(header,'cdelt2')

return, yvec
```

end

A.8 aac_pm.pro

```
function aac_pm, vec

;PURPOSE: this function gives back a vector normalized to its maximum value.


pippo=vec/max(vec)

return, pippo

end
```

A.9 aac_nanremover.pro

```
function aac_nanremover, vec, print=print, width=width


;————————————————————————————————————————————————————————————
;PURPOSE: this procedure let you remove the NaN occurrences in a
;vector. When it finds a NaN, it computes the mean in a box having a
;with equal to the value specifiedin the keyword WIDTH (default is
;10).
;
;set PRINT to print the info
;set WIDTH=n to set the 2n+1 interval centered on the NaN-point over
;which the mean will be calculated (default WIDTH=10)
;————————————————————————————————————————————————————————————
k_width=keyword_set(width)
k_print=keyword_set(print)

if k_width eq 0 then width=10

if k_print eq 1 then print, 'At the beginning of the process the number of NaN$
 in the vector is:', total(finite(vec,/nan))

for i=double(width),double(n_elements(vec)-width-1) do begin
   if finite(vec(i)) eq 0 then begin
      vec(i)=mean(vec(i-width:i+width),/nan)
      if k_print eq 1 then print, i
   endif
endfor
```

if k_print **eq** 1 **then** **print** ,'At␣the␣end␣of␣the␣process␣the␣number␣of␣NaN$
␣in␣the␣vector␣is:', total(finite(vec,/nan))

return ,vec

end

A.10 aac_frameshow.pro

pro aac_frameshow, list ,path=path, first=first , last=last , lowleft=lowleft ,$
upright=upright , scale=scale , delay=delay ,min=min,max=max,exptime=exptime ,log=log

```
;PURPOSE: this procedure let you see a video of the SDO observation
;selected .
;
;LIST= a string array containing the ordered filenames of each frame
;of the observation
;
;PATH= the path where the frames listed in LIST are
;
;FIRST= the index of the LIST vector relative to the frame you want
;the video starts from
;
;LAST=the index of the LIST vector relative to the frame you want
;the video stops at
;
;LOWLEFT= if you want to zoom in the video , this is the low−left
;corner of the box of the selected region
;
;UPRIGHT=  if you want to zoom in the video , this is the low−left
;corner of the box of the selected region
;
;SCALE= it normalizes each pixel of the frame in the range [0 ,255]
;
;DELAY= set the delay between one frame and the following one
;
;MIN/MAX= if you set it , each pixel of the image with a value lower
;than MIN will be set to 0, and each pixel of the image with a value
;higher than MAX will be set to MAX.
;
;EXPTIME= divide each frame of the observation by the exposure time ,
;taken from the header of each frame .
;
;LOG= plot each frame in logarithmic scale .
```

```
k_first=keyword_set(first)
k_last=keyword_set(last)
k_lowleft=keyword_set(lowleft)
k_upright=keyword_set(upright)
k_scale=keyword_set(scale)
k_delay=keyword_set(delay)
k_min=keyword_set(min)
k_max=keyword_set(max)
k_exptime=keyword_set(exptime)
k_path=keyword_set(path)
k_log=keyword_set(log)

if k_path eq 0 then path=''

fshow=mrdfits(path+list(0),0,header,/silent)

if (k_first+k_last eq 1) then begin
   print, 'Both first and last have to be specified!'
   return
endif else begin
   if (k_last eq 0) then begin
      first=0
      last=n_elements(list)-1
   endif
endelse


if (k_lowleft+k_upright eq 1) then begin
   print, 'Both lowleft and upright have to be specified!'
   return
endif else begin
   if (k_upright eq 0) then begin
      lowleft=[0,0]
      upright=[n_elements(fshow(*,0))-1,n_elements(fshow(0,*))-1]
   endif
endelse

if (k_log eq 0) then begin

if (k_delay eq 0) then delay=0
print, k_min
```

```
print , k_max
if (k_min+k_max eq 2) then begin

for i=first ,last do begin
   fshow=mrdfits(path+list(i),0,header,/silent)
   if k_exptime eq 1 then fshow=fshow/sxpar(header,'exptime')
   if (k_scale eq 1) then tvscl , congrid(fshow(lowleft(0):upright(0),$
lowleft(1):upright(1))>min<max,800,700) else tv , $
congrid(fshow(lowleft(0):upright(0),lowleft(1):upright(1))>min<max,800,700)
   wait , delay
endfor

endif else begin

   for i=first ,last do begin
   fshow=mrdfits(path+list(i),0,header,/silent)
   if k_exptime eq 1 then fshow=fshow/sxpar(header,'exptime')
   if (k_scale eq 1) then tvscl , congrid(fshow(lowleft(0):upright(0),$
lowleft(1):upright(1)),800,700) else tv , $
congrid(fshow(lowleft(0):upright(0),lowleft(1):upright(1)),800,700)
   wait , delay
endfor
endelse

;————————————————————————————————————————————————————————————————

endif else begin

if (k_delay eq 0) then delay=0
print , k_min
print , k_max
if (k_min+k_max eq 2) then begin

for i=first ,last do begin
   fshow=mrdfits(path+list(i),0,header,/silent)
   if k_exptime eq 1 then fshow=fshow/sxpar(header,'exptime')
   if (k_scale eq 1) then tvscl , alog(congrid(fshow(lowleft(0):upright(0),$
lowleft(1):upright(1)),800,700)>min<max) else tv ,$
alog(congrid(fshow(lowleft(0):upright(0),lowleft(1):upright(1)),800,700)>min$
<max)
   wait , delay
endfor

endif else begin
```

```idl
    for i=first ,last do begin
    fshow=mrdfits(path+list(i),0,header,/silent)
    if k_exptime eq 1 then fshow=fshow/sxpar(header,'exptime')
    if (k_scale eq 1) then tvscl, alog(congrid(fshow(lowleft(0):upright(0),$
lowleft(1):upright(1)),800,700)) else tv, $
alog(congrid(fshow(lowleft(0):upright(0),lowleft(1):upright(1)),800,700))
    wait, delay
endfor
endelse

endelse


end
```

Bibliography

Solar Data Analysis Center (SDAC) website. URL `http://umbra.nascom.nasa.gov/index.html/`.

Nobeyama Radio Heliograph, a. URL `http://solar.nro.nao.ac.jp/norh/`.

Nobeyama Radio Polarimeter, b. URL `http://solar.nro.nao.ac.jp/norp/`.

Solad Dynamics Observatory website. URL `http://sdo.gsfc.nasa.gov/`.

M. Ackermann et al. High-energy Gamma-Ray Emission from Solar Flares: Summary of Fermi Large Area Telescope Detections and Analysis of Two M-class Flares. *Astrophys. J.*, 787:15, May 2014. doi: 10.1088/0004-637X/787/1/15.

M. J. Aschwanden. Particle acceleration and kinematics in solar flares - A Synthesis of Recent Observations and Theoretical Concepts (Invited Review). *Space Sci. Rev.*, 101:1–227, January 2002. doi: 10.1023/A:1019712124366.

M. J. Aschwanden and R. A. Schwartz. The Inversion of Electron Time-of-Flight Distances from Hard X-Ray Time Delay Measurements. *Astrophys. J.*, 464:974, June 1996. doi: 10.1086/177385.

M. J. Aschwanden, L. Fletcher, C. J. Schrijver, and D. Alexander. Coronal Loop Oscillations Observed with the Transition Region and Coronal Explorer. *Astrophys. J.*, 520:880–894, August 1999. doi: 10.1086/307502.

W. B. Atwood, A. A. Abdo, M. Ackermann, W. Althouse, B. Anderson, M. Axelsson, L. Baldini, J. Ballet, D. L. Band, G. Barbiellini, and et al. The Large Area Telescope on the Fermi Gamma-Ray Space Telescope Mission. *Astrophys. J.*, 697:1071–1102, June 2009. doi: 10.1088/0004-637X/697/2/1071.

L. A. Balona, A.-M. Broomhall, A. Kosovichev, V. M. Nakariakov, C. E. Pugh, and T. Van Doorsselaere. Oscillations in stellar superflares. *Mon. Not. Roy. Astron. Soc.*, 450:956–966, June 2015. doi: 10.1093/mnras/stv661.

T. S. Bastian, A. O. Benz, and D. E. Gary. Radio Emission from Solar Flares. *Ann. Rev. Astron. Astroph.*, 36:131–188, 1998. doi: 10.1146/annurev.astro.36.1.131.

J. Birn and E. R. Priest. *Reconnection of Magnetic Fields*. Cambridge University Press, 2007.

V. Chaplin, N. Bhat, M. S. Briggs, and V. Connaughton. Analytical modeling of pulse-pileup distortion using the true pulse shape; applications to Fermi-GBM. *Nuclear Instruments and Methods in Physics Research A*, 717:21–36, July 2013. doi: 10.1016/j.nima.2013.03.067.

M. E. Cornell, G. J. Hurford, A. L. Kiplinger, and B. R. Dennis. The relative timing of microwaves and hard X-rays in solar flares. *Astrophys. J.*, 279:875–881, April 1984a. doi: 10.1086/161958.

M. E. Cornell, G. J. Hurford, A. L. Kiplinger, and B. R. Dennis. The relative timing of microwaves and hard X-rays in solar flares. *Astrophys. J.*, 279:875–881, April 1984b. doi: 10.1086/161958.

L. Dolla, C. Marqué, D. B. Seaton, T. Van Doorsselaere, M. Dominique, D. Berghmans, C. Cabanas, A. De Groof, W. Schmutz, A. Verdini, M. J. West, J. Zender, and A. N. Zhukov. Time Delays in Quasi-periodic Pulsations Observed during the X2.2 Solar Flare on 2011 February 15. *Astrophys. J. Lett.*, 749:L16, April 2012. doi: 10.1088/2041-8205/749/1/L16.

D. Gruber, P. Lachowicz, E. Bissaldi, M. S. Briggs, V. Connaughton, J. Greiner, A. J. van der Horst, G. Kanbach, A. Rau, P. N. Bhat, R. Diehl, A. von Kienlin, R. M. Kippen, C. A. Meegan, W. S. Paciesas, R. D. Preece, and C. Wilson-Hodge. Quasi-periodic pulsations in solar flares: new clues from the Fermi Gamma-Ray Burst Monitor. *Astron. Astrophys.*, 533:A61, September 2011. doi: 10.1051/0004-6361/201117077.

P. Kumar, D. E. Innes, and B. Inhester. Solar Dynamics Observatory/Atmospheric Imaging Assembly Observations of a Reflecting Longitudinal Wave in a Coronal Loop. *Astrophys. J. Lett.*, 779:L7, December 2013. doi: 10.1088/2041-8205/779/1/L7.

T. N. Larosa and R. L. Moore. A Mechanism for Bulk Energization in the Impulsive Phase of Solar Flares: MHD Turbulent Cascade. *Astrophys. J.*, 418:912, December 1993. doi: 10.1086/173448.

T. N. LaRosa and S. N. Shore. Production of Energy-dependent Time Delays in Impulsive Solar Flare Hard X-Ray Emission by Short-Duration Spectral Index Variations. *Astrophys. J.*, 503:429–434, August 1998. doi: 10.1086/305990.

T. N. Larosa, R. L. Moore, and S. N. Shore. A new path for the electron bulk energization in solar flares: Fermi acceleration by magnetohydrodynamic turbulence in reconnection outflows. *Astrophys. J.*, 425:856–860, April 1994. doi: 10.1086/174031.

C.-Y. Lee and H. Wang. Hard x-ray and Microwave Flux Spectra of the 2 November 1991 Solar Flare. *Sol. Phys.*, 195:149–164, July 2000. doi: 10.1023/A:1005221009632.

J. R. Lemen et al. The Atmospheric Imaging Assembly (AIA) on the Solar Dynamics Observatory (SDO). *Sol. Phys.*, 275:17–40, January 2012. doi: 10.1007/s11207-011-9776-8.

R. P. Lin et al. The Reuven Ramaty High-Energy Solar Spectroscopic Imager (RHESSI). *Sol. Phys.*, 210:3–32, November 2002. doi: 10.1023/A:1022428818870.

Y. Liu, J. T. Hoeksema, P. H. Scherrer, J. Schou, S. Couvidat, R. I. Bush, T. L. Duvall, K. Hayashi, X. Sun, and X. Zhao. Comparison of Line-of-Sight Magnetograms Taken by the Solar Dynamics Observatory/Helioseismic and Magnetic Imager and Solar and Heliospheric Observatory/Michelson Doppler Imager. *Sol. Phys.*, 279:295–316, July 2012. doi: 10.1007/s11207-012-9976-x.

E. T. Lu and V. Petrosian. The relative timing of microwaves and X-rays from solar flares. *Astrophys. J.*, 354:735–744, May 1990. doi: 10.1086/168730.

H. Maehara, T. Shibayama, S. Notsu, Y. Notsu, T. Nagao, S. Kusaba, S. Honda, D. Nogami, and K. Shibata. Superflares on solar-type stars. *Nature*, 485:478–481, May 2012. doi: 10.1038/nature11063.

T. Magara and D. W. Longcope. 3-DIMENSIONAL Evolution of a Magnetic Flux Tube Emerging Into the Solar Atmosphere. *AGU Fall Meeting Abstracts*, page A441, December 2002.

S. Masuda, T. Kosugi, H. Hara, S. Tsuneta, and Y. Ogawara. A loop-top hard X-ray source in a compact solar flare as evidence for magnetic reconnection. *Nature*, 371:495–497, October 1994. doi: 10.1038/371495a0.

S. Masuda, T. Kosugi, H. Hara, T. Sakao, K. Shibata, and S. Tsuneta. Hard X-Ray Sources and the Primary Energy-Release Site in Solar Flares. *PASJ*, 47:677–689, October 1995.

C. Meegan, G. Lichti, P. N. Bhat, E. Bissaldi, M. S. Briggs, V. Connaughton, R. Diehl, G. Fishman, J. Greiner, A. S. Hoover, A. J. van der Horst, A. von Kienlin, R. M. Kippen, C. Kouveliotou, S. McBreen, W. S. Paciesas, R. Preece, H. Steinle, M. S. Wallace, R. B. Wilson, and C. Wilson-Hodge. The Fermi Gamma-ray Burst Monitor. *Astrophys. J.*, 702: 791, September 2009. doi: 10.1088/0004-637X/702/1/791.

H. Mészárosová, M. Karlický, and F. Fárník. Quasi-periodic oscillations in solar X-ray sources. In A. Bonanno, E. de Gouveia Dal Pino, and A. G. Kosovichev, editors, *IAU Symposium*, volume 274 of *IAU Symposium*, pages 255–257, June 2011. doi: 10.1017/S1743921311007071.

J. A. Miller, P. J. Cargill, A. G. Emslie, G. D. Holman, B. R. Dennis, T. N. LaRosa, R. M. Winglee, S. G. Benka, and S. Tsuneta. Critical issues for understanding particle acceleration in impulsive solar flares. *J. Geophys. Res.*, 102:14631–14660, July 1997. doi: 10.1029/97JA00976.

H. Nakajima, H. Sekiguchi, S. Aiba, Y. Shiomi, T. Kuwabara, M. Sawa, H. Hirabayashi, T. Kosugi, and K. Kai. A New 17-GHZ Solar Radio Interferometer at Nobeyama. *PASJ*, 32:639, 1980.

H. Nakajima, H. Sekiguchi, M. Sawa, K. Kai, and S. Kawashima. The radiometer and polarimeters at 80, 35, and 17 GHz for solar observations at Nobeyama. *PASJ*, 37:163–170, 1985.

V. M. Nakariakov, C. Foullon, I. N. Myagkova, and A. R. Inglis. Quasi-Periodic Pulsations in the Gamma-Ray Emission of a Solar Flare. *Astrophys. J. Lett.*, 708:L47–L51, January 2010. doi: 10.1088/2041-8205/708/1/L47.

T. Neukirch. Magnetic Reconnection; Parallel Electric Fields and Particle Acceleration. In R. D. Bentley and J. T. Mariska, editors, *Magnetic Reconnection in the Solar Atmosphere*, volume 111 of *Astronomical Society of the Pacific Conference Series*, page 286, 1997.

N. V. Nitta, S. L. Freeland, and W. Liu. An Alternative View of the "Masuda" Flare. *Astrophys. J. Lett.*, 725:L28–L33, December 2010. doi: 10.1088/2041-8205/725/1/L28.

E. N. Parker. Sweet's Mechanism for Merging Magnetic Fields in Conducting Fluids. *J. Geophys. Res.*, 62:509–520, December 1957. doi: 10.1029/JZ062i004p00509.

W. D. Pesnell, B. J. Thompson, and P. C. Chamberlin. The Solar Dynamics Observatory (SDO). *Sol. Phys.*, 275:3–15, January 2012. doi: 10.1007/s11207-011-9841-3.

H. E. Petschek. Magnetic Field Annihilation. *NASA Special Publication*, 50:425, 1964.

E. Priest and T. Forbes, editors. *Magnetic reconnection : MHD theory and applications*. Cambridge University Press, 2000.

Alessandro Retinò. *Magnetic Reconnection in Space Plasmas*. PhD thesis, Uppsala Universitet, June 2007.

J. Schou, P. H. Scherrer, R. I. Bush, R. Wachter, S. Couvidat, M. C. Rabello-Soares, R. S. Bogart, J. T. Hoeksema, Y. Liu, T. L. Duvall, D. J. Akin, B. A. Allard, J. W. Miles, R. Rairden, R. A. Shine, T. D. Tarbell, A. M. Title, C. J. Wolfson, D. F. Elmore, A. A. Norton, and S. Tomczyk. Design and Ground Calibration of the Helioseismic and Magnetic Imager (HMI) Instrument on the Solar Dynamics Observatory (SDO). *Sol. Phys.*, 275:229–259, January 2012. doi: 10.1007/s11207-011-9842-2.

M. Selwa, K. Murawski, and S. K. Solanki. Excitation and damping of slow magnetosonic standing waves in a solar coronal loop. *Astron. Astrophys.*, 436:701–709, June 2005. doi: 10.1051/0004-6361:20042319.

K. Shibasaki, M. Ishiguro, S. Enome, and P. puppa. Solar Radio Acquisition and Communication System /SORDACS/ of Toyokawa Observatory. *Proceedings of the Research Institute of Atmospherics, Nagoya University*, 26:117–127, March 1979.

T. Shibayama, H. Maehara, S. Notsu, Y. Notsu, T. Nagao, S. Honda, T. T. Ishii, D. Nogami, and K. Shibata. Superflares on Solar-type Stars Observed with Kepler. I. Statistical Properties of Superflares. *Astrophys. J. Supp. Ser.*, 209:5, November 2013. doi: 10.1088/0067-0049/209/1/5.

B. V. Somov and T. Kosugi. Collisionless Reconnection and High-Energy Particle Acceleration in Solar Flares. *Astrophys. J.*, 485:859–868, August 1997.

M. Stix. *The Sun. an Introduction*. 1989.

P. A. Sweet. The Neutral Point Theory of Solar Flares. In B. Lehnert, editor, *Electromagnetic Phenomena in Cosmical Physics*, volume 6 of *IAU Symposium*, page 123, 1958.

T. Takakura and E. Scalise. Gyro-Synchrotron Emission in a Magnetic Dipole Field for the Application to the Center-to-Limb Variation of Microwave Impulsive Bursts. *Sol. Phys.*, 11:434–455, March 1970. doi: 10.1007/BF00153078.

C. Torii, Y. Tsukiji, S. Kobayashi, N. Yoshimi, H. Tanaka, and S. Enome. Full-automatic radiopolarimeters for solar patrol at microwave frequencies. *Proceedings of the Research Institute of Atmospherics, Nagoya University*, 26:129–132, March 1979.

S. Tsuneta and T. Naito. Fermi Acceleration at the Fast Shock in a Solar Flare and the Impulsive Loop-Top Hard X-Ray Source. *Astrophys. J. Lett.*, 495:L67–L70, March 1998. doi: 10.1086/311207.

S. Vaughan. A simple test for periodic signals in red noise. *Astron. Astrophys.*, 431:391–403, February 2005. doi: 10.1051/0004-6361:20041453.

L. M. Walkowicz, G. Basri, N. Batalha, R. L. Gilliland, J. Jenkins, W. J. Borucki, D. Koch, D. Caldwell, A. K. Dupree, D. W. Latham, S. Meibom, S. Howell, T. M. Brown, and S. Bryson. White-light Flares on Cool Stars in the Kepler Quarter 1 Data. *Astron. J.*, 141:50, February 2011. doi: 10.1088/0004-6256/141/2/50.

T. J. Wang, S. K. Solanki, W. Curdt, D. E. Innes, I. E. Dammasch, and B. Kliem. Hot coronal loop oscillations observed with SUMER: Examples and statistics. *Astron. Astrophys.*, 406:1105–1121, August 2003. doi: 10.1051/0004-6361:20030858.

R. S. White, E. Verwichte, and C. Foullon. First observation of a transverse vertical oscillation during the formation of a hot post-flare loop. *Astron. Astrophys.*, 545:A129, September 2012. doi: 10.1051/0004-6361/201219856.

H. J. Wiehl, W. A. Schochlin, and A. Magun. Microwave Time Delays as Evidence for a Collisionless Conduction Front. *Astron. Astrophys.*, 92:260, December 1980.

Y.-H. Yang, C. Z. Cheng, S. Krucker, M.-S. Hsieh, and N.-H. Chen. Asymmetry of Hard X-Ray Emissions at Conjugate Footpoints in Solar Flares. *Astrophys. J.*, 756:42, September 2012. doi: 10.1088/0004-637X/756/1/42.

Acknowledgment